ROYAUME DU MAROC
Université Mohammed V - RABAT -
جامعة محمد الخامس – الرباط –
Faculté des sciences
كلية العلوم
CENTRE D'ETUDES DOCTORALES - SCIENCES ET TECHNOLOGIES

N° d'ordre : 3268

THESE

En vue de l'obtention du : **DOCTORAT**

Structure de Recherche : Laboratoire de la Matière Condensée et Sciences Interdisciplinaires
Discipline : Sciences de la Matière Physique
Spécialité : Matière Condensée et Modélisation des Systèmes

Présenté et soutenu le 13/12/2019

Par :

Anass SIBARI

Phosphorene as a promising 2D material for Energy Conversion, Energy Storage and Sensing Applications: ab-initio study

JURY

Mohammed LOULIDI	PES, Faculté des Sciences, Université Mohammed V-Rabat	Président
Hamid EZ-ZAHRAOUY	PES, Faculté des Sciences, Université Mohammed V-Rabat	Rapporteur/Examinateur
El Mustapha FEDDI	PES, ENSET, Université Mohammed V-Rabat	Rapporteur/Examinateur
Abdelkader KARA	PES, University of Central Florida, Orlando-USA	Rapporteur/Examinateur
Abdelilah BENYOUSSEF	PES, Académie Hassan II des Sciences et Techniques-Rabat	Examinateur
Omar MOUNKACHI	PA, Faculté des Sciences, Université Mohammed V-Rabat	Invité
Ari Paavo SEITSONEN	Dr, École Normale Supérieure, Paris-France	Invité
Mohammed BENAISSA	PES, Faculté des Sciences, Université Mohammed V-Rabat	Directeur de Thèse

Année Universitaire : **2019/2020**

✉ Faculté des Sciences, avenue Ibn Battouta, BP. 1014 RP, Rabat –Maroc
☎ 00212(05) 37 77 18 76 🖷 00212(05) 37 77 42 61; http://www. fsr.um5.ac.ma

“ Fail early,

Fail often,

Fail forward.”

– John C. Maxwell

مهداة لأبي وأمي،

ولروح جدتي الطاهرة.

Acknowledgments

This thesis was carried out at the Laboratory of Condensed Matter and Interdisciplinary Sciences (LaMCScI) of the Faculty of Sciences, University Mohammed V-Rabat, Morocco under the supervision of Prof. **Mohammed BENAISSA**.

First and foremost, praises and thanks go to Allah, the Almighty, for his unlimited and uncountable blessings in my whole life and throughout my research work especially.

I would like to express my very great appreciation, deep gratitude and sincere thanks to my supervisor Prof. **Mohammed BENAISSA**, for giving me the opportunity to learn from his valuable expertise. He always had the time to answer my questions and he patiently provided the vision, encouragement and the necessary advice for me to proceed throughout my research period. It has been truly a great pleasure to work with you and an even greater privilege to be your student.

I would like also to thank the thesis committee for reviewing my work and giving their insightful and useful comments. It is an honor for me that they agreed to judge this work.

I would like to thank Prof. **Mohammed LOULIDI** from University Mohammed V-Rabat, Faculty of Science, who agreed to be the president of the jury members of this thesis.

I would like also to express my thanks to Prof. **Hamid EZ-ZAHRAOUY** from University Mohammed V-Rabat, Faculty of Science, for reporting and reviewing this PhD thesis.

I would like also to extend my thanks to Prof. **El Mustapha FEDDI** from University Mohammed V-Rabat, École Normale Supérieure de l'Enseignement Technique, for reporting and reviewing this PhD thesis.

I would like also to offer my thanks to Prof. **Abdelkader KARA** from the University of Central Florida, Orlando, United States, for reporting and reviewing this PhD thesis.

I would like also to offer my sincere thanks to Prof. **Abdelilah BENYOUSSEF** from Académie Hassan II des sciences et techniques of Rabat, for reviewing this thesis.

I would like also to extend my thanks to Prof. **Omar MOUNKACHI** from University Mohammed V-Rabat, Faculty of Science, for reviewing this PhD thesis. I would like also to take

this opportunity to thank Prof. **Omar MOUNKACHI** who introduced me, as my Master's supervisor, to the field of 2D materials by allowing me to work on a fascinating subject such as the study of Phosphorene and who helped me also to put my very first steps in my research career.

I would also like to express my thanks to Dr. **Ari Paavo SEITSONEN** from École Normale Supérieure, Paris, France, for reviewing this PhD thesis.

I would like to point out that part of this thesis was carried out at the University of Central Florida of USA in the frame of the ***Fulbright Joint-Supervision Program*.** I would like to express my deep gratitude to the Fulbright and MACECE committees who granted me to pursue a year of research and training in the USA under the supervision of Prof. **Abdelkader KARA** to whom I would like to extend my deepest appreciations for hosting me throughout my stay at UCF. Words cannot express my gratitude, nor my thanks for all your help and guidance. It has been a great honor to closely work with you. My thanks go also to all Professors, administrative employees and PhD students at the department of Physics of UCF. Also, I would like to extend my thanks to the Moroccan community in Orlando who were of essential assistance to me throughout my stay there.

I would like to take this opportunity to express my sincere gratitude to Prof. **Abdelilah BENYOUSSEF**, Prof. **Omar MOUNKACHI**, Prof. **Mohammed HAMEDOUN**, Prof. **William KADEN**, Dr. **Marwan LAKHAL**, Dr. **Adil MARJAOUI**, Dr. **Karima LASRI** and Dr. **Walter MALONE** for their fruitful discussions and assistance. My thanks go also to my colleagues Dr. **Mustapha ABDELLAOUI**, Dr. **Hanan ABSIKE, Mohammed Khalil HAJJI**, **Wafaa AZOUZI**, **Hind BENZIDI**, **Rachida LAMOURI, Hind EL MASAOUDI, Nusaiba ZAMAN** and **Muhammad SAJID**. In particular, I would like to express my special thanks to my colleague Dr. **Zineb KERRAMI** with whom I shared the good and bad moments of my PhD studies.

Finally, my gratitude goes to my parents for their encouragements and continuous prayers and for their emotional and financial support. My gratitude goes also to my brother, his wife and my beloved Adam, to my extended family, friends and everyone who helped and supported me in any way during my PhD studies.

Abstract

The present thesis discusses one of the most exciting areas of Nano-science over the last few years; the study of the newly discovered two-dimensional (2D) material: Phosphorene, a two-dimensional variant of the layered black Phosphorus. Due to its unique puckered structure, tunable bandgap and other intriguing properties, Phosphorene is very attractive for many applications. For that, a comprehensive first-principles study based on Density Functional Theory was employed to get a better understanding of its physical properties and its potential in different applications.

Our results show that its electronic properties are very flexible and a mechanical strain could be adopted to engineer its bandgap to make of it an effective material for optoelectronic devices. Moreover, Phosphorene's unique puckered structure in addition its large inter-sheets distance which is capable of hosting large ions such as sodium (2.04 Å) or potassium (2.76 Å) show that Phosphorene clearly exhibits a higher performance than graphene as an anode material for energy storage devices. Lastly, the adsorption of different toxic molecules on Phosphorene shows, for some molecules, a substantial charge transfer from the substrate to the molecule in addition to strong binding energies; indicating the promising potential of Phosphorene as a gas sensor device.

Keywords: 2D Materials, Phosphorene, Density Functional Theory, Energy Conversion, Energy Storage, Gas Sensing.

Résumé

Cette thèse aborde l'un des sujets les plus passionnants de la nanoscience au cours des dernières années ; l'étude du matériau bidimensionnel (2D) récemment découvert : le Phosphorène, une variante bidimensionnelle du phosphore noir. Sa structure unique, son gap ajustable et autres propriétés fascinantes attire l'attention de nombreuses applications. Pour cela, une étude approfondie basée sur la théorie de la densité fonctionnelle a été menée pour mieux comprendre ses propriétés physiques et son potentiel dans différentes applications.

Nos résultats montrent que ses propriétés électroniques sont très flexibles et qu'une contrainte mécanique pourrait être adoptée pour varier son gap et en faire un matériau efficace pour les dispositifs optoélectroniques. De plus, la structure plissée unique de Phosphorène ainsi que sa grande distance entre les feuilles, capable d'accueillir des grands ions tels que le sodium (2,04 Å) ou le potassium (2,76 Å), montrent que le Phosphorène présente clairement une performance supérieure au graphène en tant qu'anode pour les dispositifs de stockage d'énergie. Enfin, l'adsorption de différentes molécules toxiques sur le phosphorène montre un transfert de charge important du substrat vers la molécule en plus de fortes énergies de liaison ; indiquant le potentiel prometteur du Phosphorène dans la détection de gaz toxiques.

Mots-clés : Matériaux 2D, Phosphorène, Théorie de la densité fonctionnelle, Conversion d'énergie, Stockage d'énergie, Détection de gaz.

Résumé détaillé

En un peu plus d'une décennie, la famille de systèmes bidimensionnels est passée de la découverte singulière du graphène en 2004 à plus de 40 nouveaux membres, dont le Phosphorène. Ces nombreux matériaux se sont révélés d'avoir des propriétés électroniques, optoélectroniques et mécaniques intéressantes et uniques résultants principalement de leurs propriétés de surface exceptionnelles, qui sont absentes dans leurs précurseurs massiques. Ces propriétés intrigantes pourraient permettre aux matériaux 2D de constituer une solution viable pour la réduction continue de la taille et l'amélioration des performances des dispositifs électroniques, comme le prévoit la loi de Moore.

Lors de cette thèse, nous avons utilisé des calculs basés sur des principes-fondamentaux pour explorer et exploiter les propriétés physiques du Phosphorène dans diverses applications technologiques. La réponse du Phosphorène en termes de ses propriétés électroniques à l'effet combiné de la taille et de la déformation est également étudié, ainsi que celui des comportements d'adsorption et de diffusion de différents métaux sur une monocouche de Phosphorène afin d'examiner son potentiel en tant que matériau anodique pour les batteries rechargeables. En outre, nous avons élargi notre étude afin d'explorer les perspectives du Phosphorène en tant que matériau de détection des gaz en étudiant les caractéristiques d'absorption de plusieurs molécules toxiques sur le Phosphorène.

Le chapitre III présente les résultats d'une étude détaillée sur la combinaison des effets de contrainte et de taille sur les propriétés structurales et électroniques d'une monocouche, bicouche et tri-couche de Phosphorène soumises à une contrainte uni-axiale. Nos calculs montrent que la contrainte exercée soit sur la direction armchair ou la direction du zigzag, tend à modifier la nature du point Γ de la bande interdite d'un espace électronique direct à un indirect en fonction de la valeur de la contrainte. Cependant, nous trouvons que dans une contrainte allant de -14% à + 6%, les structures ML, BL et TL se comportent comme la plupart des semi-conducteurs sous contrainte, où la contrainte de compression réduit la bande interdite alors que la contrainte de traction pose un effet inverse. Enfin, un effet combiné contrainte-taille très intéressant est observé sur les bandes

VBM et CBM où le niveau de Fermi se déplace d'un côté à l'autre du gap énergétique. Alors que les structures ML, BL et TL sont de type p à 0% de contrainte, elles basculent vers des semi-conducteurs de type n sous contrainte allant de + 2% à + 14%. Nous pensons que cette capacité de transition de type p à type n peut avoir un impact technologique majeur dans les domaines où des mono- et hétérojonctions sont nécessaires.

Dans le chapitre IV, nous avons étudié les comportements d'adsorption et de diffusion d'atomes alcalins (Li, Na et K) et d'atomes de métaux alcalino-terreux (Be, Mg et Ca) sur une surface de Phosphorène afin d'évaluer ses performances en tant qu'un matériau anode pour les piles rechargeables. Nos résultats montrent que tous les éléments peuvent être adsorbés de manière stable sur le Phosphorène et ont tendance à préférer être adsorbés sur le site H. L'énergie de liaison des atomes alcalins montre que la taille de l'atome influe fortement sur l'interaction entre l'adatom et le substrat, tandis que l'interaction des métaux alcalino-terreux et du Phosphorène est difficile à prédire. En comparaison avec le graphène, nos résultats montrent que le Phosphorène améliore les énergies de liaison des atomes adsorbés. De plus, une transition de semi-conducteur à métal est observée lors de l'adsorption complète de plus de quatre atomes, ce qui est vital pour les utilisations des électrodes. En outre, l'analyse de diffusion montre que la migration des atomes sur le Phosphorène est fortement influencée par son anisotropie structurelle, ce qui confère un privilège à la diffusion dans le sens du zigzag par rapport au armchair. En raison de sa grande taille atomique, nous avons constaté que la barrière de diffusion de K le long de la direction du zigzag est extrêmement basse (0,02 eV), tandis qu'une taille atomique de l'ordre de l'atome de Be trouve qu'il est presque interdit de diffuser dans la direction du armchair (0,77 eV). Nos résultats montrent que le Phosphorène présente clairement des performances plus élevées que d'autres matériaux 2D tels que le graphène en termes d'adsorption et de diffusion, mais une capacité de stockage inférieure à celle du dernier. Néanmoins, nous pensons qu'un système hybride phosphorène-graphène peut constituer une anode ionique à haute capacité.

Enfin, au chapitre V, nous avons étudié le comportement d'adsorption des molécules de NH_3, NO, NO_2, CO et CO_2 sur une surface de phosphorène en utilisant des calculs de principes-fondamentaux. D'après nos résultats, il a été constaté que l'approximation SCAN+rVV10 donnait un meilleur accord avec les paramètres de mailles expérimentaux du phosphore noir massique, par

rapport à optB88-vdW et PBE. Nos résultats montrent que toutes les molécules considérées peuvent se lier fortement à la surface du Phosphorène avec différents sites d'adsorption préférables en énergie, lorsque les interactions de van der Waals sont prises en compte. À l'exception de NO et NO_2, aucun transfert de charge notable n'a été trouvé. Pour NO_2, optB88-vdW et SCAN+rVV10 prévoient un transfert de charge substantiel du substrat vers la molécule (~ 0,34e), tandis que pour NO, SCAN+rVV10 prédit un transfert de charge négligeable et optB88-vdW qui prédit un transfert de charge négligeable (. 16e). Les effets calculés de la couverture moléculaire ont montré des différences substantielles entre les deux fonctionnelles. Notre comparaison calculée entre les fonctions optB88-vdW et la nouvellement introduite SCAN+rVV10 montre que, à mesure que la couverture augmente, des différences substantielles dans les énergies d'adsorption et les configurations entre les deux fonctions commencent à apparaître.

En se basant sur les résultats présentés dans cette thèse, nous avons montré que la structure unique " plissée " du Phosphorène et sa bande interdite directe ajustable s'ajoutant à sa mobilité exceptionnelle des porteurs, son rapport surface/volume élevé et sa grande distance entre couches pourrait faire du Phosphorène un candidat potentiel pour les dispositifs nanoélectroniques de prochaine génération où de telles propriétés sont nécessaires, comme dans les dispositifs optoélectroniques, les batteries et les capteurs de gaz. Néanmoins, nous pensons qu'une intégration totale du Phosphorène dans les technologies futuristes se heurte à un obstacle majeur en raison de nombreux facteurs limitant la possibilité de profiter des propriétés aussi prometteuses du Phosphorène telles que son oxydation rapide et sa dégradation subséquente dans des conditions ambiantes. Cependant, et bien que l'achèvement de ce travail ne fût pas une tâche facile à réaliser en raison du manque de ressources de calcul de hautes performances dans notre pays, nous espérons que les résultats présentés dans cette thèse pourront fournir un éclairage instructif aux chercheurs travaillant sur la fabrication d'appareils à haute performance à base de Phosphorène dans l'avenir.

List of Contents

List of Figures

List of Tables

List of Abbreviations

0D Zero Dimensional

1D One Dimensional

2D Two Dimensional

3D Three Dimensional

Å Angstrom

APW Augmented Plane Wave

ATP Adenosine Triphosphate

bP Black Phosphorus

BL Bilayer

C Charge Transfer

CBM Conduction Band Minimum

CC Coupled Cluster

CI Configuration Interaction

CMOS Complementary Metal–Oxide–Semiconductor

CNTs Carbon Nanotubes

CPU Central Processing Unit

CVD Chemical Vapor Deposition

DOS Density of States

DFT Density Functional Theory

E_b Binding Energy

FETs Field-effect Transistors

GGA Generalized Gradient Approximation

H-K Hohenberg-Kohn

K-S Kohn-Sham

LAPW Linearized Augmented Plane Wave

LDA Local Density Approximation

LIBs Li-ion batteries

ML Monolayer

MP Moller-Plesset

MoS_2 Molybdenum Disulfide

$MoSe_2$ Molybdenum Diselenide

$MoTe_2$ Molybdenum Ditelluride

NEB Nudged Elastic Band

PAW Projector Augmented Wave

PBE Perdew−Burke−Ernzerhof

PNRs Phosphorene Nanoribbons

QE Quantum ESPRESSO

SCAN Strongly Constrained and Appropriately Normed

SIBs Na-ion batteries

STM Scanning Tunneling Microscopy

STS Scanning Tunneling Spectroscopy

TL Trilayer

TMDs Transition Metal Dichalcogenides

VASP Vienna Ab initio Simulation Package

VBM Valence Band Maximum

vdW van der Waals

VOCs Volatile Organic Compounds

WS_2 Tungsten Disulfide

WSe_2 Tungsten Diselenide

GENERAL INTRODUCTION

Nanotechnology can be defined as the understanding and control of materials at dimensions smaller than 100 nm, where unique phenomena enable novel applications. At the nanometric scale, the physical, chemical and biological properties of materials differ in a fundamental way from those of atoms and individual molecules or materials in the bulk state.

Actually, dimensionality is one the most decisive characteristics for a material. The same substance may have completely different properties during the formation of its structure in various dimensions 0, 1, 2, or 3. Although zero-dimensional (0D) structures such as quantum dots, one-dimensional (1D) structures like nanotubes or three dimensional (3D) structures have been widely studied; research on two-dimensional (2D) crystals received less interest until the experimental realization, in 2004, of an atomic two-dimensional crystal, that is bi-layer of graphene [1].

In fact, the Nobel Prize of Physics in 2010 was awarded to Andre Geim and Kostya Novoselov from Manchester University [2] for their innovative experiments on graphene by making its fabrication very simple due to their technique of mechanical exfoliation. This two-dimensional crystal is nothing more than a single layer of graphite which is an already well-known material by the scientific community since the 60s. Among Geim and Novoselov's essential contributions is to have shown that graphene has remarkable mechanical and electronic properties such as high carrier mobility (200 000 $cm^2\ V^{-1}\ s^{-1}$) [3] but whose absence of an electronic bandgap limits its potential applications. Other two-dimensional materials have attracted considerable attention such as MoS_2 which has a direct gap of 1.96 eV but whose carrier mobility is much lower than that of graphene [4]. Recently, phosphorene has shown remarkable electronic properties as well. For example, it is reported that phosphorene has the drain current modulation up to 10^5 and a carrier mobility up to (1000 $cm^2V^{-1}s^{-1}$) [5], which makes phosphorene a potential candidate for future nanoelectronics applications. Phosphorene also has a direct bandgap which can be modified from 1.51 eV for a monolayer to 0.59 eV for a stack. Moreover, the p-type phosphorene transistor

has already been integrated with the n-type MoS_2 transistor to make a 2D Complementary Metal–Oxide–Semiconductor (CMOS) inverter [6].

Phosphorene is a nanomaterial with a 2D sheet structure composed of phosphorus atoms arranged in a honeycomb structure, which can be isolated in the laboratory through mechanical exfoliation from bulk **black Phosphorus** (bP), and has received considerable attention [7-10]. Indeed, Phosphorene's tunable direct bandgap can easily solve the problem of the absence of a gap in Graphene which is very crucial in **energy conversion** applications such as in optoelectronic devices. Moreover, Phosphorene's unique anisotropic and puckered structure in addition to its outstanding carrier mobility are expected to play an important role in a fast diffusion of the ions used in **energy storage** applications such as in Li-ion batteries. Lastly, we believe that the high surface-to-volume ratio present in Phosphorene in addition to its large inter-sheets distance (absent in Graphene) can be of advantage in **sensing applications** at a higher-coverage detection of toxic molecules.

Therefore, to explore the bulk and surface physical properties of Phosphorene and exploit them in various technological applications where Graphene could not perform well, various parameters are needed to describe those properties such as lattice parameters, atomic positions, densities of state, band structures, binding energies, diffusion barriers and theoretical capacities amongst others. For such reasons, we adopted in this thesis a theoretical approach based on Density Functional Theory (DFT) as the accurate calculation method of choice. Indeed, DFT has been well established for predicting structural and electronic properties of 2D materials where the interlayer van der Waals forces are essential to maintain the equilibrium structure. It is however well-known that it is less accurate when it comes to predicting the energy levels of excited states that are important in order to determine transport, optical and chemical properties.

This thesis is organized as follows:

- An introduction to 2D materials and their bulk precursors is presented in Chapter I, along with their synthesis methods and applications, in order to build an essential block to further studies.

- Chapter II focuses on the needed background of the computational methods for the calculations that are performed in the following chapters.
- In Chapter III, we explore the structural and electronic properties of phosphorene by combining the effects of size and strain in order to examine the tunability of its bandgap and semiconducting type.
- Chapter IV provides a comprehensive study on the potential of phosphorene as an anode material for rechargeable batteries by investigating the adsorption and diffusion behaviors of alkali and alkaline earth-metal atoms on a phosphorene monolayer.
- In Chapter V, the adsorption characteristics of several toxic molecules on phosphorene at different coverages are inspected in order to examine the prospects of phosphorene as a gas sensing material.
- Finally, a general conclusion summarizing the findings of this thesis dissertation is presented.

CHAPTER I: 2D MATERIALS AND THEIR BULK PRECURSORS

The history and existence of two-dimensional (2D) materials is mainly connected to layered bulk materials which are compounds with an intriguing layered structure including clays, chalcogenides, hydroxides, silicate minerals as well as graphite, hexagonal boron nitride, black phosphorus, etc. These compounds have already attracted for a long time the interest of the scientific research community in multiple scientific disciplines and industrial applications, from engineering of industrial materials to condensed matter theory.

To properly talk about 2D phosphorene, one should inevitably discuss layered black Phosphorus in the first place, because it is the well-recognized precursor to the ultrathin Phosphorene sheets. Afterwards the monolayer crystals which are essential for the aim of this thesis will be described to provide a firm base ground for the results.

I.1 Layered Materials

Layered materials form a large and important group of the naturally occurring compounds. Clays and ceramics have found their use in civil engineering, materials engineering as well as in high-temperature superconductivity. The chalcogenides have become an essential part of the semiconductor industry and mechanical engineering applications. Materials like graphite and hexagonal boron nitride have reached wide utilization from metallurgy, through artistic media, up to the medicine.

The common and defining feature of these layered materials is their underlying crystal structure of coupled, ultra-thin layers. This form determines their mechanical properties as the self-lubrication in the case of graphite or hexagonal boron nitride [11], but as well their electronic features promoting the effects of quantum confinement. The list of layered materials includes graphite, transition metal dichalcogenides, layered clays and even MoO_3, GaTe, or Bi_2Se_3 with diverse electrical, mechanical and optical properties [12].

I.1.1 Black Phosphorus

Elemental phosphorus can exist in several allotropes [13]; the most common of which are white and red solids. Solid violet and black allotropes are also known. Gaseous phosphorus exists as di-phosphorus and atomic phosphorus. Red and white phosphorus are highly flammable unlike black phosphorus which is the most thermodynamically stable form of phosphorus at room temperature and pressure [14-16].

Black phosphorus, which was discovered in 1914 [17], forms in several crystalline structures including orthorhombic, rhombohedral, and cubic [18]. Orthorhombic black phosphorus with space group *Cmca* is of importance because of its layered structure. Similar to graphite, orthorhombic black phosphorus is formed by repeated vertical stacking of individual atomic layers. The bonding of each atomic layer is very anisotropic. Out of plane interactions between each layer is weak (exfoliation energy is about -151 meV/atom) [19] and is considered as a consequence of van der Waals interactions. As such, black phosphorus is also known as a van der Waals material which includes the previously introduced TMDs and graphite. In-plane bonding is much stronger and is governed by atomic orbital hybridization. One of the most striking properties of black

phosphorus is its high hole mobility. In addition, the energy band gap of bulk black phosphorus is 0.3 eV, which places it in the infrared region of the electromagnetic spectrum [18].

Bulk black phosphorus has been historically synthesized under high pressure routes [14-16]. Bridgman et al. [14] found that when white phosphorus was subject to a 1.2 GPa pressure, it goes into a structural phase change. The resulting structure was black phosphorus. Both white and red phosphorus can be induced to transform into black phosphorus at high pressures [15,20]. However, high pressure routes of synthesis have relatively small yields and high pressures synthesis make experimental design a safety issue. As more interest in black phosphorus occurred, more methods of synthesis have been developed. Bulk black phosphorus has been made by high speed ball milling [21], closed transport reactions [22,23] and most recently through high energy sonication [24].

Just like TMDs, the increased interest in black phosphorus is in part due to the discovery of graphene in 2004 [25]. The successful separation of graphite layers to form one layer of graphene using mechanical exfoliation [25,26] sparked the race for 2D and quasi-2D materials. The amount of attention that black phosphorus received paid off in 2014 when two teams successfully synthesized monolayer black phosphorus, named phosphorene [27,28].

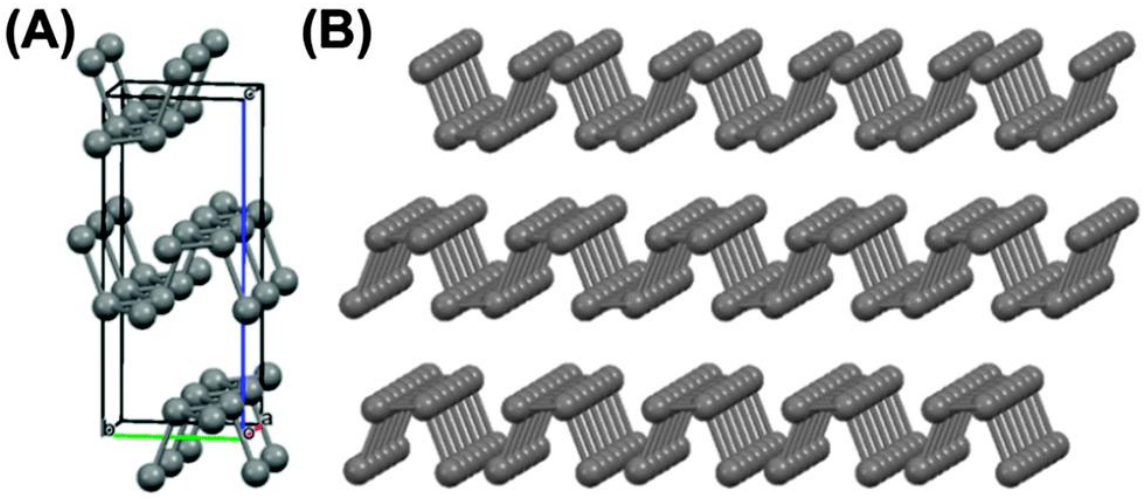

Figure I.1: The chemical structure of bulk black phosphorus (A) The orthorhombic unit cell of black phosphorus which generates a layer structure comprising corrugated lamellae of phosphorus atoms held together by weak interlayer forces. (B) Three-layer phosphorene.

- **Hybridization of Phosphorus**

Phosphorus atom (P) is in Group 15 of the periodic table. It has 16 neutrons, 15 electrons and 15 protons. Phosphorus compounds are abundant and found in many different systems. Groups of phosphates (PO_4^{3-}) are found in adenosine triphosphate (ATP) which is used as an energy source and as a neurotransmitter in our bodies [29].

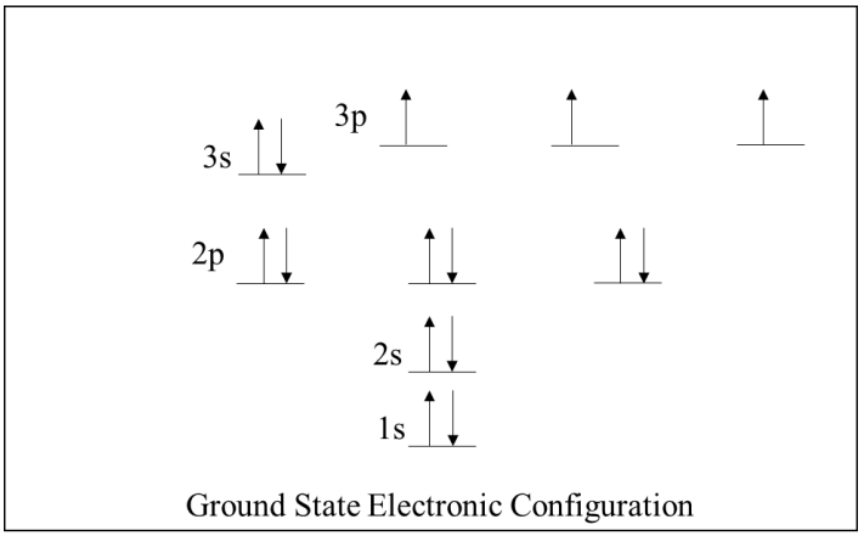

Figure I.2: The ground state electronic configuration for phosphorus.

The electronic configuration of phosphorus atoms in the ground state is $1s^2\,2s^2\,2p^6\,3s^2\,3p^3$. The orbitals involved in chemical reactions are the 3s and 3p orbitals shown in Figure 1.2. These orbitals are responsible for the nonexistence of elemental phosphorus naturally occurring. Unlike graphite, the in-plane bounding in black phosphorus is due to the sp^3 hybridization [30]. Each phosphorus atom is bonded to three adjacent phosphorus atoms. The above requires that each phosphorus atom retains a lone pair of electrons.

Due to each phosphorus atom having a lone pair of electrons, black phosphorus is a highly reactive material [31]. Those lone pairs contribute to bonding with other elements, in particular water and oxygen. In the presence of ambient environmental conditions, few layers of black phosphorus degrade to PO_x species [32] and phosphoric acid H_3PO_4 [33] within a few hours. Much work has been made to stop this degradation. Capping layers and advanced synthesis routes seem to be very promising [34,35].

I.2 Two-Dimensional Nanosheets

The separation of layered solids into individual layers was questioned for a long period of time. It was unclear whether it was even possible due to concerns about their stability at finite temperatures [36]. The long-lasting stand-off was broken in 2005, when the first successful isolation of single-layer atomic crystals was reported by K. S. Novoselov et al. [37].

The first separation of 2D materials has been performed by exfoliation of layered bulk materials. Thus graphene, boron nitride and molybdenum disulfide have been exfoliated from graphite, hexagonal boron nitride or molybdenum, respectively. Nowadays, also sandwich-like structures of these different 2D materials are realized, which allows to tune the properties of these layered structures [38]. The exfoliated sheets are not true two-dimensional objects, rather quasi 2D materials with a macroscopic size in two principal dimensions and a thickness of several atoms.

Further, we will discuss a couple of notable examples of ultrathin materials which are relevant for our results, including phosphorene, graphene, silicene and transition metal dichalcogenides. The focus lies on their common properties and structures.

I.2.1 Retrieval of the Nanosheets

Important aspects of 2D materials can be captured by understanding the conditions and methods used in the process of their synthesis or extraction. Two major method classes exist. The first one includes the top–down procedures, commonly called exfoliation techniques, where the molecular thin crystals are separated or grown from the bulk precursors. The second class of bottom–up practices, represents actual synthesis methods from other chemical compounds.

- **Exfoliation Techniques**

The exfoliation methods are the most direct way for obtaining 2D crystals. The group of bulk materials for which the exfoliation technique can be efficiently used includes black phosphorus, graphite, hexagonal boron nitride, transition metal dichalcogenides and transition metal oxides.

The first approach is the *liquid assisted exfoliation*. The bulk materials are exfoliated in a solvent with or without assistance of intercalation compounds or mechanical acceleration such as sonication. The obtained flakes of a few molecular layers are afterwards transferred to a substrate by spraying, mechanical transfer or by drying the suspension. The variety of method implementations is large, especially because of the number of layered materials and the specific processes (oxidation, intercalation or exchange, treatment by solvents, etc.).

Black phosphorus and most of the TMDs are suitable for the liquid-phase exfoliation. In fact, the preparation and isolation of phosphorene monolayers, bilayers and few-layers flakes using liquid-phase exfoliation in different solvents has been recently made by Adam H. Woomer et al. in 2015, identifying benzonitrile as the best solvent of the surveyed solvents [39]. The discovery of the liquid exfoliation was an important advancement and it is a research field under constant development as it allows production of large quantities of nanosheets.

Unlike the liquid exfoliation techniques *chemical exfoliation* realizes the final 2D material through intermediate steps with chemically modified compounds which can be exfoliated much more easily in the solvents in the form of a colloidal dispersion. For example, the well-known intermediate compound for the production of graphene is graphene oxide. It is produced from graphite that is oxidized with use of strong acids and oxidants, like in the Brodie, Staudenmaier and Hummers method [40]. After oxidation the individual graphene layers are heavily disrupted with a large portion of carbon atoms creating bonds with hydroxyl and epoxy groups. These sheets of layered material are strongly hydrophilic, which makes it easy to intercalate water between the layers and thus to create a colloidal suspension of graphene oxide in a water or other polar solvent with the help of sonication.

Still, the most direct approach of extracting single or multiple layers out of layered bulk crystals is *mechanical exfoliation*. The extraction employs mechanical cleaving. The best-known example is the mechanical exfoliation of graphene with a technique called the “scotch-tape method”. The process itself consists of repeatedly peeling of highly oriented pyrolytic graphite (a crystal of almost pure hexagonal graphite) which is performed by repeated sticking of an adhesive tape. In this way the weak interlayer forces can be overcome ending up with a single molecular layer from the layered crystal [37]. The direct advantages of the mechanical exfoliation are the simplicity of the method, which can be employed within a couple of hours, and the quality of the

obtained samples, which is of high grade, hard to be matched by other techniques. However, the main disadvantage is the lack of scalability, in terms of the sample size as well as the amount of time required for the production. Moreover, the nature of the technique gives little control over the number of exfoliated layers and the actual shape of the crystals [41].

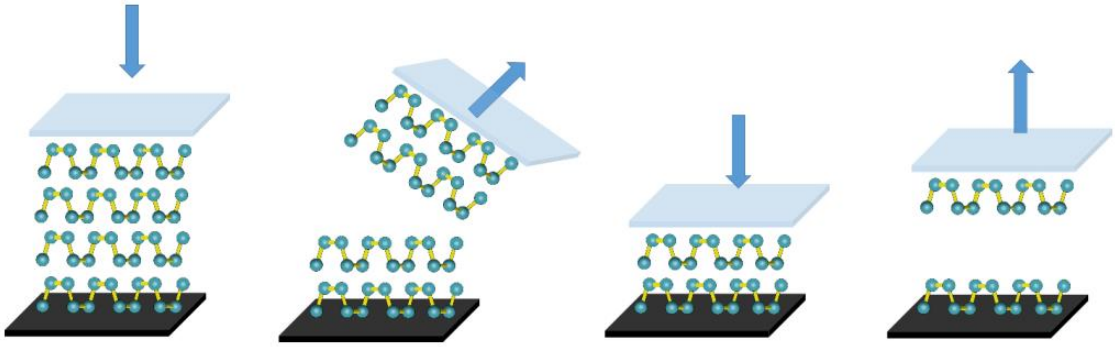

Figure I.3: Schematic of mechanical exfoliation process.

- **Synthesis Techniques**

Synthesis techniques unlike exfoliation ones do not require bulk layered material as precursors. The bottom up approaches are known to be very suitable for the large-scale production of two-dimensional crystals due to the scalability of the process and the reasonable to superior quality of the produced samples.

Probably the most promising method for scalable and continual production is *chemical vapor deposition (CVD)*. In the last decade large attention was given especially to the CVD synthesis of graphene due to its attractive electrical properties as a transparent conductive film, but TMDs, silicene and other monolayers can be produced in a similar fashion.

The synthesis process of graphene consists of exposing a metallic foil (Cu, Ni, Ru, etc.) in a high temperature reactor to the presence of organic compounds as a source of carbon atoms (CH_4, etc.) mixed in the gas atmosphere (H_2, Ar, etc.). After the crystal synthesis the graphene layer can be transferred directly with the use of epoxy resin and polymers or indirectly by a transport film or etching the metal substrate. The known inconveniences of this approach are the low control over the number of graphene layers as well as the polycrystallinity of the material which depends on the polycrystallinity of the substrate metal.

Under similar experimental conditions, the growth of silicene is possible as well. The first experimental evidence of successful epitaxial growth was reported by Padova et al. [42]. The growth of molybdenum disulfide is much more sensitive to the environmental conditions, including highly crystalline metal substrates or vacuum requirements. However, the successful CVD growth has been reported of the large area MoS_2 and WS_2 samples on amorphous SiO_2 substrates by sulfurization of deposited thin metal films.

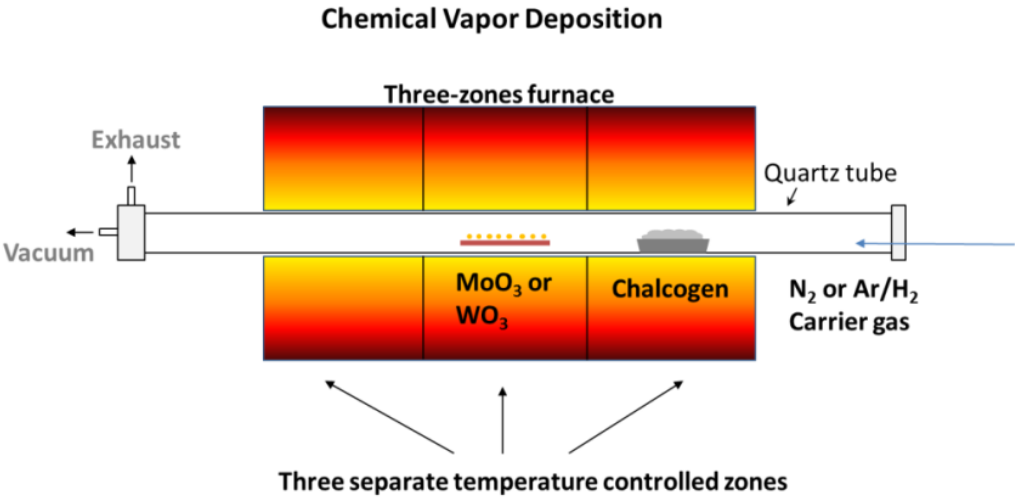

Figure I.4: Schematic of multi-zone quartz tube furnace used for CVD.

The second method is the *chemical synthesis* of carbon-based macromolecules from polycyclic aromatic hydrocarbons, which is a field with long history in chemistry. The route of a chemically driven, bottom–up approach, may not be appealing for the synthesis of large two-dimensional sheets of structurally simple materials like graphene, however there is a large set of more complex monolayer crystals without bulk counterparts including graphyne, its boron nitride analogue, graphdiyne, other planar benzene-based macromolecules, nanoribbons (1D structures), etc. which will benefit from the advances in available methods from organic chemistry.

I.2.2 Phosphorene

The discovery of graphene in 2004 brought forth a rapid development of exfoliation and other thin layer processing techniques, leading to a renewed interest in black phosphorus. In 2014,

theoretical and experimental works revealing the electronic properties of monolayer or few layers black phosphorus were published [43]. The results, showing a direct bandgap and high carrier mobility, stimulated the beginning of a new chapter in research on what came to be named phosphorene: that is, monolayer black phosphorus. Curiously, this name does not reflect the chemical nature of the material, which has no sp^2 bonds; instead, it comes from its conceptual similarity to graphene — the attributed name by the IUPAC is 2D phosphane [33].

- **Crystal Structure**

Single-layer phosphorene can be produced by liquid exfoliation from bulk black Phosphorus (bP). As shown in Figure I.1, bP has a layered structure with weak van der Waals (vdW) forces between the layers and strong in-plane covalent interactions. The atomic structure of single-layer phosphorene is shown in Figure I.5(a). In its structure, each P atom is covalently bonded to three neighbors, similar to graphene. However, a phosphorene layer is not flat; instead, it forms a puckered surface due to the sp^3 hybridization as shown in Figure I.5(b).

The optimized lattice parameters for a single-layer phosphorene are a = 4.62 Å and b = 3.30 Å. The calculated puckering height (i.e. thickness of single layer) is of 2.10 Å. The calculated P-P bond lengths are 2.22 Å for the horizontal bonds and 2.26 Å for the bonds in other directions. The sum of bond angles at each P atom in phosphorene is equal to 304.28°, close to the idealized value of 328° for sp^3 (tetrahedral) configuration and much smaller than 360° for sp^2 (planar).

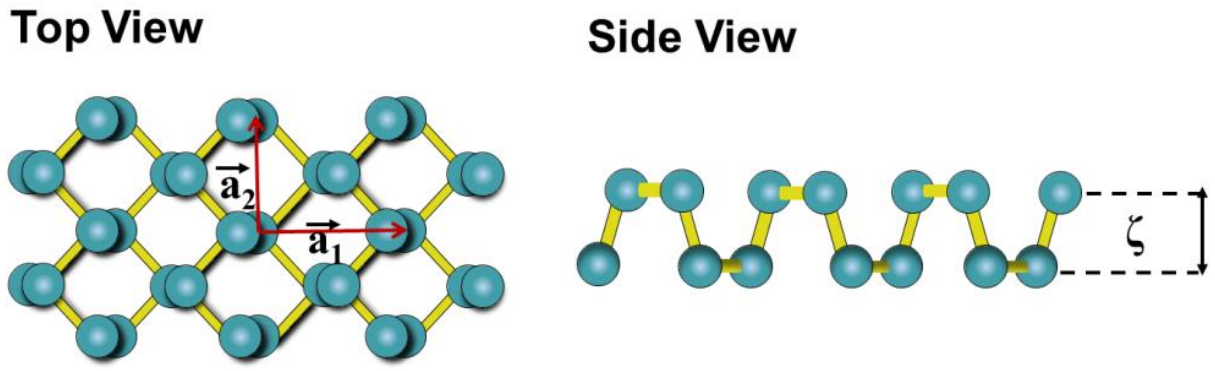

Figure I.5: Structure of phosphorene from a (a) top view and (b) side view with buckling parameter.

- **Anisotropy**

It is evident that phosphorene has taken the research community captive just as graphene has. With over 60 publications per month in 2015, the rate in phosphorene research is growing. One of the main contributors to this is its remarkable anisotropic properties [30,43,44].

Two-dimensional materials exhibit in-plane and out of plane anisotropy due to differences in bonding. In-plane bonding is dominated by covalent/ionic interactions and out of plane is vdW dependent. Vertical conductivity through one layer into another layer is dominated by quantum tunneling. As such it is much lower than in plane conductivity. Charge carrier motilities vary for in plane versus out of plane for graphene. However, for phosphorene there is an added anisotropy in the zigzag and armchair directions. Electric polarizability has a large difference in values for the zigzag direction and armchair direction [45]. By orientating the zigzag direction in the same sense as charge carrier flow in the conduction channel in a field effect transistor, device performance can be maximized [46]. Electronic transport is not the only property that is affected by anisotropy in phosphorene. Ion diffusion is of extreme importance in secondary battery anodes and cathodes. For anodes, it is extremely important to have high diffusion rates [47-49]. Due to the topological structure of phosphorene, anisotropic diffusion in the zigzag and armchair directions is difficult to determine and current theoretical models show conflicting results. The anisotropy in phosphorene can be utilized to make novel batteries and optoelectronic devices.

- **Electronic Structure**

Most studies on the electronic structure of phosphorene or thin bP are based on first principle calculations. Their electronic properties are determined mainly by the band dispersions in the vicinity of Γ point. For example, anisotropic properties arise from the difference between Γ-X and Γ-Y dispersions. Γ-X and Γ-Y directions correspond to armchair and zigzag directions, respectively. According to the first principle calculations, a direct band gap is located at Γ point in monolayer phosphorene, and it reduces with increasing the number of layers, to reach 0.3 eV at Z point in bulk bP. The presence of direct band gap in phosphorene is crucial and clearly distinguishes it from the other 2D materials, such as graphene and silicene.

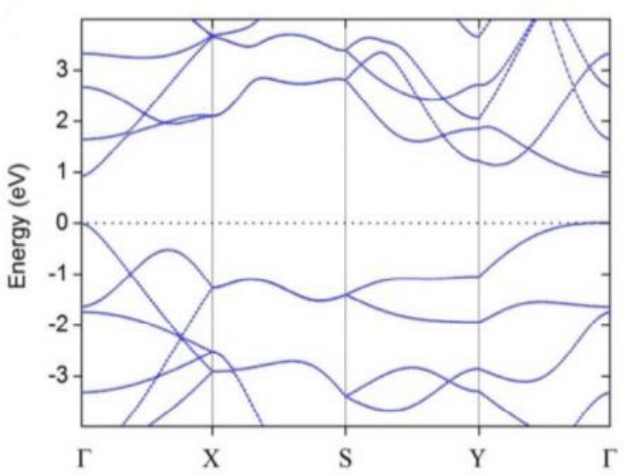

Figure I.6: Electronic band structure of single-layer phosphorene. The Fermi level is set to zero.

While the values of the band gap E_g have been calculated by many groups, they depend on the employed calculation method. The DFT method gives the value of around 1 eV, but this method is famous for underestimating the E_g. It is widely accepted that the reliable E_g is provided by the GW approach, which results in E_g = 2 eV. The Scanning Tunneling Microscopy/Spectroscopy (STM/STS) supports this prediction of $E_g \simeq 2$ eV [50].

- **Charge Transport**

The large carrier mobility observed in phosphorene is one of the factors that drew attention to this material over the past years and has been a driving force for the improvement of preparation and encapsulation methods. Typically, the mobility increases smoothly with an increasing number of layers up to a thickness of about 10 nm, reaching values exceeding 1000 $cm^2\ V^{-1}\ s^{-1}$ along the *y* direction (see Table I.1 for a comparison with other 2D materials) [51]. The comparison of this value with the theoretical limit for phonon-limited carrier mobility shows that there is still room for improvement: for holes, the mobility may reach values of up to 10 000–26 000 $cm^2\ V^{-1}\ s^{-1}$ along the *y* direction for the monolayer and up to 4800–6400 $cm^2\ V^{-1}\ s^{-1}$ for thick phosphorene (five layers) [46].

Table I.1: Properties of phosphorene compared with those of other 2D materials from Ref. [51].

2D Material	Crystal Class	Electronic Structure	Bandgap for monolayer (eV)	Mobility ($cm^2 V^{-1} s^{-1}$)
Graphene	Hexagonal	Semimetal	–	200 000 (freestanding; experimental value) [52]
TMDs (MoS_2)	Hexagonal	Semiconductor	1.96 (direct) [53]	< 320 for electrons and < 270 for holes (theoretical values) [54]
Phosphorene	Orthorhombic	Semiconductor	1.75 (direct) [50]	< 10 000–26 000 (monolayer; theoretical values) [46]

I.3 Applications and Limitations of Phosphorene

The easy fabrication and novel properties of phosphorene have led to the design and demonstration of extensive device applications in the areas of electronics, batteries, optoelectronics, photovoltaics and so on. Moreover, the extremely high pace of early developments suggests remarkable potential and many novel devices for phosphorene applications.

I.3.1 Optoelectronic Devices

Optoelectronics is a technology field which studies, designs, and manufactures devices converting electrical signals into photon signals and vice versa. Direct band gap, strong optical conductivity, efficient light absorption, and anisotropy of the optical properties make few-layer phosphorene a promising candidate for future applications in near and mid-infrared optoelectronics, such as detectors, switches, and modulators (night vision and thermal imaging), spectroscopy, as well as light generation devices (light-emitting diodes and lasers). The mechanical flexibility of phosphorene also makes its suitable for wearable optoelectronic devices.

One of the most exciting features of phosphorene for optoelectronics applications is the wide-range tunability of its band gap by applying strain [55] and by varying the number of layers [56], which allows to extend the covered frequency range from infrared to visible one. In their experiments, Engel et al. [56] found that a multi-layer black phosphorene photodetector is capable of acquiring high-resolution images both in the visible (λ = 532 nm) and in the infrared (λ = 1550 nm) spectral regime. This large degree of band gap tunability makes phosphorene a unique two-dimensional material that can be potentially used in optical communication networks for high-

speed data communication and nanoscale optical circuits. The phosphorene-based high-speed photo-detectors were shown to exhibit a vast improvement in efficiency over graphene-based devices.

Deng et al. [57] fabricated p–n diodes based on a van der Waals p–n heterojunction composed of p-type BP and n-type monolayer MoS_2. These p–n diodes show a maximum photodetection responsivity of 418 mA/W at the wavelength of $\lambda = 633$ nm and high photovoltaic energy conversion. The fabricated p-n diodes can be used for broad-band photodetection and solar energy harvesting.

Nevertheless, novel techniques to switch the semiconducting type of phosphorene from p-type to n-type could be very useful and may have a major technological impact in fields where mono- and hetero-junctions are needed. Indeed, in **Chapter III** we employed first-principle methods in order to engineer the electronic structure and semiconducting type of phosphorene from a p-type to n-type and vice-versa.

I.3.2 Batteries

Latest theoretical and investigational researches have revealed that phosphorus is a promising candidate for advanced battery applications, having a strong theoretical specific capacity of 2596 mAh/g and a discharge potential range of 0.4-1.2 V. The expected notably high average voltage of 2.9 V in a phosphorene-based Li-ion battery and excellent electrical conductivity of phosphorene as an electrode propose hopeful potential for its application as a rechargeable battery in many industrial fields. The discharge capacity of 2786 mAh/g attained at a 0.2C current rate is meaningfully higher than that in Li-ion batteries based on graphite, Ge and Sn as anode materials. Its reliability is demonstrated with a superb result of recycle life test, which appears that 80% of capacity is conserved after 100 cycles [58].

A recent study conducted by Zhao et al. have examined the potential application of phosphorene as an electrode material in Li-ion batteries by applying the density functional theory. As a result, Li atoms can bind with the phosphorene single- and bi-layer with a substantial electron transfer. Comparing to conventional anode materials currently used in batteries, monolayer of phosphorene has demonstrated higher specific capacity of 432.79 mAh/g. The outcome of this research reported on the improvement of Li atoms binding when phosphorene is doped with

silicon. Accordingly, lithiated phosphorene is considered as a suitable choice of electrode material in battery applications due to its remarkable properties such as a good capacity, low open-circuit voltage, minor volume changes and excellent electrical conductivity [59].

2D materials have aroused great amount of attentions to be employed as anode materials in battery applications because of their good surface-to-volume ratio and outstanding electronic properties. Recently, application of Li-ion batteries have been extensively developed because of their great reversible capacity and excellent cyclic lifespan. Their activity highly depends on Li capacity as well as cycling rate of anode materials.

But still, can we improve the electrochemical properties of batteries by choosing other metallic-ions rather than Li? In order to answer this question, we have investigated the effect of the adsorption and diffusion of different metallic-ions (Na, K, Mg, etc.) on the surface of phosphorene. These findings will be more elaborated in **Chapter IV**.

I.3.3 Gas Sensing

Gas sensing is another future application for phosphorene. The quasi-planar structure of phosphorene is highly anisotropic along the armchair and zigzag direction resulting in unique electrical and optical properties, highly useful for sensing purposes [60], this unique property is different from graphene and 2D-TMDs like MoS_2. The adsorption of CO, CO_2, NH_3 and NO_2 on single layers of graphene, MoS_2 and phosphorene are investigated to find their most stable configuration and relative orientations on the host layers and it has been found that the structural and electronic properties of host layers are unaffected as a result of the adsorption process. Among these host layers for gas sensing applications, phosphorene showed the highest physio-adsorption toward all examined molecules due to its controllable electronic properties in optoelectronics and switching devices. Therefore, phosphorene is considered as the most suitable Single Electron Transistor (SET) for gas sensing applications. MoS_2 and phosphorene are found to be more sensitive towards the detection of N-based molecules due to the introduction of stronger doping [61].

However, most of the studies which investigate the potential of 2D materials, including phosphorene, as a gas sensing material do not take into consideration the effect of the molecule-molecule interactions at higher adsorption coverages. In **Chapter V**, we will employ a recent

breakthrough in density functional theory, in the form of the meta-GGA SCAN approximation, in order to study the high coverage effect of the adsorption of different small molecules on the surface of phosphorene.

I.3.4 Other Applications for Phosphorene

- **Field-effect Transistors**

The variable bandgap energy, together with the high hole mobility at room temperature (up to 1000 $cm^2\ V^{-1}\ s^{-1}$ for a thickness of ~10 nm) make phosphorene suitable for electronic and optoelectronic applications. Most of the device designs proposed so far are based on FETs. FETs with phosphorene channels have consistently high on/off ratios (as high as 10^5) [27,28]. Subthreshold swings are still high, but a value as low as 69 meV dec^{-1} has been achieved for black phosphorus transistors with a high-*k* dielectric [62]. By carefully choosing the channel length, dielectric thickness and contacts, it is possible to obtain well-defined saturation of the drain current in the high drain–source bias region, a desirable characteristic for radio-frequency applications that is lacking in graphene-based transistors [63].

The first studies [64] showed that phosphorene-based transistors perform well in the radio-frequency range, exhibiting a peak short-circuit current gain cutoff frequency and a maximum oscillation frequency of 12 GHz and 30 Hz, respectively, for a channel length of 300 nm. The major challenges so far are the control of the device thickness, the suppression of degradation processes, and the control of the Schottky barrier height and of the conduction type.

Both the spectral response and the mobility depend critically on the number of phosphorene layers. At the same time, because, unlike in other 2D materials, the bandgap is direct (or nearly direct) regardless of the thickness, for most low frequency applications it is a good compromise to use a multilayer channel (with a thickness of ~10 nm), which provides a higher carrier mobility. This results in higher driving currents but in a lower on/off ratio [64]. Presently, the control of the channel thickness remains a problem because of the lack of scalable exfoliation methods able to produce samples with a narrow thickness distribution. In this regard, exfoliation in liquid and/or plasma thinning are the most promising solutions.

CHAPTER II: DENSITY FUNCTIONAL THEORY

The density functional theory (DFT) formalism is probably the most spread ab initio quantum mechanical modelling tool in the contemporary solid-state-matter research. In this Chapter, a short introduction and schematic overview of its principles is presented, as it is the method of choice for the results presented later in the manuscript.

DFT is built upon the premise that the properties of many electron systems, such as solid-state crystals, molecules and matter in general can be expressed as functionals of the electron density. The history of the formalism dates back to 1964 when the two Hohenberg and Kohn theorems were formulated. They express the equivalence between the electronic density and the all-electron wave function of a quantum mechanical many-body system. Shortly after, in 1965 the practical implementation by Kohn and Sham was introduced. However, only the later improvements of exchange-correlation energy, pseudopotentials and projector augmented wave method together with advances in the computational infrastructure allowed for its widespread use.

Next we discuss the DFT fundamentals and approximations.

II.1 Introduction

All materials are composed of atomic nuclei and electrons. The macroscopic material properties that we observe only depend on the position of these electrons and ions. Thus, knowing only the type of the atoms a material is made of is in principle enough to calculate the wave function and the energy of the system using the (time independent) Schrödinger equation:

$$H\Psi(\mathbf{r}_1, \mathbf{r}_2, ..., \mathbf{R}_1, \mathbf{R}_2, ...) = E\Psi(\mathbf{r}_1, \mathbf{r}_2, ..., \mathbf{R}_1, \mathbf{R}_2, ...) \qquad (2.1)$$

where ψ is the wave function of the system, r_i and R_i are the positions of the electrons and ions respectively, and H is the Hamiltonian of the system:

$$\begin{aligned} H = &-\sum_i \frac{\hbar^2 \nabla_i^2}{2m_e} - \sum_{i,I} \frac{1}{4\pi\epsilon_0} \frac{Z_I e^2}{|\mathbf{r}_i - \mathbf{R}_I|} + \frac{1}{2} \sum_{i \neq j} \frac{1}{4\pi\epsilon_0} \frac{e^2}{|\mathbf{r}_i - \mathbf{r}_j|} \\ &- \sum_I \frac{\hbar^2 \nabla_I^2}{2M_I} + \frac{1}{2} \sum_{I \neq J} \frac{1}{4\pi\epsilon_0} \frac{Z_I Z_J e^2}{|\mathbf{R}_I - \mathbf{R}_J|} \end{aligned} \qquad (2.2)$$

M_I and Z_I are the nuclear mass and charge respectively and m_e is the electron mass. This Hamiltonian can be decomposed in five terms:

$$H = T_e + V_{ext} + V_{int} + T_N + V_N \qquad (2.3)$$

where T_e and T_N are the kinetic energy operators of electrons and nuclei respectively, V_{ext} is the potential energy of the electrons in field of nuclei, V_{int} represents the Coulomb interaction between the electrons and similarly V_N is the Coulomb interaction between nuclei.

These calculations are known as first-principles or ab initio calculations since they are based only on the laws of physics and the values of nature's constants, such as Planck's constant ħ and the electron charge e. Nothing else is assumed or used as empirical input.

In practice, however, it is only possible to solve the Schrödinger equation exactly for small simple systems such as the hydrogen atom with spherical symmetry. For larger systems like molecules and solids, additional approximations have to be made.

II.1.1 Born-Oppenheimer approximation

The first step is the Born-Oppenheimer approximation which separates the motion of the ions and the electrons. This is justified by the fact that the mass of a nucleus is much larger than the mass of an electron so that they move on different time scales. From the electron point of view,

the ions are stationary and the electron cloud will rearrange itself instantaneously to any new ionic configuration. Mathematically, the wave function is rewritten as a product of the electron wave function and the nuclear wave function:

$$\Psi(\mathbf{r}_1, \mathbf{r}_2, ..., \mathbf{R}_1, \mathbf{R}_2, ...) = \psi(\mathbf{r}_1, \mathbf{r}_2, ...; \mathbf{R}_1, \mathbf{R}_2, ...) \cdot \chi_{nuc}(\mathbf{R}_1, \mathbf{R}_2, ...) \quad (2.4)$$

The semicolon in the electron wave function indicates that it is dependent upon the ionic positions as parameters but not as variables. The Schrödinger equation of the electrons for a given frozen ionic configuration is written as follows:

$$H'\psi(\mathbf{r}_1, \mathbf{r}_2, ...; \mathbf{R}_1, \mathbf{R}_2, ...) = E'\psi(\mathbf{r}_1, \mathbf{r}_2, ...; \mathbf{R}_1, \mathbf{R}_2, ...) \quad (2.5)$$

H' represents the electronic Hamiltonian consisting of only electronic terms:

$$H = T_e + V_{ext} + V_{int} \quad (2.6)$$

and the total Hamiltonian is then reduced to:

$$H = T_e + V_{ext} + V_{int} + V_N \quad (2.7)$$

With the Born-Oppenheimer approximation, the original problem is now reformulated as a quantum many-body problem for the electrons in a Hamiltonian set by the nuclei positions. The last, and probably hardest, obstacle to overcome is the reduction of the many-electron equation above to a solvable problem.

II.1.2 The Hartree approximation

The simplest way to solve the many-electron equation is to rewrite Eq. (2.5) as a one-particle equation for an electron moving in an average potential from all the electrons, as proposed by Hartree. The wave function then becomes:

$$\psi(\mathbf{r}_1, \mathbf{r}_2, ..., \mathbf{r}_n) = \phi_1(\mathbf{r}_1)\phi_2(\mathbf{r}_2) \cdots \phi_n(\mathbf{r}_n) \quad (2.8)$$

The ϕ_i (r_i) are *n* independent electron wave functions. A fundamental result in quantum mechanics states that if E_0 is the ground state energy solution of the Schrödinger equation, for any wave function φ:

$$\frac{\langle\varphi|H|\varphi\rangle}{\langle\varphi|\varphi\rangle} \geq E_0 \quad (2.9)$$

This is called the variational principle. This principle can be used with the Hamiltonian in Eq. (2.3) and the constraint that the wave function should have the Hartree form (presented in Eq. (2.8)) to prove that the solution to the Schrödinger equation in the Hartree approximation is obtained by solving the Hartree equation:

$$\left[-\sum_i \frac{\nabla_i^2}{2} - \sum_I \frac{Z_I}{|\mathbf{r}_i - \mathbf{R}_I|} + \sum_{j \neq i} \int \phi_j^*(\mathbf{r}_j) \frac{1}{|\mathbf{r}_i - \mathbf{r}_j|} \phi_j(\mathbf{r}_j)\right] \phi_i(\mathbf{r}_i) = \epsilon_i \phi_i^*(\mathbf{r}_i) \tag{2.10}$$

In the Hartree approximation, each electron i is treated independently but in an effective potential determined by an integration over the wave functions of the other electrons. Thus, the Hartree approximation is a mean-field approximation replacing the complicated many-body problem by n simpler problems in a mean-field potential. Hartree also proposed a self-consistent way to solve this equation since for the with wave function, the effective potential depends on all the other wave functions. Self-consistency is a procedure in which the wave function for the step *k* are found through solving the Eq. (2.10) with the effective potential determined by the wave function in step *k* - 1. The procedure is repeated until all the wave functions converge to a solution.

II.1.3 The Hartree-Fock approximation

Electrons being fermions, the exact many-particle wavefunction needs to be antisymmetric upon the exchange of electrons:

$$\psi(\mathbf{r}_1, \mathbf{r}_2, ..., \mathbf{r}_j, ..., \mathbf{r}_k, ..., \mathbf{r}_n) = -\psi(\mathbf{r}_1, \mathbf{r}_2, ..., \mathbf{r}_k, ..., \mathbf{r}_j, ..., \mathbf{r}_n) \tag{2.11}$$

This constraint can be added to the independent electron Hartree approach by using a Slater determinant as wave function instead of Eq. (2.8):

$$\Psi(\mathbf{r}_1, \mathbf{r}_2, ..., \mathbf{r}_n) = \frac{1}{\sqrt{n!}} \begin{vmatrix} \phi_1(\mathbf{r}_1) & \phi_2(\mathbf{r}_1) & \cdots & \phi_n(\mathbf{r}_1) \\ \phi_1(\mathbf{r}_2) & \phi_2(\mathbf{r}_2) & \cdots & \phi_n(\mathbf{r}_2) \\ \vdots & \vdots & & \vdots \\ \phi_1(\mathbf{r}_n) & \phi_2(\mathbf{r}_n) & \cdots & \phi_n(\mathbf{r}_n) \end{vmatrix} \tag{2.12}$$

Using the variational principle with this Slater determinant, it can be proven that the best solution is obtained by solving the Hartree-Fock equation:

$$\Big[-\sum_i \frac{\nabla_i^2}{2} - \sum_I \frac{Z_I}{|\mathbf{r}_i - \mathbf{R}_I|} + \sum_j \int \phi_j^*(\mathbf{r}_j)\frac{1}{|\mathbf{r}_i - \mathbf{r}_j|}\phi_j(\mathbf{r}_j)\Big]\phi_i(\mathbf{r}_i) - \sum_j \Big[\int \phi_j^*(\mathbf{r}_j)\frac{1}{|\mathbf{r}_i - \mathbf{r}_j|}\phi_i(\mathbf{r}_j)\Big]\phi_j(\mathbf{r}_i) = \epsilon_i \phi_i^*(\mathbf{r}_i) \quad (2.13)$$

The effect of the new constraint is to add a term, called the exchange potential, to the Hartree Eq. (2.10).

II.1.4 The correlation energy

The Hartree-Fock approach assumes independent electrons in an effective potential is an approximation to the true many-body problem. The energy missing is defined as the correlation energy ($E_{corr} = E_{exact} - E_{HF}$). Many methods exist to introduce this correlation energy very accurately for instance Moller-Plesset (MP) perturbation theory, configuration interaction (CI), or coupled cluster (CC) methods or quantum Monte-Carlo methods. However, these methods are computationally very expensive and only the smallest systems can be currently computed. On the other hand, Density Functional Theory (DFT) offers a good compromise between the qualitative description of electronic structure and the computational effort required to produce the result. Thus, DFT is one of the most popular and successful quantum mechanical approaches to describe matter. It is nowadays routinely applied for calculating, e.g., the binding energy of molecules in chemistry and the electronic band structure of solids in physics.

II.2 The fundamentals of Density Functional Theory

II.2.1 The Hohenberg-Kohn theorems

Modern theory of DFT is based on the two Hohenberg-Kohn (HK) theorems [65,66]: the first theorem states that the many-body wave function, which has a central position in standard quantum theory, can be replaced by the electron ground state density without any loss of information and the second theorem is more or less the equivalent of the variational principle in standard quantum mechanics. In DFT the electron density is the central quantity. In a system of n electrons, the electron density is defined from the wave functions as follows:

$$n(\mathbf{r}) = \sum_{i=1}^{N} \int \cdots \int d\mathbf{r}_1 ... d\mathbf{r}_N \Psi^*(\mathbf{r}_1, ..., \mathbf{r}_N)\delta(\mathbf{r}_i - \mathbf{r})\Psi(\mathbf{r}_1, ..., \mathbf{r}_N) \quad (2.14)$$

The energy is now rewritten from being the expectation value of the electronic Hamiltonian to a functional only depending on the electron density and not explicitly the wave function. The first Hohenberg-Kohn theorem is:

Theorem 1. For any system of interacting particles in an external potential $V_{ext}(r)$ the potential $V_{ext}(r)$ is determined uniquely, except for a constant, by the ground state density $n_0(r)$.

This implies that all the properties can thus be extracted from the exact ground state electron density. The problem is now only how to find this density. The second theorem based on the variational principle is helpful in this matter.

Theorem 2. A universal functional for the energy $E[n]$ in terms of the density $n(r)$ can be defined, valid for any external potential $V_{ext}(r)$. The exact ground state energy of the system is the global minimum of this functional and the density that minimizes the functional is the exact ground state density $n_0(r)$.

This reduces the very complex problem of finding all ground state physical properties of a system to finding the minimum of the energy with respect to the electron density. The energy functional is as follows:

$$E_{HK}[n] = T[n] + E_{int}[n] + \int V_{ext}(\mathbf{r})n(\mathbf{r})d\mathbf{r} \qquad (2.15)$$

where $E_{HK}[n]$ is the total energy functional, $T[n]$ its kinetic energy part and $E_{int}[n]$ the part coming from the electronic interactions. E_N does not depend on the density and is due to the nuclei-nuclei interaction. It should be noted that although the first Hohenberg-Kohn theorem requires a nondegenerate ground state, degenerate ground states are also allowed by the Levy formulation. It should also be noted that using the Hohenberg- Kohn formulation of DFT implies that we are working at $T = 0$ K.

II.2.2 The Kohn-Sham equations

The Hohenberg-Kohn theorems show that the electron density can rigorously be made the fundamental quantity of the many-body problem, but they are pure theorems of existence and say nothing on how this exact charge density can be found.

Kohn and Sham have shown that there is a way to map the problem of solving Eq. (2.15) to the one of solving a system of non-interacting electrons moving in an effective potential from all the (other) electrons. According to Theorem 2, the true electron density will minimize the total energy, but all means of finding it are valid. It could be guessed or, as suggested by Kohn and Sham, calculated from a reference system of non-interacting electrons moving in an effective potential. Thus, developing this variation with the full energy functional added (Eq. (2.15)), under the condition that the sum of the density throughout the molecule or solid should be constant and equal to the number of electrons,

$$\int_V n(\mathbf{r})d\mathbf{r} = n_e \qquad (2.16)$$

finally gives the Schrödinger-like equations called the Kohn-Sham equations:

$$\mathcal{H}\phi_i = [-\frac{1}{2}\nabla^2 + V_{eff}(\mathbf{r})]\phi_i = \epsilon_i\phi_i \qquad (2.17)$$

$\mathcal{H}$ is the one electron Hamiltonian and $V_{eff}(r)$ the effective potential in which the electron moves. The effective potential is given by

$$V_{eff}(\mathbf{r}) = V_{ext} + V_H + V_{XC} = V_{ext}(\mathbf{r}) + \int \frac{n(\mathbf{r}')}{|\mathbf{r}-\mathbf{r}'|}d\mathbf{r}' + \frac{\delta E_{XC}[n(\mathbf{r})]}{\delta[n(\mathbf{r})]} \qquad (2.18)$$

Since the electron density,

$$n(\mathbf{r}) = \sum_{i=1}^{occ.} |\phi_i(\mathbf{r})|^2, \qquad (2.19)$$

is needed to calculate the last two terms, which are the Coulomb potential from all electrons and the exchange-correlation potential, the Kohn-Sham equations need to be solved self-consistently. The new term, the exchange-correlation potential, appearing here contains all the many-body effects that are not present in the classical Hartree interaction term. The initial electron density can be chosen, for example, as a superposition of atomic densities. The Kohn-Sham equations can now be solved instead of finding the minimum of Eq. (2.15), and the orbitals $\phi_i\,(r)$ then give the electron density according to Eq. (2.19) above. These orbitals are often called Kohn-Sham orbitals and in the case of a non-spin-polarized system, each of these orbitals contain two electrons.

II.2.3 The exchange-correlation approximations

- **Local Density Approximation (LDA)**

The simplest physical way to approximate the exchange-correlation energy is the Local Density Approximation (LDA). In this approximation two assumptions are made: i) the local

exchange-correlation energy per particle only depends on the local density (hence the name of the approximation) and ii) is equal to the exchange-correlation energy per particle of a homogeneous electron gas, that has the same density, in a neutralizing positive background (jellium background). The total exchange-correlation energy E_{XC} is then given by the sum of the contributions of each point in space, where it is assumed that the contribution of one point only depends on the density of that particular point, independent of the other points. So:

$$E_{XC}[n] = \int n(\mathbf{r})\epsilon_{XC}(n(\mathbf{r}))d\mathbf{r} \qquad (2.20)$$

where $E_{XC}[n(r)]$ is the exchange-correlation energy per particle of a uniform electron gas of density $n(r)$. The quantity $E_{XC}[n(r)]$ can be further split into exchange and correlation contributions,

$$\epsilon_{XC}(n(\mathbf{r})) = \epsilon_X(n(\mathbf{r})) + \epsilon_C(n(\mathbf{r})) \qquad (2.21)$$

The exchange part, E_x, represents the exchange energy of an electron in a uniform electron gas and is given by:

$$\epsilon_X = -\frac{3}{4}\sqrt[3]{\frac{3n(\mathbf{r})}{\pi}} \qquad (2.22)$$

The correlation part, E_C, is determined using quantum Monte-Carlo simulations of the homogeneous electron gas as proposed by Ceperly and Alder [67].

This approximation is more accurate for systems with slowly varying densities, as it is assumed that the density is locally a constant. While being a simple approximation, the results of this approximation are surprisingly good. In general, LDA almost always leads to a correct picture of binding trends across the periodic table. Also, structures, bond lengths, vibrational energies, phonon spectra and other properties are predicted correctly, or with a systematic deviation. Binding energies of solids and molecules are usually overestimated, which leads to an underestimation of the bond lengths. Band gaps are also underestimated (a notorious example of this is the bandgap of bulk Ge, which is predicted to be metallic).

- **Generalized Gradient Approximation (GGA)**

In LDA, one uses the knowledge of the density in a point *r*. In real systems the density varies in space. A logical improvement of the LDA approximation would be to include also

information of this rate of change in the functional. This can be done by adding gradient terms. This approach is called the gradient-expansion approximation. In this class of approximation, one tries to systematically calculate gradient-corrections of the form $|\nabla n\,(r)|$, $|\nabla n\,(r)|^2$, $|\nabla^2 n\,(r)|$, etc., to the LDA. In practice, the inclusion of low-order gradient corrections almost never improves on the LDA, and often even worsens it. Moreover, higher-order corrections are exceedingly difficult to calculate and little is known about them. It was realized that instead of power-series-like systematic gradient expansions one could experiment with more general functions of $n(r)$ and $|\nabla n\,(r)|$ which needs not proceed order by order. Such functionals, of the general form:

$$E_{XC}^{GGA}[\rho(r)] = \int \rho(r)\varepsilon_{XC}\big(\rho(r)\big)\,\nabla\,\rho(r)dr \qquad (2.23)$$

are known as generalized-gradient approximations (GGAs). The current GGAs seem to give reliable results for all main types of chemical bonds and are popular in computational chemistry.

Overall, GGA type functionals, like PBE, are hoped to be more accurate than LDA type functionals, meaning a GGA functional should give better results for a larger array of systems than an LDA functional. LDA functionals may perform better than GGA functionals for a particular system or a particular group of systems, but overall GGA functionals should give better result than LDA functional.

- **Meta-GGA: SCAN**

Going further, the meta-GGA functionals [68-71] cost even more computational time than LDA or GGA functionals. This increase in computational cost is hoped to be rewarded with an increase in accuracy. The reason why meta-GGA functionals cost more than GGA functionals is because they are more mathematically complex than GGA functionals. Meta-GGA functionals, in contrast to all the functionals discussed previously, allow the exchange correlation interaction to depend on the electron density, the gradient of the electron density, and the Laplacian of the electron density:

$$E_{XC} = \int n\varepsilon_{XC}[n, \nabla\mathrm{n}, \nabla^2 n]\; d^3r \qquad (2.24)$$

As with GGA functionals, there are many different parameterizations of ε_{XC}. In this thesis, we will focus on the SCAN (Strongly Constrained and Appropriately Normed) functional [72]. As with PBE, ε_{XC} in SCAN can be divided further into an exchange and correlation energy per

electron. SCAN's exchange energy per electron is increasingly complicated and possesses a large number of parameters. Its general form however is:

$$E_X = \int n\varepsilon_{XC}^{LDA}(n)\, F_X(s,\alpha)\, d^3r \qquad (2.25)$$

From our discussion of the PBE functional we are familiar with all the terms in the above equation except α, which is a dimensionless Laplacian of the electron density.

$$\alpha = \frac{\tau - \tau_w}{\tau_{unif}} > 0 \qquad (2.26)$$

where τ is the Laplacian of the electron density, τ_w is the single-orbit limit of τ, and τ_{unif} is τ in the uniform-density limit. With these definitions $\tau = \tau_w$ or $\alpha = 0$ corresponds to the single-orbit limit or the limit of a single covenant bond, and $(\tau - \tau_w) = \tau_{unif}$ or $\alpha = 1$ corresponds to the uniform density limit or the metallic limit. SCAN's exchange energy per unit electron was constructed as an interpolation between $\alpha = 0$ and $\alpha = 1$, and an extrapolation to $\alpha = \infty$. Explicitly, τ_w and τ_{unif} are:

$$\tau_w = \frac{|\nabla|^2}{8n} \quad ; \quad \tau_{unif} = \frac{3}{10}(3\pi^2)^{\frac{2}{3}}(n)^{\frac{5}{3}} \qquad (2.27)$$

The expression for the correlation energy of SCAN possesses an even more complicated form than SCAN's exchange energy so we will omit it here. We will mention though, like the exchange energy, the correlation energy is a functional of the dimensionless Laplacian of electron density, τ, and that it was constructed as an interpolation between single-orbit limit, $\alpha = 0$, and the uniform density limit, $\alpha = 1$, and as an extrapolation to $\alpha = \infty$. The interested readers will find the correlation energy along with the rest of the derivation of SCAN in Sun's original paper [72].

II.3 Methods for electronic structure calculations

In this section we will briefly discuss the three most popular methods that are used to calculate the electronic band structure of 2D materials. These are (i) pseudopotentials in combination with the plane wave basis set (ii) the Linearized Augmented Plane Wave (LAPW) method and (iii) the projector augmented wave (PAW) method.

II.3.1 Plane wave pseudopotential method

Plane waves offer a natural choice as a basis set to expand the periodic functions $u_{nk}(r)$ as:

$$u_{n\mathbf{k}}(\mathbf{r}) = \sum_{\mathbf{G}} c_{n\mathbf{k},\mathbf{G}} e^{i\mathbf{G}\cdot\mathbf{r}} \qquad (2.28)$$

where the summation is over all the reciprocal lattice vectors G of the system under study. Thus, the electronic wave functions can be written as:

$$\phi_{n\mathbf{k}}(\mathbf{r}) = \sum_{\mathbf{G}} c_{n\mathbf{k},\mathbf{G}} e^{i(\mathbf{k}+\mathbf{G})\cdot\mathbf{r}}. \qquad (2.29)$$

The electronic wave functions at each k-point are now expressed in terms of a discrete plane wave basis set. In principle this Fourier series is infinite. However, in practice we cannot work with an infinite basis set, it has to be truncated. The number of plane waves can be restricted by placing an upper boundary to the kinetic energy of the plane waves. This boundary is called energy cut-off E_{cut} and only plane-waves satisfying the condition:

$$\frac{|\mathbf{k}+\mathbf{G}|^2}{2} < E_{cut} \qquad (2.30)$$

are considered in the computation.

With DFT, the complexity of the problem has reduced appreciably. However, for systems with a large number of electrons, it still remains computationally very expensive. Pseudopotentials helped in a crucial way to make the calculations tractable. Using the fact that the physical properties of solids depend mainly on valence electrons, the computational effort can be minimized considerably. In the pseudopotential approximation, the core electrons are removed and the strong ionic potential is replaced by the weaker pseudo potential V_{pseudo} that acts on a set of pseudo wave functions Ψ_{pseudo} rather than the true valence wave functions (Ψ). The pseudopotential and pseudo wave functions are generated in such a way that they are identical to the true potential and wave function beyond a certain radius known as cut-off radius r_c. In the core region the pseudo wave function is constructed such that all the nodes are removed but the norm is conserved. Also, since the nodes of the core states are removed, the number of plane-wave basis functions required to describe this wave function in the core region is much less resulting in reduced computational effort. This leads to a popular plane wave pseudopotential method for electronic structure

calculations. In this Thesis, we use this method to calculate the DFT band structure within the GGA approximation. These calculations are performed using the VASP code

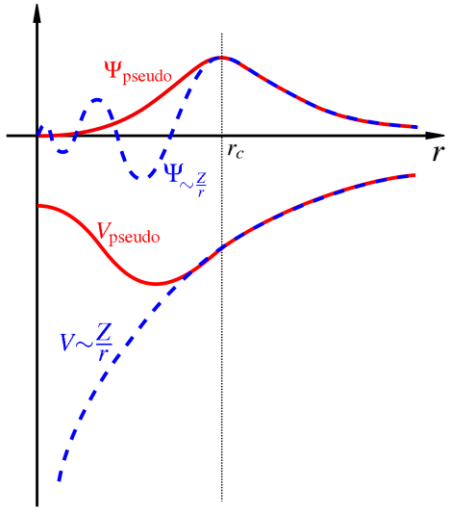

Figure II.1: Schematic representation of pseudopotential and the pseudo wave function.

II.3.2 All-electron methods

It is possible to solve the Kohn-Sham equations avoiding an artificial core-valence separation of electrons, as described by the pseudopotential. Such methods are called all-electron methods in which all the electrons are explicitly used in the computation.

- **Augmented plane wave (APW) method**

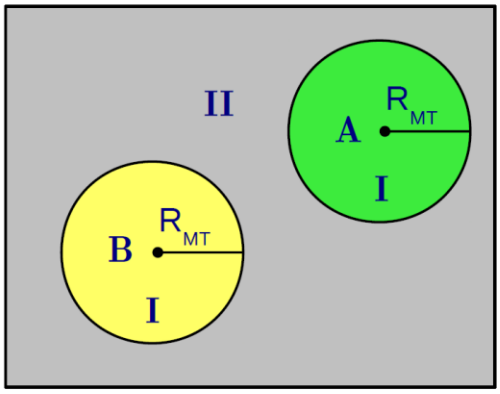

Figure II.2: Schematic division of unit cell containing two types of atoms A and B, in Muffin-Tin spheres (I) and an interstitial region (II).

The APW method uses a plane wave basis set which is especially modified to solve the problem. This adaptation is achieved by dividing the unit cell into (I) non-overlapping atomic spheres (centered at the atomic sites), also known as the Muffin-Tin spheres, and (II) an interstitial region. This is schematically illustrated in Figure II.2 with a unit cell containing two types of atoms: A and B. For the two regions, the electron potential *V*(r) is expanded as:

$$V(\mathbf{r}) = \begin{cases} \sum_{lm} V_{lm}(r) Y_{lm}(\hat{\mathbf{r}}) & (\mathbf{r} \in MT) \\ \sum_{\mathbf{G}} V_{\mathbf{G}} e^{i\mathbf{G}\cdot\mathbf{r}} & (\mathbf{r} \in I) \end{cases} \qquad (2.31)$$

In the two types of regions different basis sets are used:

$$\phi_{\mathbf{k}_n}^{APW}(\mathbf{r}, \epsilon_l) = \begin{cases} \sum_{lm} A_{lm,\mathbf{k}_n} u_l(r, \epsilon_l) Y_{lm}(\hat{\mathbf{r}}) & (\mathbf{r} \in MT) \\ \frac{1}{\sqrt{V}} e^{i\mathbf{k}_n\cdot\mathbf{r}} & (\mathbf{r} \in I) \end{cases} \qquad (2.32)$$

where $k_n = k + G_n$; G_n are the reciprocal lattice vectors, k is the wave vector inside the first Brillouin zone and V is the volume of unit cell.

Inside the atomic spheres (MT), the wave functions are expanded by radial functions times spherical harmonics. u_l (r, E_l) is the (at the origin) regular solution of the radial Schrödinger equation for a spherical potential V (r) for energy E_l,

$$-\frac{1}{r^2}\frac{d}{dr}(r^2\frac{du_l}{dr}) + [\frac{l(l+1)}{r^2} + V(r) - \epsilon_l] r u_l = 0 \qquad (2.33)$$

In the interstitial region (I) plane waves are instead used to build the wave function. The coefficients A_{lm} in the atomic sphere expansion are determined by requiring that the wave functions in the MT and the interstitial regions match each other at the MT boundary.

Thus, each plane wave is augmented by an atomic-like function in every atomic sphere and constitutes thus the basis set used to expand the Kohn-Sham wave function (Ψ),

$$\psi_{\mathbf{k}}(\mathbf{r}) = \sum_n c_n \phi_{\mathbf{k}_n}(\mathbf{r}) \qquad (2.34)$$

The disadvantage in the APW method is that it cannot get the eigenvalues from a single diagonalization due to the unknown parameter E_l in Eq. (2.32). The exact E_l value is needed to describe the eigenstate k(r) accurately. Since this energy depends on the function ul (r, E_l), the

resulting eigenvalue problem is non-linear in energy. Thus, it needs to be solved self-consistently which makes the APW method computationally inefficient.

- **Linearized Augmented Plane Wave (LAPW) method**

In order to overcome the non-linearity problem in the APW method, the LAPW method was developed. The radial wavefunction can be expanded in a Taylor series expansion around E_l as:

$$u_l(r,\epsilon_l) = u_l(r,\epsilon_l^1) + (\epsilon_l - \epsilon_l^1)\dot{u}_l(r,\epsilon_l^1) + O((\epsilon_l - \epsilon_l^1)^2) \qquad (2.35)$$

Where $\dot{u}_l = \delta u_l / exp\delta\epsilon_l$. In this case the radial function error is second order and the energy error is of fourth order. When El1 is set near El the radial function and energy errors are negligible. Thus, the LAPW basis set can be defined as

$$\phi_{\mathbf{k}_n}^{LAPW}(\mathbf{r}) = \begin{cases} \sum_{lm}[A_{lm,\mathbf{k}_n}u_l(r,\epsilon_l) + B_{lm,\mathbf{k}_n}\dot{u}_l(r,\epsilon_l)]Y_{lm}(\hat{\mathbf{r}}) & (\mathbf{r}\in MT) \\ \frac{1}{\sqrt{V}}e^{i\mathbf{k}_n\cdot\mathbf{r}} & (\mathbf{r}\in I) \end{cases} \qquad (2.36)$$

In the interstitial region, the basis set is the same as in the APW method, but in the Muffin-Tin spheres, the basis functions not only depend on u_l, but also on its energy derivative $\dot{u}_l$. Thus, LAPW method offers more flexibility than the APW method in the Muffin-Tin spheres. Now, it is not important to know the exact value of u_l. For a fixed value ofE_l^1, the modified basis functions provide the extra flexibility to cover a large energy region around this linearization energy. The coefficients A_{lm} and B_{lm} are determined by requiring that this basis function matches (in value and slope) each plane wave (PW) which is the corresponding basis function of the interstitial region.

- **APW+lo method**

Another efficient way to linearize the APW method is achieved by the introduction of local orbitals (lo). The basis set of the introduced APW+lo method is also energy independent and still has the same basis size as the original APW method. To allow enough variational flexibility local orbitals are added, which are defined as

$$\phi_{lm}^{lo}(\mathbf{r}) = \begin{cases} [A_{lm}u_l(r,\epsilon_l) + B_{lm}\dot{u}_l(r,\epsilon_l)]Y_{lm}(\hat{\mathbf{r}}) & (\mathbf{r}\in MT) \\ 0 & (\mathbf{r}\in I) \end{cases} \qquad (2.37)$$

The two coefficients A_{lm} and B_{lm} are determined by normalization and by the condition that the local orbital is zero at the Muffin-Tin boundary. The advantage of the APW+lo method is that it has a small basis set like the APW method but with the same accuracy compared to the LAPW method.

II.3.3 Projector augmented wave method (PAW)

An approach that lies half-way between the LAPW and the pseudopotential methods has been introduced by Blöchl [73] known as the projector augmented waves (PAW) method. This approach retains the all-electron character, but it uses a decomposition of the all-electron wave function in terms of a smooth pseudo-wave function, and a rapidly varying contribution localized within the core region. The true and pseudo-wave functions are related by a linear transformation:

$$|\Psi_n^{AE}\rangle = |\Psi_n^{PS}\rangle + \sum_i (|\phi_i^{AE}\rangle - |\phi_i^{PS}\rangle)\langle p_i^{PS}|\Psi_n^{PS}\rangle \qquad (2.38)$$

The pseudo-wave functions Ψ_n^{PS}, where n is the band index, are the variational quantities and are expanded in plane waves. In the regions between the PAW spheres surrounding the atoms, the Ψ_n^{PS}, n are identical to the AE wave functions Ψ_n^{AE}, but inside the spheres Ψ_n^{PS} are only a bad approximation to the exact wave functions, they are used only as a computational tool.

The AE partial waves ϕ_i^{AE} are solutions of the spherical scalar-relativistic Schrödinger equation for a non-spin-polarized atom at a reference energy E_i in the valence regime and for an angular momentum I_i,

$$\left(-\frac{1}{2}\nabla^2 + \nu_{eff}^{AE}\right)|\phi_i^{AE}\rangle = \varepsilon_i|\phi_i^{AE}\rangle \qquad (2.39)$$

where V_{eff}^{AE} is the spherical component of the AE potential. The index i contains the reference energy ε_i the angular momentum quantum numbers (I_i, m_i), and the atomic coordinates $\boldsymbol{R_i}$. The PS partial waves ϕ_i^{PS} are nodeless and identical to the AE partial wave outside a core radius r_c (approximately equal to half the nearest-neighbor distance) and match continuously to ϕ_i^{PS} inside these spheres.

The projector functions p_i^{PS} are constrained to be dual to the partial waves, they are constructed by a two-step procedure: First, intermediate functions χ_i are computed via

$$|\chi_i\rangle = \left(\varepsilon_i + \frac{1}{2}\nabla^2 - \nu_{eff}^{PS}\right)|\phi_i^{PS}\rangle \qquad (2.40)$$

where V_{eff}^{PS} is the spherical component of the effective pseudopotential, which can be chosen arbitrarily inside the radius rc but must match V_{eff}^{AE} for $r \geq r_c$. The projector functions are linear combinations of the χ_i with

$$|\phi_i^{PS}\rangle = \sum_j (B^{-1})_{ji}|\chi_j\rangle, B_{ij} = \langle\phi_i^{PS}|\chi_j\rangle \qquad (2.41)$$

such that the ϕ_i^{PS} and p_i^{PS} are dual, $\langle p_i^{PS}|\phi_j^{PS}\rangle = \delta_{ij}$ and $\langle r|p_i^{PS}\rangle = 0$ for $r \geq r_c$.

II.4 Computational packages

In this section, a brief introduction to the DFT codes that are used throughout this Thesis is given.

II.4.1 Quantum ESPRESSO (QE)

Quantum ESPRESSO [74] stands for op**E**n **S**ource **P**ackage for **R**esearch in **E**lectronic **S**tructure, **S**imulation and **O**ptimization. It is a free software, released under the GNU General Public License. The code is designed to perform density functional theory calculations of the electronic structure. It uses plane wave basis sets and pseudopotential in its applications. Its features range from the calculation of ground-state energy and Kohn-Sham orbitals to the calculation of atomic forces, stresses, and structural optimization, molecular dynamics on the ground state Born-Oppenheimer surface, Nudged Elastic Band (NEB) and Fourier String Method Dynamics. Quantum ESPRESSO is also able to perform other calculations such as; phonon frequencies and eigenvectors at a generic wave vector, effective charges and dielectric tensors, electron-phonon interaction coefficients for metals, Infrared and Raman (non-resonant) cross section etc. [74]. The main advantages of QE over VASP in the context of this work are as follows: first, QE is able to characterize the vibrational frequencies into either Raman or infrared active modes. Secondly, QE assigns modes on the basis of the degeneracy of the vibrational frequencies (single, double or triple). In addition, QE tells you to which irreducible representation a mode belongs. This makes it easy to interpret the results of Raman and infrared spectra.

Quantum Espresso is presently divided into several executable, performing different types of calculations, although some of them have overlapping functionalities. Typically, there is single set of functions or a single Fortran 90 module that perform each specific task, but there are still important exceptions to this rule, reflecting the different origin and different styles of the original components. Quantum Espresso has in fact built out of the merging and re-engineering of different packages.

II.4.2 Vienna Ab initio Simulation Package (VASP)

VASP is a DFT package used for ab-initio quantum-mechanical molecular dynamics simulations by utilizing pseudopotentials or the projector-augmented wave (PAW) method with a plane wave basis set. This is done by using the (finite-temperature) local-density approximation whereby the free energy is used as the variational quantity. The instantaneous electronic ground state is evaluated exactly at each time step of the molecular dynamic. Efficient matrix diagonalization schemes and an efficient Pulay/Broyden mixing for the charge density are used by VASP to avoid possible problems of the original Car-Parrinello method which is basically described by simultaneous integration of the equations of motions for the electrons and ions. Interactions are described by ultra-soft Vanderbilt pseudopotentials (US-PP) or by the PAW method. Both approaches can reduce the number of plane-waves per atom drastically at least for transition metals and first row elements. With VASP one can calculate forces and the full stress tensor which can be used for the relaxation of atoms into their instantaneous ground-state.

CHAPTER III: SIZE AND STRAIN EFFECTS ON THE ELECTRONIC PROPERTIES OF PHOSPHORENE FOR OPTOELECTRONIC DEVICES

Tunability of the electronic properties of 2D materials is crucial for their integration in nanoelectronic devices. Several strategies are commonly used: (1) converting a 2D sheet to 1D structure, such as 1D nanoribbons or nanotubes [75], (2) varying the number of stacked 2D sheets of the same material or constructing van der Waals hetero-layers by stacking different 2D materials [76] or applying either (3) an external electric field [77] or (4) a tensile or compressive strain [78]. In fact, strain is an effective technique that widely used for engineering the electronic properties of 2D materials.

In this Chapter we will explore, using density functional theory, the structural and electronic properties of a phosphorene monolayer, bilayer and trilayer under a uniaxial strain along the armchair (*b* axis) and zigzag (*a* axis) directions. This combined size and strain effect significantly affects the bandgap and the Fermi energy position in phosphorene. Around 0% strain, all phosphorene structures are of p-type, while they switch to an n-type semiconductor in the range of strain values from +2% up to +14%. This p-type to n-type transition may have a major technological impact in fields where mono- and hetero-junctions are considered.

III.1 Motivation

Developing alternatives to the silicon-based materials remains one the most challenging issues to improve the performance of devices in the electronics industry [79,80]. To face this problem, researchers have sought several approaches to engineer the electronic properties of the existing materials including nano-structuring [81,82], substrate engineering [83], or applying an electric field [84].

For decades, tuning the electronic properties of materials by means of strain has been proven to be a practical and yet an effective mechanism that offers an interesting degree of flexibility to expand the range of their applications in nanoelectronics [85,86]. In particular, it was found that dimensionally-reduced nanostructures such as two-dimensional (2D) materials can maintain stability under much larger strain-magnitudes than that applied to their bulk counterparts [87-89]. For example, graphene and 2D-MoS_2 were reported to endure 15% and 11% of strain, respectively, without damaging their structures [90,91]. In addition, it has been computationally shown that a phosphorene monolayer can resist a tensile strain up to 30% [92], a value that is superior to those values corresponding to other 2D materials like graphene or 2D-MoS_2. In this context, phosphorene, with its high structural anisotropy [93], is in fact expected to reveal a response to strain but little is known about the variation of its intrinsic electronic properties, particularly the Fermi level position. In fact, many groups reported that the bandgap of phosphorene can be modulated through different approaches such as nanostructuring (nanoribbons or nanotubes) and heterostructuring [94]. However, we believe that the effect of strain and size interplay on the electronic properties of phosphorene is still not fully explored and must also be investigated in depth. In terms of strain-compensation, the parameters that compensate the strain effect as a function of layers number is not clearly elucidated. For all these reasons, we performed in the present chapter a comprehensive computational study that investigates both effects by exploring the behavior of structural and electronic properties of a phosphorene monolayer, bilayer and trilayer under a uniaxial strain.

III.1.1 Strain Engineering

Nanostructured materials can withstand extremely large deformation without mechanical failure compared with their conventional counterparts, opening up a vast parameter space for

rational engineering of materials properties by strain. The electronic, optical, thermal, and chemical properties of crystals are functions of the six-dimensional elastic strain tensor ε ($\varepsilon_1 = \varepsilon_{11},\ \varepsilon_2 = \varepsilon_{22},\ \varepsilon_3 = \varepsilon_{33},\ \varepsilon_4 = \varepsilon_{23},\ \varepsilon_5 = \varepsilon_{13},\ \varepsilon_6 = \varepsilon_{12}$ following the so-called Voigt notation). Electronic bandgap E_g opens or closes with ε, resulting in drastic alteration of the electrical, thermal, optical, and magnetic characteristics [95]. With the spread of ultra-strength nanostructured materials that can sustain a wide range of nonhydrostatic and potentially dynamically varying stresses [96], and various miniaturization-enabled means of applying ε [97], a new window of opportunity has now opened up to scan a vast unexplored space for the development of materials and devices with desirable combinations of physical and functional properties [98]. For example, while it is well known that unstrained Si has an electronic bandgap of 1.1 eV, we know that when it is subjected to a biaxial strain of 5%, it would have a different bandgap. At large strains, all these differently strained pure Si crystals would not behave as the unstrained "typical silicon." It should be also noted that, not only the value of E_g, but also its character (e.g., direct or indirect), and its semiconducting type can be changed with ε.

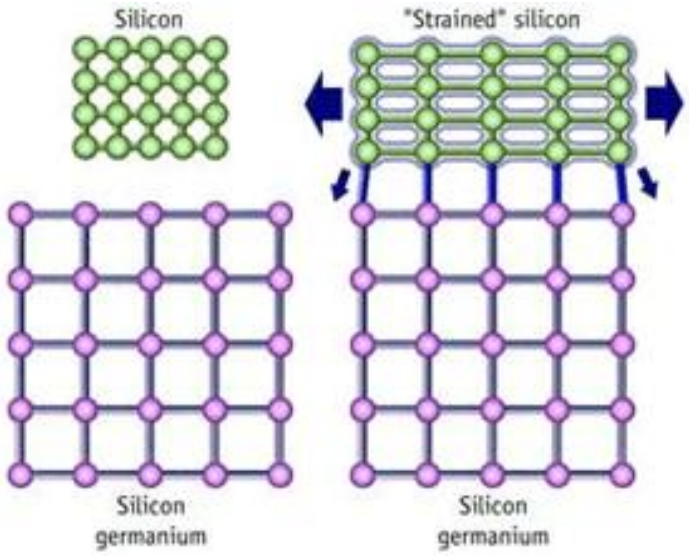

Figure III.1: Illustration of strained Silicon after deposition on a Germanium substrate.

III.1.2 Strain Applications

Over the past two decades, strain engineering has achieved one considerable commercial success [99]: strained silicon technology, where a biaxial elastic strain of the order of 1% applied

to a thin channel of silicon enhances the mobility of charge carriers by more than 50% and increases Central Processing Unit (CPU) clock speed correspondingly. Recent studies have shown that nanowires of silicon can sustain a tensile elastic strain of as much as 16% [100], while nanoscale needles of diamond can be bent to a local maximum tensile elastic strain in excess of 9% [101]. As discussed by Zhe Shi et al. [102], if the ability of Si and C to deform up to strains of these magnitudes under certain conditions is exploited, there exist much greater possibilities than what is currently realized for engineering of band structure and bandgap for a wide variety of electronic, optoelectronic, and photonic materials employed in communication, information, and energy applications that impact every aspect of modern life [103].

III.2 Computational Details

Phosphorene, as experimentally exfoliated from its bulk counterpart Black Phosphorus (the most stable allotrope of phosphorus) [104,105] has attracted great attention due to its interesting properties such as its experimentally measured direct optical bandgap of 1.75 eV [106], an intrinsic p-type conduction and a high carrier mobility of 1000 $cm^2.V^{-1}.s^{-1}$ [104]. Our calculations were performed within the framework of density functional theory as implemented in the Quantum ESPRESSO package [107]. The generalized gradient approximation (GGA) in the form of the Perdew−Burke−Ernzerhof (PBE) functional and the projector augmented wave (PAW) potentials [108] were considered alongside with the effect of van der Waals (vdW) interactions in the form of the DFT-D2 correction [109]. To better estimate the bandgap, the hybrid functional HSE06 [110] is used for monolayer phosphorene to give a direct bandgap of 2.03 eV (very close to the experimental value [105]); however, we limited our calculations of strained phosphorene to the GGA-PBE + vdW-DF2 approximation as it is well known that the HSE06 is very consuming in terms of computational-time. The plane wave cut-off for all calculations was set to 40 Ry and the atomic relaxation was performed with an energy convergence of 10^{-5} Ry and a force convergence of 10^{-4} Ry per Bohr. A unit cell of phosphorene with periodic boundary conditions is used with a vacuum of 15 Å in the perpendicular direction to the surface in order to avoid interactions between periodic images. K-point samplings of 6×4×1 were used for the structure relaxation, while denser meshes of 18×12×1 were used to calculate the electronic properties. Under uniaxial strain along the zigzag direction (along *x*) or in the armchair direction (along *y*), *a* and *b* lattice constants were

varied in order to simulate either a compression or a tension, while the relaxation of the crystal is freely performed along the *c* axis and along the transverse axis for each *a*(*b*) fixed value. This uniaxial strain is expressed as: $\varepsilon_x(\%) = \frac{a - a_0}{a_0}$ and $\varepsilon_y(\%) = \frac{b - b_0}{b_0}$, where *a*(*b*) and $a_0(b_0)$ are the lattice constants along the *x*(*y*) direction of strained and unstrained structures, respectively. The compression is represented by negative values while expansion corresponds to positive ones.

III.3 Unstrained Phosphorene

III.3.1 Structural properties of unstrained ML, BL and TL phosphorene

Like graphite, black Phosphorus is a layered material in which atomic layers are bound by van der Waals (vdW) interactions and exhibits AB stacking. In each single layer of bP, phosphorus atoms form a puckered and hexagonal structure as shown in Figures III.2. Our calculated and relaxed lattice constants for bulk BP are: *a* = 3.315 Å, *b* = 4.561 Å and *c* = 11.28 Å (as determined using GGA-PBE approximation) are in good agreement with experiment (*a* = 3.31 Å, *b* = 4.37 Å and *c* = 10.48 Å) [111,112]. On this basis, our starting phosphorene monolayer (ML) structure corresponds to a single layer in such a relaxed BP. The phosphorene bilayer (BL) and trilayer (TL) structures correspond then to two single-layers and three single-layers, respectively. As can be seen in Figure III.2, other important structural features are those corresponding to the puckering height (or distance) (Δ) and the interlayer distance (*d*).

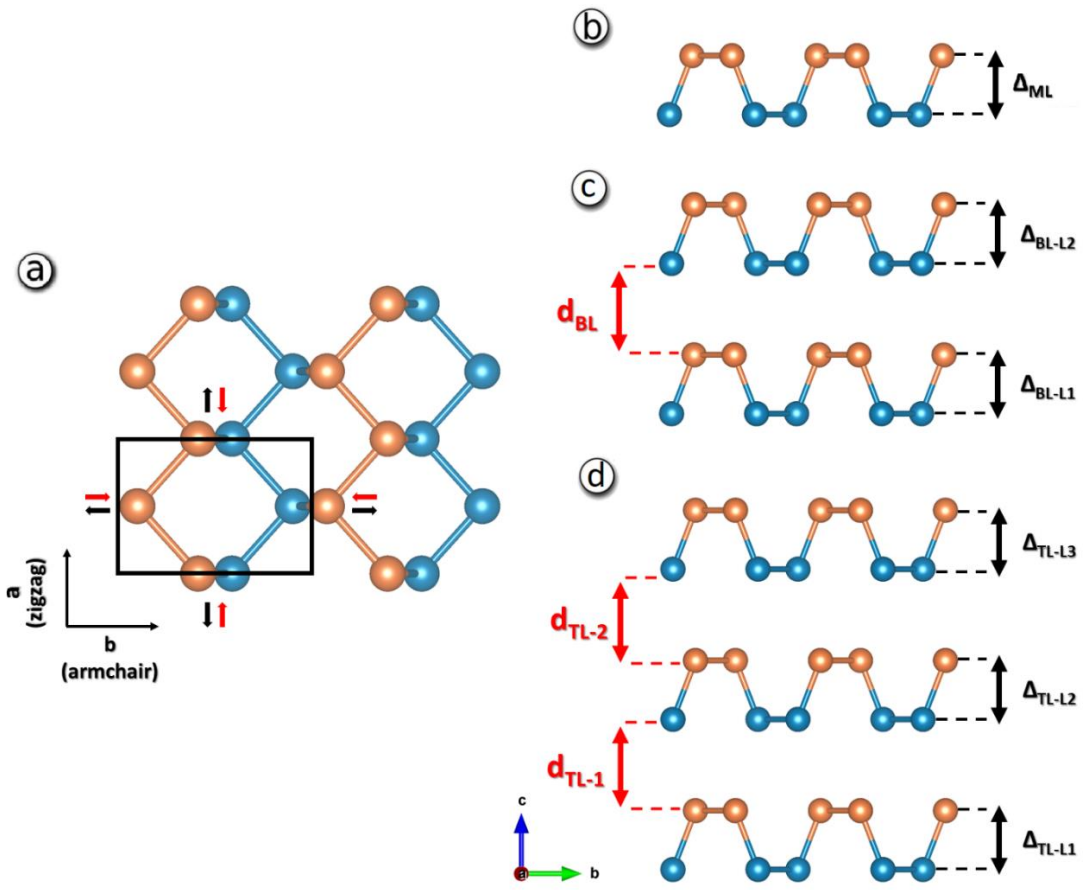

Figure III.2: (a) Top view of monolayer phosphorene; (b), (c) and (d) are side views of monolayer (ML), bilayer (BL) and trilayer (TL) phosphorene respectively. Δ and d denote the puckering and interlayer distances, respectively. Orange spheres are top-front P atoms and blue spheres are back-front P atoms.

Using the GGA-PBE approximation, relaxation of the three structures (ML, BL and TL) results are summarized in Figure III.3. We first notice that in the case of a ML the *a* parameter is stretched while that of *b* is elongated, as compared to those of the bulk BP, which looks like a reasonable tendency to a self-flattening of the ML. By adding more layers (BL and TL) the "*a*" parameter tends to increase with increasing the layers number while the "*b*" parameter is decreased. This trend, which validates our approximation of choice, can simply be explained by the fact that both parameters tend to converge towards those of BP-bulk parameters. It is also very interesting to note that Δ_{TL-L2} exhibits a higher value as compared to those of Δ_{TL-L1} and Δ_{TL-L3}, while those for the BL structure (Δ_{BL-L1} and Δ_{BL-L2}) show a similar value. This implies that TL phosphorene is subjected to a relaxation of the top and bottom layers pushing therefore these layers (Δ_{TL-L1} and

Δ_{TL-L3}) to reduce their puckering heights, while that of the inner-layer remains closer to that of the bulk value. Likewise, it is noted that d_{TL-1} and d_{TL-2} show a higher value as compared to d_{BL} due to the induced repulsion between the inner-layer and the top and bottom layers. This result suggests that the *d* parameter will tend to converge towards that of the BP-bulk value when the number of layers is increased.

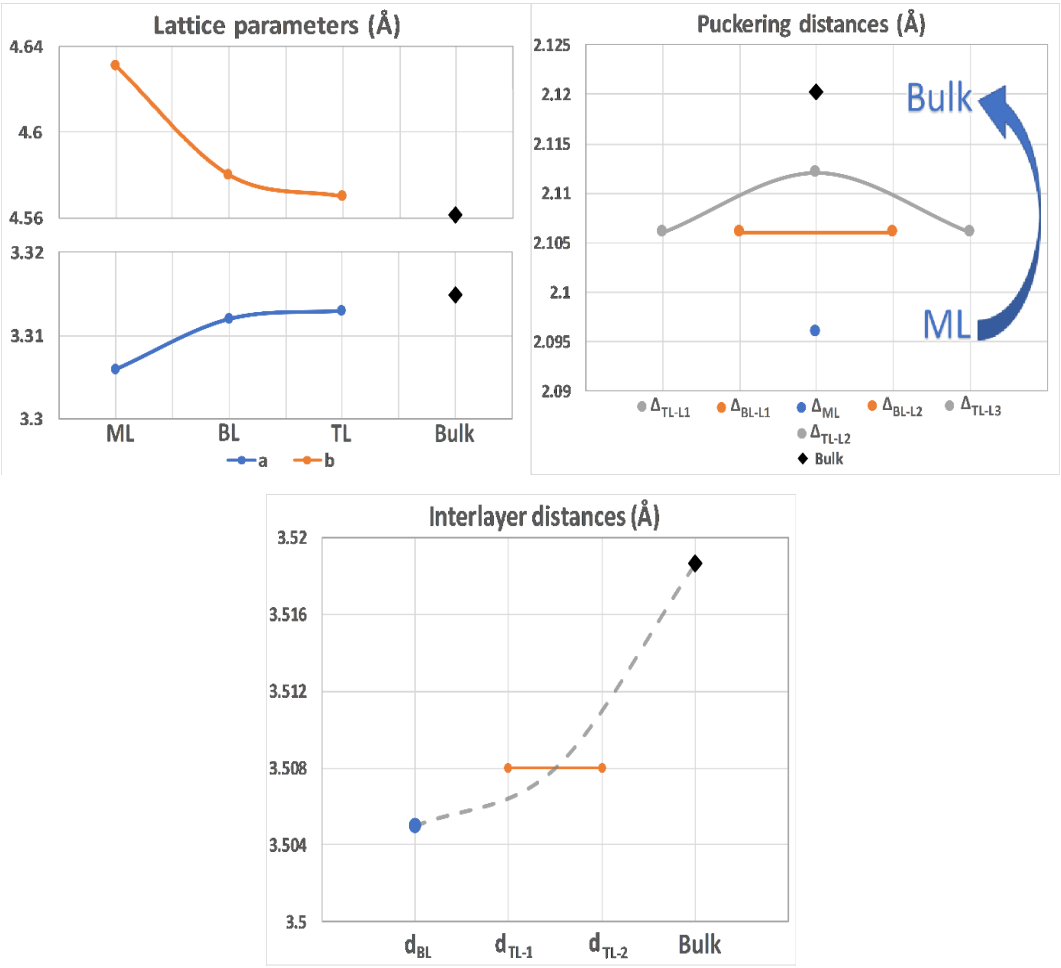

Figure III.3: Calculated structural parameters of ML, BL and TL phosphorene obtained with GGA-PBE approximation.

In fact, comparison with reported studies (*a* = 3.29 Å and *b* = 4.63 Å for ML) [113,114] indicates that GGA-PBE is the functional that best matches the reported theoretical lattice constants. However, it is known that van der Waals interactions play a major role in the electronic properties of layered materials, and they must therefore be considered. For such a reason, we

calculated total energies E_{total} for ML, BL and TL systems by employing different vdW corrections to the GGA-PBE. Our calculations indicate that the minimum energy for all systems corresponds to those configurations calculated with the vdW-DF2 correction as presented in Figure III.4. On this basis, we will in the following use the vdW-DF2 correction combined with fixed lattice parameters from GGA-PBE to calculate the electronic structure of unstrained phosphorene.

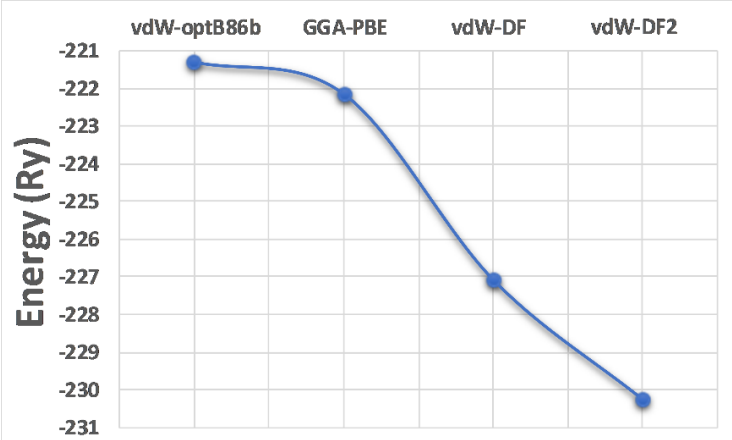

Figure III.4: Calculated total energy (E_{total}) for monolayer phosphorene as a function of different van der Waals corrections (vdW-optB86b, vdW-DF and vdW-DF2) as compared to the GGA-PBE approximation.

III.3.2 Electronic properties of unstrained ML, BL and TL phosphorene

From the calculated band structures corresponding to ML, BL and TL structures (Figures III.5), it can be observed that all of them exhibit a direct bandgap at Γ point with similar features in terms of their spectrum, except for the bandgap variation as a function of the number of stacked layers. As the latter increases, the bandgap value decreases as shown in Figure III.5d.

Although the GGA-PBE approximation is well known to underestimate the bandgap value [115], the size-effect is clearly evidenced which is mainly due to a band splitting occurring over the entire Brillouin zone and more specifically at the valence band maximum (VBM) and the conduction band minimum (CBM).

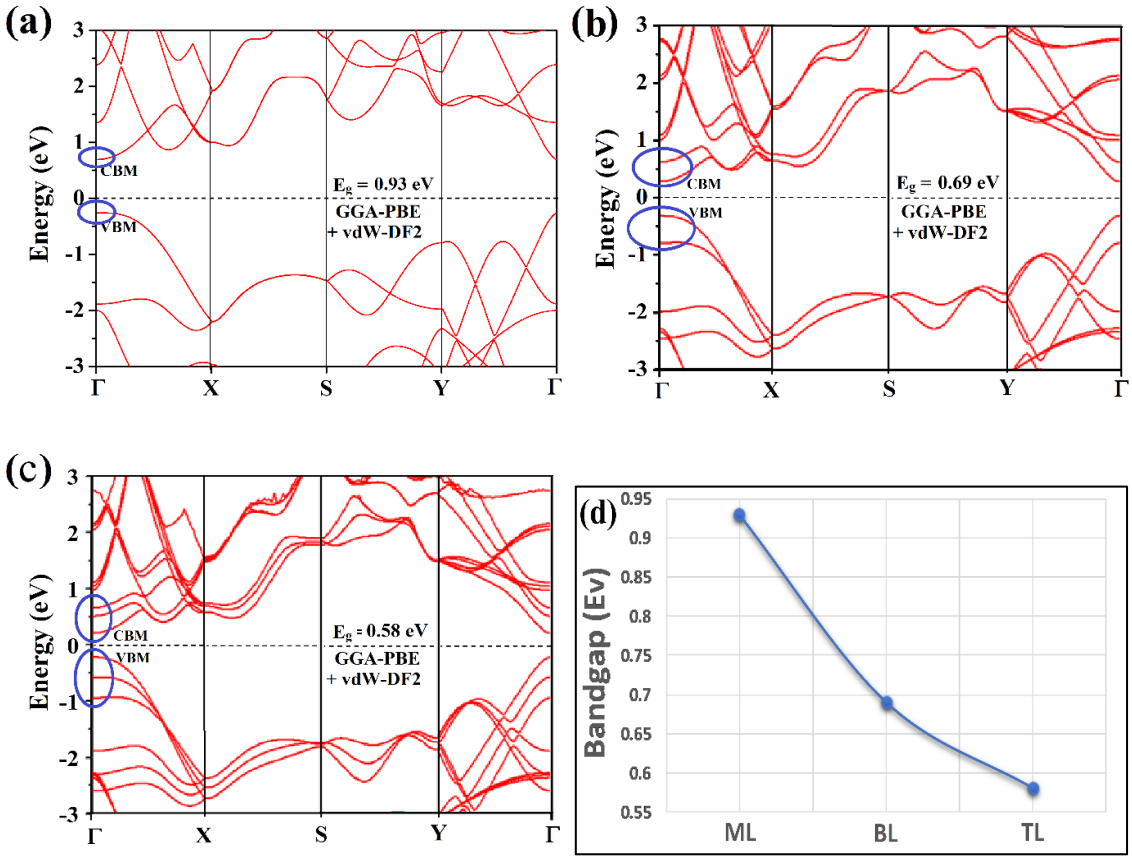

Figure III.5: Band structure of (a) ML, (b) BL and (c) TL phosphorene. (d) Bandgap energy (*E*g) as a function of number of layers.

III.4 Strained Phosphorene

III.4.1 Structural properties of strained ML, BL and TL phosphorene

To study the uniaxial strain effect on the ML, BL and TL structures, it is worth recalling that phosphorene presents a structural anisotropy [116,117] within its layer, usually called armchair and zigzag directions, as illustrated in Figure III.2a. Based on the relaxed structure of the ML phosphorene, we have considered a series of uniaxial strains ranging from -14% to +24% along the armchair direction and from -12% to +20% along the zigzag direction as displayed by dark and red arrows in Figure III.2a. Strain values were chosen on the basis of previous reports [92] where tensile strain for phosphorene has shown a limit of 30% and 27% along the armchair

and zigzag directions, respectively, after which a plastic deformation occurs resulting in an irreversible distortion of the phosphorene structure. As can be seen from Figures III.6a-6b, exercising a uniaxial strain along the armchair direction (*b* axis) significantly increases the *b* lattice parameter for positive strain values (and vice versa) while *a* and Δ_{ML} lattice parameters exhibit a smaller decrease for the whole range of strain (from 2.16 Å at -14% to 1.91 Å at +24% for Δ_{ML}). When applying a uniaxial strain along the zigzag direction (*a* axis), however, the *a* and *b* lattice parameters follow an opposite behavior with respect to each other for the whole strain range while that of the Δ_{ML} parameter remains almost unchanged (from 2.11 Å at -14% to 2.16 Å at +24%). From the above findings, strain along the armchair direction (*b* axis) tends to compensate the increase of the *b* lattice parameter by those of *a* and Δ lattice parameters simultaneously. Along the zigzag direction (*a* axis), however, variation of the *a* lattice parameter is only compensated by that of the *b* lattice parameter. This behavior is then very specific to the ML phosphorene as a consequence of its structural anisotropy.

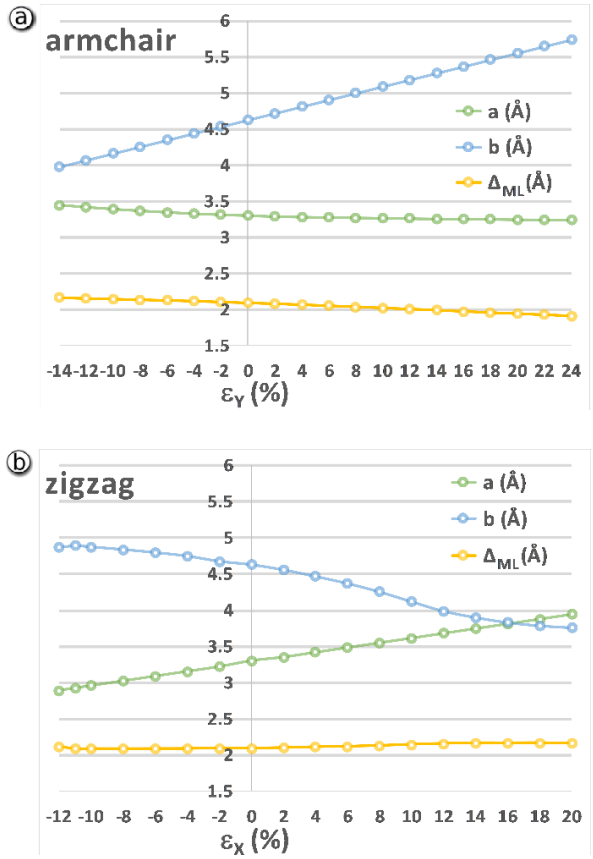

Figure III.6: Calculated lattice parameters of ML phosphorene under uniaxial strain along (a) the armchair direction or (b) the zigzag direction.

Similarly, it can be noticed that for both strain directions, the BL and TL structures behave the same way as the ML structure over the whole range of strain (Figures III.7a-7c and III.8a-8c). Indeed, the Δ parameter seems to be unaffected along the zigzag direction (for all layers) while it is slightly varied along the armchair one (Figures III.7b-7d and III.8b-8d). Our results clearly indicate that for the BL and TL structures, the *d* parameter acts as an additional degree of liberty for strain compensation. Indeed, the increase of the *b* lattice parameter under strain along the armchair direction (*b* axis) is simultaneously compensated by those of *a*, *d* and Δ lattice parameters, while along the zigzag direction (*a* axis) variation of the *a* lattice parameter is only compensated by those of *b* and *d* lattice parameters. In terms of the variation weight under strain, distortion of the *b* lattice parameter along the armchair direction (*b* axis) seems to be mainly supported by the *b* lattice array itself, while that of the *a* lattice parameter along the zigzag direction (*a* axis) the distortion is equally shared between both lattice arrays, *a* and *b*.

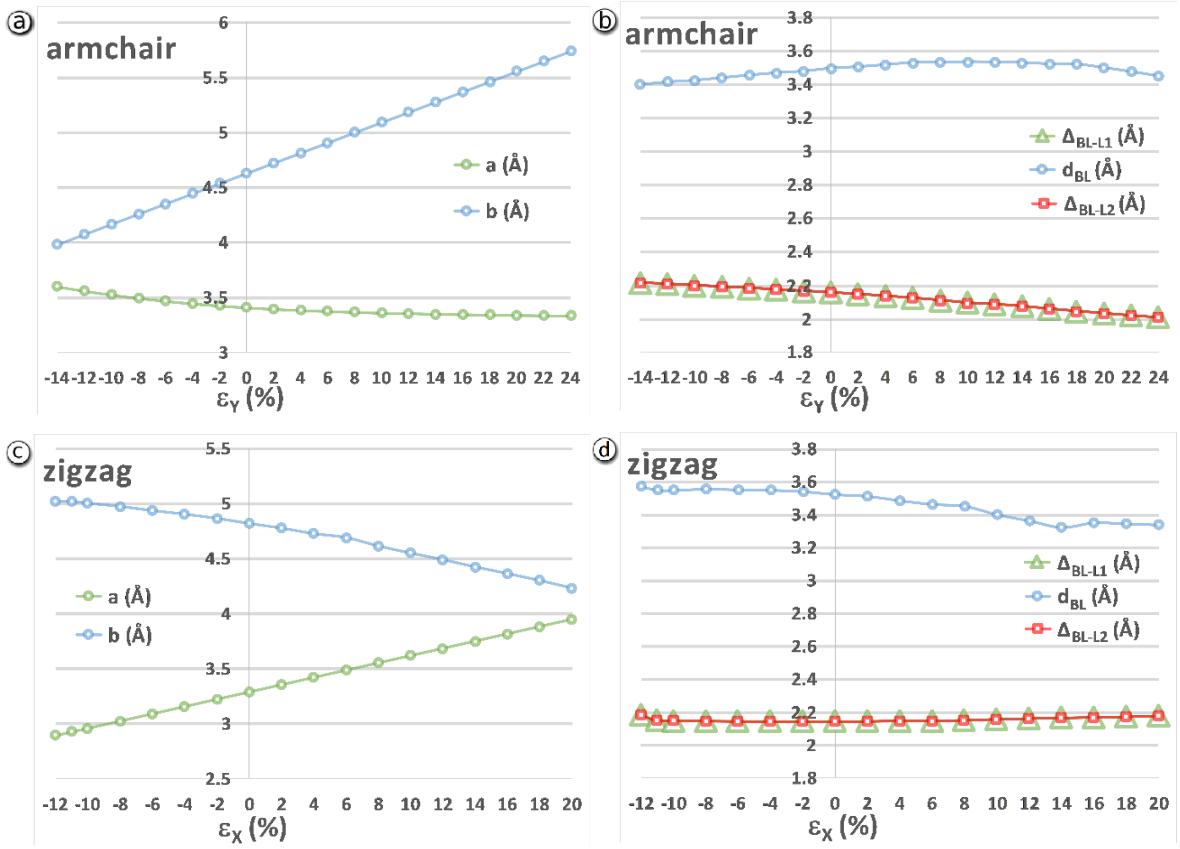

Figure III.7: Calculated lattice parameters of BL phosphorene under uniaxial strain along (a)-(b) the armchair direction and (c)-(d) the zigzag direction.

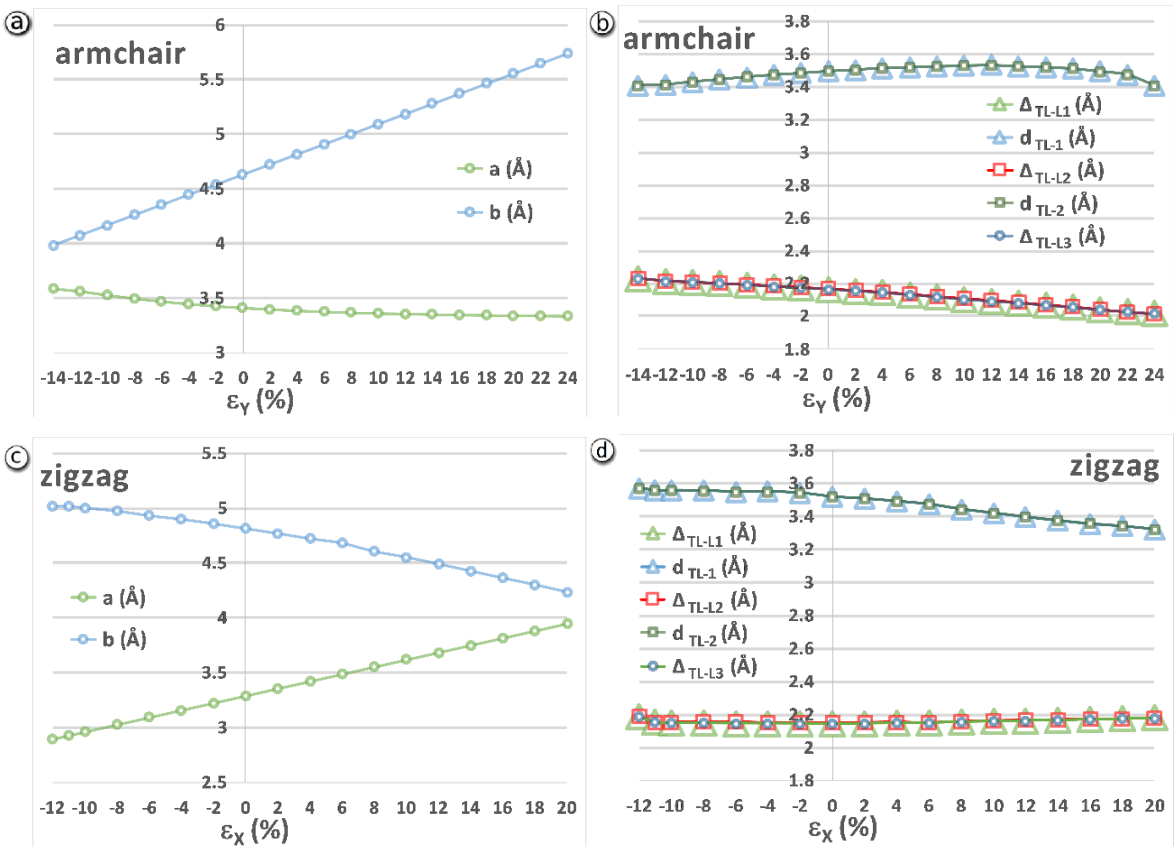

Figure III.8: Calculated lattice parameters of TL phosphorene under uniaxial strain along (a) and (b) the armchair direction or (c) and (d) the zigzag direction.

III.4.2 Electronic properties of strained ML, BL and TL phosphorene

To further explore the strain effect on the electronic properties of ML, BL and TL phosphorene structures, the bandgap as a function of uniaxial strain is plotted in Figure III.9. As a general remark, we noticed that strain applied either on the armchair (Figure III.9a) or zigzag (Figure III.9b) direction tends to change the nature of the bandgap from a direct to an indirect electronic transition as a function of the strain value. The strain-range for a direct electronic transition is narrower for a ML, as compared to that for a BL or a TL structure. Strain can then be modulated to obtain a direct transition, for optoelectronic applications for instance, as a function of the layers number. In addition, it is shown that from -14% to +6%, negative strain values provoke a decrease of the bandgap value while positive strain values tend to increase the bandgap value. Within this strain-range, ML, BL and TL structures behave therefore like most

semiconductors under strain where compressive strain blueshifts the bandgap and tensile strain redshifts it. It is important to notice that in these figure cases, size and strain effects simultaneously contribute to the bandgap value. This combined effect is an exceptional alternative for tuning the phosphorene bandgap. Surprisingly, we found that this tendency is stopped up to +6% strain where the bandgap for all structures reaches its maximum value, and then starts to decrease again for higher positive strain values. A similar critical strain value has also been reported by Wang et al. [114] and found to be related to charge distribution of electronic states near the Conduction Band Minimum (CBM) and Valence Band Maximum (VBM).

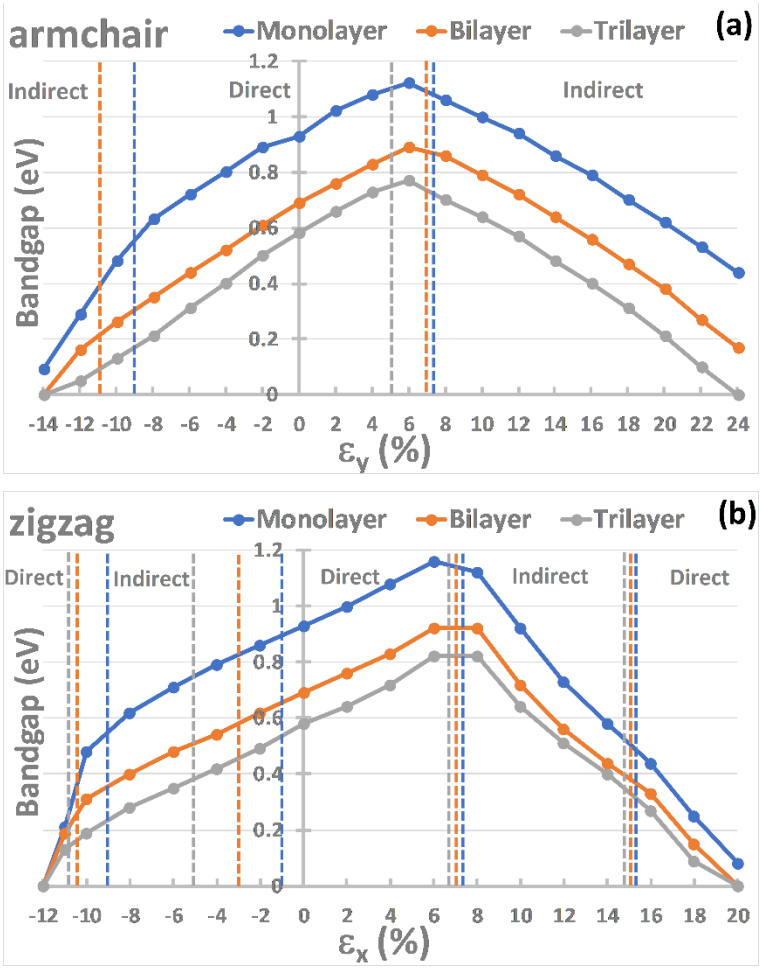

Figure III.9: Calculated bandgap of ML (blue), BL (orange) and TL (gray) phosphorene under uniaxial strain along (a) the armchair direction and (b) the zigzag direction.

III.4.3 p-type to n-type transition in strained ML, BL and TL phosphorene

To gain additional insight on the bandgap variation for all phosphorene structures under strain, we examined the variation of VBM and CBM bands as a function of armchair and zigzag strain directions, as plotted in Figure III.10. Generally, one observes that both bands show an energy decrease but that of VBM exhibits a rapid decrease as compared to that of the CBM as a function of strain, where the critical +6% strain value corresponds to the largest bandgap as already described in Figure III.9. Interestingly, Figure III.10 also shows that both armchair and zigzag strain directions have a significant effect on the Fermi energy position that determines the semiconductor type [118] (*n* or *p*). Indeed, BP is well known to be a p-type impurity semiconductor at low temperature [119]. The conductivity is entirely due to the holes with a much faster mobility than that of electrons. When reduced to a ML, a BL or even a TL, the structure remains of *p-type* as can clearly be seen at 0% strain. In the case of armchair strain direction, the Fermi level of a ML shifts to the CBM side as soon as a positive strain is started (+2%) which switches the compressed ML to an *n-type* semiconductor. As compared to BL and TL structures, the ML structure has the largest strain range where it can be switched to an *n-type*, a range that starts from +2% up to +14% strain-values. In the case of zigzag strain direction, the same trend is also noticed although slightly complicated since the range for the *n-type* formation is reduced.

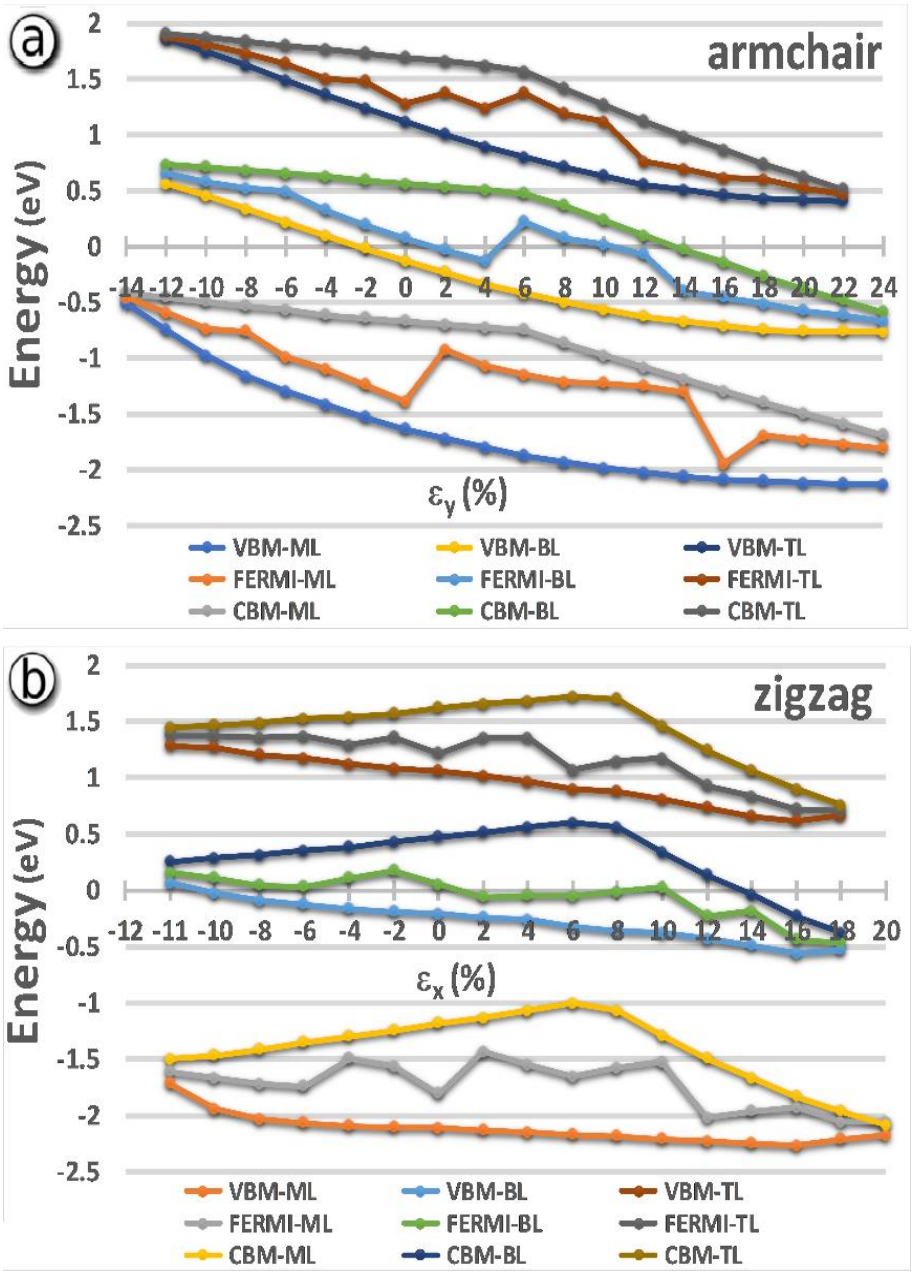

Figure III.10: Valence Band Maximum (VBM), Conduction Band Minimum (CBM) and Fermi level of ML, BL and TL phosphorene under strain along (a) the armchair direction and (b) the zigzag direction. All data points are plotted.

To verify our findings, carrier concentrations were calculated, as presented in Table III.1 for ML phosphorene, and found to agree with the Fermi levels plotted in Figure III.10 in terms of which carrier concentration (holes or electrons) is dominant. At extreme-values, we can notice that

the Fermi level increases with compression and decreases with extension which is mainly attributed to the charge density which proportionally alters these Fermi levels. Still, the Fermi levels between those extremities are not showing a stable variation which is due to the fact that DFT underestimates these energy levels. However, we believe that our findings provide an interesting insight on the strain-induced type transition in phosphorene. This ability to switch the semiconductor type may have a major technological impact in fields where monojunctions are needed.

Table III.1: Carrier concentrations of holes (p) and electrons (n) for ML phosphorene under strain.

	armchair strain (%)							
	-12	-8	-4	0	4	8	12	16
p (cm^{-2})	$4.3x10^{17}$	$3.7x10^{16}$	$3.3x10^{17}$	$3.4x10^{15}$	$2.2x10^{14}$	$5.8x10^{14}$	$2.2x10^{14}$	$7.2x10^{19}$
n (cm^{-2})	$2.5x10^{18}$	$3.9x10^{17}$	$2.5x10^{15}$	$1.1x10^{13}$	$5.2x10^{16}$	$6.9x10^{16}$	$3.5x10^{18}$	$2.8x10^{14}$
	zigzag strain (%)							
	-11	-8	-4	0	4	8	12	16
p (cm^{-2})	$6.6x10^{19}$	$7.5x10^{15}$	$2.2x10^{13}$	$3.4x10^{15}$	$1.7x10^{15}$	$1.4x10^{13}$	$1.7x10^{18}$	$2.7x10^{16}$
n (cm^{-2})	$1x10^{19}$	$1.9x10^{17}$	$1.4x10^{18}$	$1.1x10^{13}$	$2.9x10^{15}$	$1.8x10^{15}$	$9x10^{14}$	$2.8x10^{18}$

III.5 Size-reduced Phosphorene Nanostructures

Besides the size and strain effects, several strategies can be used to tune the electronic properties of 2D materials. In fact, one way to do that would be by reducing their size rather than increasing it. In what follows, we extended our study to engineer the bandgap of phosphorene by converting its 2D sheets into 1D nanostructures in the form of nanoribbons and also by edge-passivating these 1D structures with Hydrogen. Our study reveals that the electronic properties of the 1D phosphorene are very flexible and several approaches could be adopted to engineer them.

III.5.1 Phosphorene Nanoribbons (PNRs)

The electronic properties of PNRs are highly dependent on the crystal orientation of the ribbons. Figure III.11 illustrates the structures of the armchair and zigzag PNRs with unpassivated edges (the periodicity is along the direction of the ribbon). The computed a-PNRs and z-PNRs were truncated from monolayer phosphorene along the b- and a-directions, respectively, and the

width of the ribbon is referred to according to the number of the hexagonal rings in the direction perpendicular to the ribbon direction; in our case it is a 5-rings armchair and zigzag PNRs.

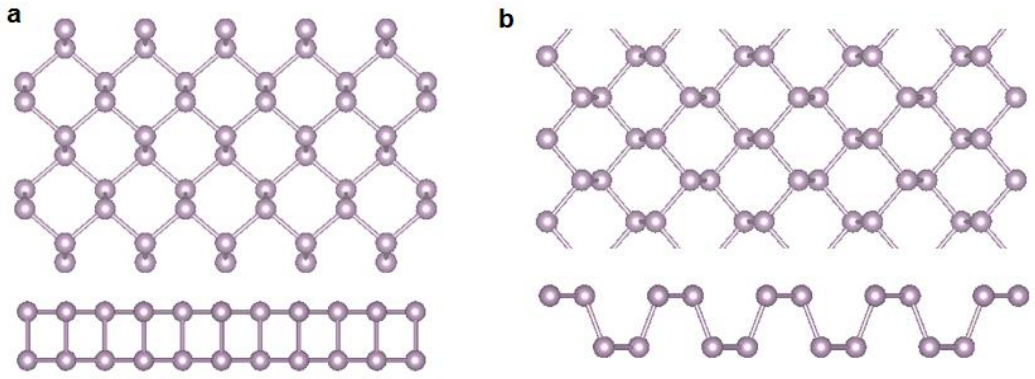

Figure III.11: Top and side views of the (a) 5-armchair and (b) 5-zigzag (PNRs) with unpassivated-edges.

The electronic structure of the edge-unpassivated 5-zigzag PNR is computed (Figure III.12b), and exhibits a metallic behavior. The electronic states contributed by the edge atoms of the 5-zigzag PNR are located around the Fermi level and close up the band gap. Contrary to metallic character of the edge-unpassivated z-PNRs, the edge-unpassivated 5-armchair PNR is a semiconductor with an indirect bandgap (Figure III.12a). For the 5-armchair PNR, the CBM is not located at the Γ point while the VBM is at Γ, which gives an indirect gap. The computed bandgap value in this case is 0.50 eV (GGA-PBE).

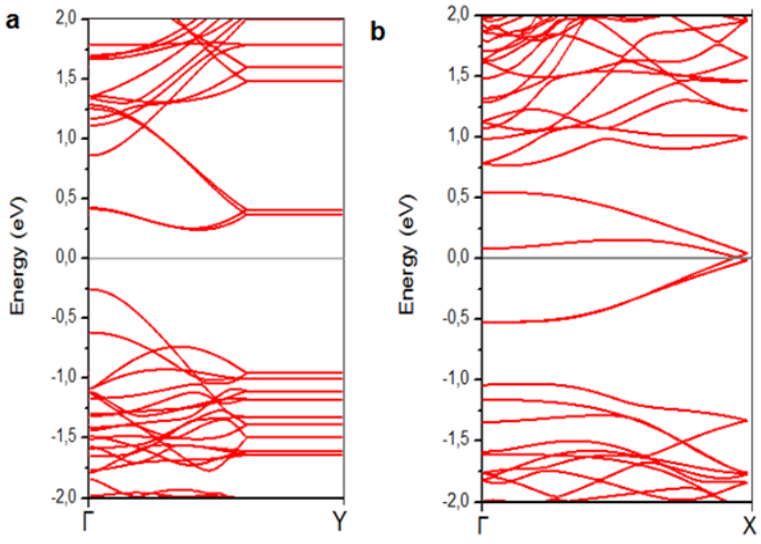

Figure III.12: Computed band structures (PBE) of the edge-unpassivated (a) 5-armchair and (b) 5-zigzag PNRs.

III.5.2 Hydrogen edge-passivated PNRs

One commonly used method to modulate the bandgap of nanoribbons is by passivating their edges with different groups of atoms. In fact, it was reported in other studies [120] that the edges of a nanoribbon play a direct influence on its electronic structures. Therefore, it is of crucial importance to study the edge-passivation of the PNRs. Figure III.13b indicates that in a stark contrast of the metallic behavior observed for the edge unpassivated z-PNRs, our PBE calculations show that the Hydrogen edge-passivated z-PNRs exhibit a nearly direct bandgap of 1.37 eV. This is due to the fact that with the hydrogen passivation, the contribution of the edge states to the Fermi level region disappears, thereby leading to the metal-to-semiconductor transition. Also, for the H-edge-passivated a-PNRs (Figure III.13a), the computed band structure (PBE) shows that the a-PNRs are still semiconductors with a direct bandgap of 0.97 eV as compared to the indirect bandgap for edge-unpassivated a-PNRs. Therefore, we can say that the edge passivation of the 1D PNRs structures is considered as an effective strategy into tuning their electronic properties.

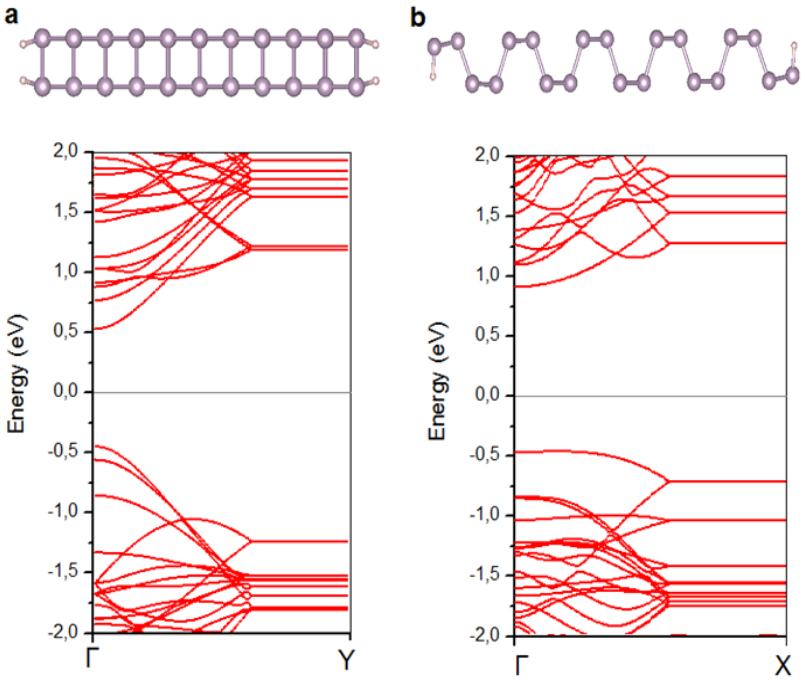

Figure III.13: Computed band structures (PBE) of the H-edge passivated (a) 5H-armchair and (b) 5H-zigzag PNRs. Purple spheres represent P atoms while white spheres represent H atoms.

III.6 Conclusion

In conclusion, we have reported in this chapter a detailed first-principles study on the strain and size effects interplay where both structural and electronic properties of a phosphorene monolayer, bilayer and trilayer under a uniaxial strain are explored. Our calculations show that strain along the armchair direction (*b* axis) provokes a distortion of the *b* lattice parameter which is mainly compensated by the *b* parameter itself, while that of the *a* lattice parameter along the zigzag direction (*a* axis) the distortion is equally shared between both parameters; *a* and *b*. In addition, the applied strain either on the armchair or zigzag direction tends to change the nature of the bandgap from a direct to an indirect electronic gap as a function of the strain value. However, we find that within a strain ranging from -14% to +6%, the ML, BL and TL structures behave like most semiconductors under strain where compressive strain blueshifts the bandgap and tensile strain redshifts it. Surprisingly, this trend is inverted for strain values higher than +6%. Finally, a very interesting strain-size combined effect is observed on the VBM and CBM bands where the Fermi level shifts from one side to another of the energy gap. While the ML, BL and TL structures are of p-type at 0% strain, they switch to n-type semiconductors under strain ranging from +2% up to +14%. We believe that this p-type to n-type transition ability may have a major technological impact in fields where mono- and hetero-junctions are needed.

In addition, an examination of the tunability of the bandgap of phosphorene is investigated by reducing the size of 2D phosphorene into 1D phosphorene nanoribbons (PNRs). We showed that the edge-unpassivated zigzag PNRs are metallic while armchair PNRs are semiconductors with indirect bandgaps. We reported that both their electronic structures can be adjusted with Hydrogen edge-passivation, z-PNRs become semiconductors with a nearly direct bandgap while a-PNRs become semiconductors with a direct bandgap.

These findings reveal that the bandgap and electronic structure of the black phosphorus derivatives are very flexible and several approaches could be adopted in order to engineer them hence, leading a very important role towards their integration in optoelectronic devices.

CHAPTER IV: ADSORPTION AND DIFFUSION BEHAVIORS ON A PHOSPHORENE MONOLAYER FOR ENERGY STORAGE DEVICES

In this Chapter, density functional theory calculations, including van der Waals interactions, have been carried out in order to evaluate the prospects of phosphorene as an anode material for different rechargeable batteries by exploring the adsorption and diffusion behaviors of alkali (Li, Na and K) and alkaline earth-metal (Be, Mg and Ca) atoms on a phosphorene monolayer. Our binding energy calculations over various adsorption sites showed that the site located above the triangle center composed of three phosphorous surface atoms is the most attractive to all adatoms.

In addition, simulation of the diffusion of the above adatoms over the surface of a phosphorene monolayer was found to be anisotropic, with the lowest diffusion-energy being that of K (0.02 eV) along the zigzag pathway. To the best of our knowledge, this is the lowest diffusion barrier among any other metal adatom on a phosphorene single layer. While phosphorene clearly exhibited a higher performance than graphene in terms of adsorption and diffusion, it showed however a lower storage capacity than the later most probably due to a structural distortion provoked by oversaturated surfaces. This finding strongly suggests that a phosphorene-graphene hybrid system constitutes a promising high-capacity ion-anode.

IV.1 Motivation

Energy storage remains the chief inhibitor in our quest to move from fossil fuel-derived energy to that which we can collect from the sun, wind, and ocean waves. These three energy sources suffer from one common problem, intermittency. If we can store the excess of energy we can derive from them, then the intermittency problem is solved. Indeed, the increasing demand of energy storage technologies for the portable electric devices and electric vehicles has promoted extensive research on high power density as well as long cycle and calendar life rechargeable energy systems such as Li-ion batteries (LIBs).

Lithium-ion batteries continues to be the most widely used storage technology nowadays, making up nearly 85% of all new capacity installed, and are present in laptops, mobile phones and in hybrid and fully electric vehicles. However, lithium is expensive and resources are unevenly distributed across the planet. Large amounts of drinking water are used in lithium extraction and extraction techniques are becoming more energy intensive as lithium demand rises. With the ever-increasing demand for electric cars, the need for reliable rechargeable batteries is rising dramatically, so there is keen interest in finding a charge carrier other than lithium that is cheap and easily accessible. Sodium is inexpensive and can be found in seawater so is virtually limitless. However, sodium is a larger ion than lithium, so it is not possible to simply "swap" it for lithium in current technologies. For example, unlike lithium, sodium will not fit between the carbon layers of the ubiquitous LIB anode, graphite. Hence, the need to find new alternatives for LIBs.

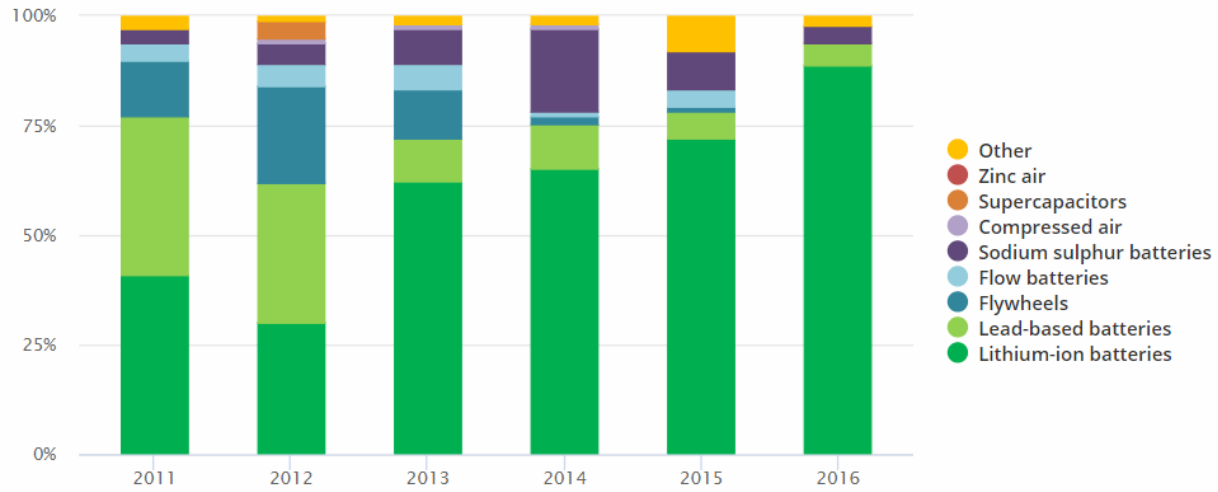

Figure IV.1: Technology mix in storage installations.

Moreover, the development and commercialization of future batteries is directly rooted in material discovery. Promising new materials with high energy density are required toward the achievement of more efficient batteries. Interestingly, the recent breakout in 2D materials with their outstanding properties strengthens the role they can play in energy storage applications.

The exfoliation of graphene [121] from its bulk counterpart, graphite, in 2004 has attracted a wide attention thanks to its unique properties [122-125] in a variety of applications such as nanoelectronic devices [126], field-effect transistors [127], solar cells [128], Li-ion batteries (LIBs) [129,130], etc. The successful manipulation of graphene has afterwards opened the way to extensive research on new 2D materials, particularly in the field of energy storage applications. Indeed, usage of graphene [131-133] and 2D-MoS_2 [134-136] as anodes in LIBs has shown high reversible lithium storage capacity and rate capability. However, the relatively weak binding and the high diffusion barriers in those 2D materials are still preventing their fruitful applications in batteries [137,138]. In this context, it was recently demonstrated that black phosphorus (BP), with its high capacity of storage of 1279 $mAh.g^{-1}$ (against 372 $mAh.g^{-1}$ and 744 $mAh.g^{-1}$ for graphite and graphene, respectively [139]) and its decent cycle of life (100 cycles) [140], may represent the next generation of anodes for LIBs. Analogically with graphite/graphene, we therefore believe that phosphorene (the 2D material of BP bulk counterpart) is expected to contribute to the development of anode materials due to its interesting structural anisotropic properties, *e.g.* puckered structure, that provides phosphorene with a relatively high carrier mobility up to 1000 $cm^2.V^{-1}.s^{-1}$ [141] although it is not as high as that of graphene; 200 000 $cm^2.V^{-1}.s^{-1}$ [146]. In terms of integration in ion-batteries, graphene is very limited to small ions due its tiny inter-sheets distance (1.86 Å) [142] as compared with that of phosphorene (3.08 Å) [143] which is capable of hosting large ions such as sodium (2.04 Å) or potassium (2.76 Å).

Therefore, it is of central importance to explore phosphorene's electrochemical properties with a variety of ion sizes. As a first attempt, a detailed study on the adsorption and diffusion behaviors of alkali and alkaline earth-metal atoms on a phosphorene monolayer is presently reported, using first-principles calculations. In order to approach those behaviors, a hypothetically assumed two-dimensional and free-standing phosphorene is considered in this thesis. Binding energies, specific capacities and diffusion barriers were calculated in the aim to elucidate the phosphorene characteristics as an anode material for battery applications.

IV.2 Computational Details

Our first-principles calculations were performed within the framework of density functional theory (DFT), implemented in the Quantum-ESPRESSO package [144]. The Perdew−Burke−Ernzerhof (PBE) functional and projector augmented wave (PAW) potentials, derived from the generalized gradient approximation (GGA) [145], were used to take into account the electron-ion interactions. Effects of van der Waals (vdW) interactions were taken into consideration using a dispersion-corrected DFT method (DFT-D2 method) [146]. The used plane wave cut-off for all calculations is of 40 Ry. All atomic positions and lattice vectors were fully optimized to obtain the relaxed configuration by means of the Broyden–Fletcher–Goldfarb–Shanno (BFGS) method. The atomic relaxation was performed with an energy convergence of 10^{-5} Ry and a force convergence of 10^{-4} Ry per Bohr. A model of 1x2 supercell of phosphorene monolayer is used and a large enough (larger than 15 Å) periodic vacuum condition is used in the perpendicular direction to the phosphorene surface in order to avoid interactions between periodic images. k-point samplings of 4×3×1 were used for the structure relaxation, while denser meshes of 16×12×1 were used to calculate the electronic properties. The diffusion behavior of the adatoms on phosphorene was simulated using the nudge elastic band (NEB) method. In the relaxation calculations, 7 images were generated between the initial and final points of the diffusion and the considered orthogonal force on each image is converged to 0.01 eV $Å^{-1}$.

IV.3 Results and Discussion

Unlike the flat structure of graphene, atoms in a single-layer of phosphorene form a hexagonal puckered structure. Our relaxed-structure calculation, using a PBE-based approximation, led to lattice constants of a = 3.29 Å, b = 4.63 Å and Δc = 2.10 Å (thickness of a single layer), in agreement with other investigations [147-149].

In order to study the adsorption and surface-diffusion behaviors of alkali atoms (Li, Na and K) and alkaline earth-metal atoms (Be, Mg and Ca) on a phosphorene surface, we have first calculated binding energies of these atoms as a function of their positions on the surface. The calculated binding energy for each site is given by [150]: $E_{\mathrm{b}} = E_{\mathrm{P-A}} - E_{\mathrm{P}} - E_{\mathrm{A}}$, where $E_{\mathrm{P\text{-}A}}$ is the total energy of the system composed of the adatom bound to phosphorene , E_{P} is the total energy

of phosphorene and E_A is the total energy of a freestanding metal atom. Binding energy calculations over various adsorption sites are summarized in Table IV.1. As can be noticed, the highest binding energies were found to be those corresponding to three different adsorption sites.

Table IV.1: Absolute binding energies $|E_b|$ at the hollow (H), top (T) and bridge (B) sites.

atoms	$\|E_b\|$ (eV)		
	H	T	B
Li	1.94	1.68	1.89
Na	1.56	1.03	1.49
K	1.14	0.55	0.94
Be	1.87	1.87	1.84
Mg	0.93	0.93	0.92
Ca	1.54	1.54	1.46

These three positions are illustrated in the scheme of Figure IV.2. As a first remark, we clearly notice that the calculated binding energy is inversely proportional to the adatom atomic radius, mainly due to the negative charge repulsion between adatoms and the phosphorene surface where the larger is the adatom radius the more is the repulsion from the surface. However, an exception for Mg is noted. This Mg exception has been reported elsewhere [151] to be due to the P-Mg interaction that reduces the polarizability of Mg and thus resulting in a weak binding energy. In addition, we also noticed that the highest binding-energy site, for all adatoms, corresponds to the hollow (H) site located above the triangle center composed of three phosphorous (P) surface atoms, in perfect accordance with the literature [152-154]. Such a behavior indeed makessense since adatoms usually prefer adsorption sites with the highest coordination number, although the H and T sites are shown to be very competitive for alkaline earth-metal atoms (Be, Mg and Ca) attraction. For the other two sites, however, a slight difference is noticed depending on the adatom nature. For alkali adatoms, the second site of preference is the bridge (B) site taking place between two P atoms, while for alkaline earth-metal adatoms it is the top (T) site, directly situated on top of a P atom. This behavior is most probably due the high electronegativity of alkaline earth-metal adatoms that help the later to be attracted only by a single P atom.

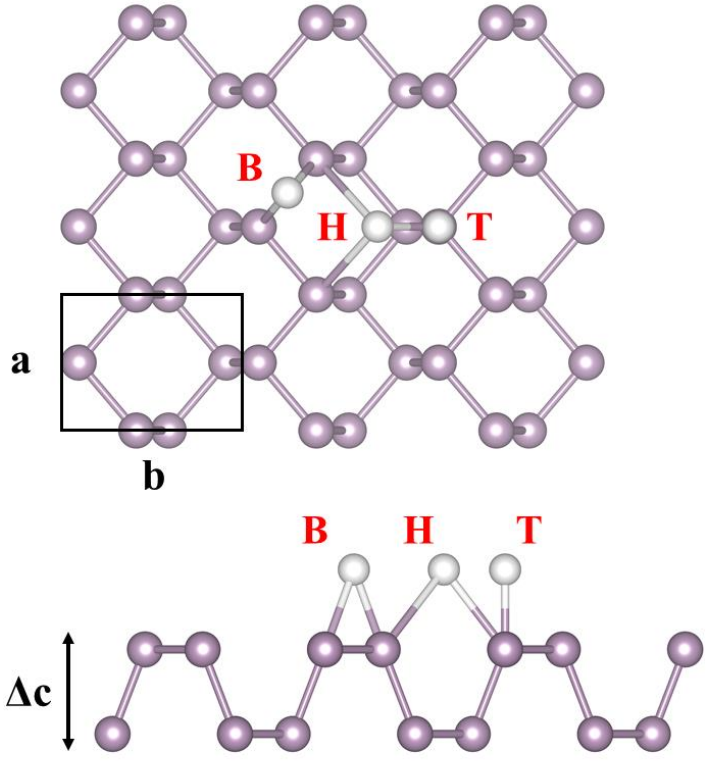

Figure IV.2: Top and side views of phosphorene with three different adsorption sites; hollow (H), top (T) and bridge (B). The purple and black spheres represent P atoms and the adsorption sites, respectively.

A comparison of phosphorene binding-energy values with those corresponding to graphene [155,156] is presented in Figure IV.3. Only phosphorene H-site values are considered. Interestingly, a clear advantage for phosphorene over graphene is demonstrated for all adatoms suggesting that, in contrast to the flat structure of graphene, the puckered structure strengthens the binding of adatoms on the phosphorene surface. The Bader charge [157] examination of the transferred electrons between the adatoms and phosphorene has been carried out showing a large charge transfer to the surface with values of 0.80, 0.86, 0.53, 0.68, 0.51 and 0.60 |e| for Li, Be, Na, Mg, K and Ca respectively. The significant amount of charge transfer from the adatoms to the surface of phosphorene explains the strong P-adatom binding presented in Figure IV.3.

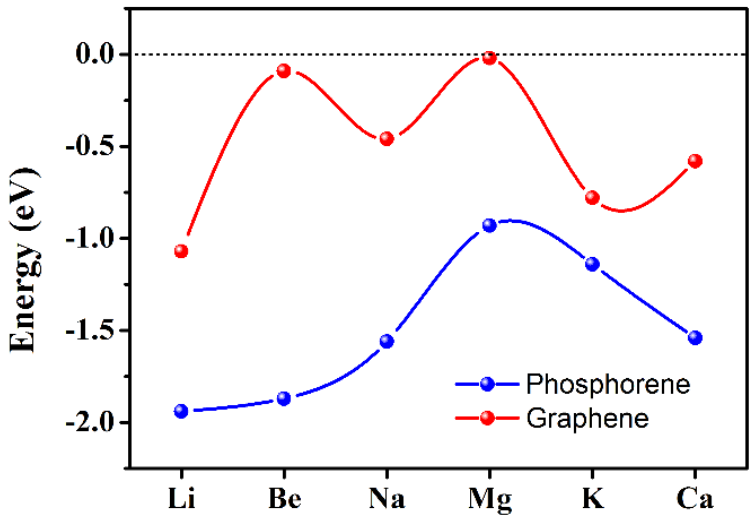

Figure IV.3: Comparison of total binding energy at the H-site for all adatoms on phosphorene (this work as blue-line) and on graphene (as red-line, Ref. [155,156]).

Alongside the adsorption properties, the performance of a battery is essentially accounted for the facile mobility of its intrinsic ions. Therefore, we simulated the diffusion of Li, Be, Na, Mg, K and Ca atoms over the surface of a phosphorene monolayer in order to examine their possible pathways and evaluate their energy barriers. Considering the puckered structure of phosphorene, two diffusion pathways are considered [153], as illustrated in Figures IV.4a-4d: the first one along the H1-T-H3 pathway (*i.e.* armchair direction) and the second one through the H1-B1-H2-B2-H3 pathway (*i.e.* zigzag direction). As expected, we found that the diffusion of all adatoms on phosphorene shows an anisotropic behavior, in agreement with the literature [153,154]. The typical barrier energy variation is exhibited in Figure IV.4e. The low diffusion-energy clearly corresponds to that along the zigzag pathway.

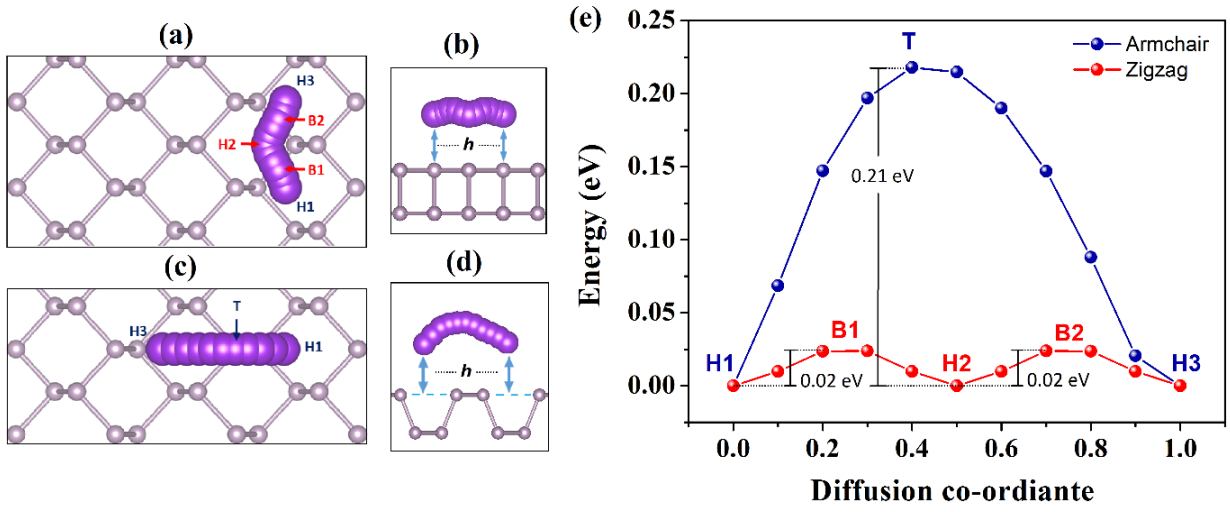

Figure IV.4: Top and side views of an adatom diffusion path along (a, b) the zigzag direction, (c, d) the armchair direction. (e) Typical barrier-energy profile of an adatom (K in this case) along armchair and zigzag directions on a phosphorene monolayer.

In Figure IV.5, we can see that the lowest barrier energies being those of alkali adatoms, especially that of K (0.02 eV). To the best of our knowledge, this is the lowest diffusion barrier among any other metal adatom on phosphorene single layer. This remarkable diffusion preference is absent in any other 2D anode material. In the case of alkaline-earth metals, however, the obtained diffusion barrier energies are quite high as compared with those of alkali adatoms. In fact, these adatoms have small atomic radii which should result in a strong attachment between the phosphorene and the adatom as represented by the vertical height (*h*) in Table IV.2.

Table IV.2: Vertical height (*h*) at the H-site and the bond lengths ($d_{P\text{-}A}$) of the nearest three P atoms to the adatom position at the H-site.

atoms	*h* (Å)	$d_{P\text{-}A}$ (Å)		
		P_1-A	P_2-A	P_3-A
Li	1.53	2.42	2.55	2.55
Na	2.34	2.89	3.01	3.01
K	2.65	3.30	3.39	3.39
Be	0.81	2.09	2.17	2.17
Mg	2.10	2.73	2.90	2.90
Ca	2.15	2.94	3.03	3.03

Indeed, we found that the diffusion of Be across phosphorene requires a diffusion barrier energy of about 0.77 eV along the armchair direction, against 0.23 eV along the zigzag direction. On the other hand, we have found that Mg diffuses more easily than Ca on phosphorene with values of 0.2 eV and 0.05 eV along armchair and zigzag directions, respectively, against 0.44 eV (armchair) and 0.07 eV (zigzag) for Ca. Although the above diffusion barriers on phosphorene are relatively high, they remain very much lower than those on other 2D anode materials such as graphene (0.32 eV for Li) [158], silicene (0.20 eV for Li) [159] and MoS_2 (0.28 eV for Na) [160].

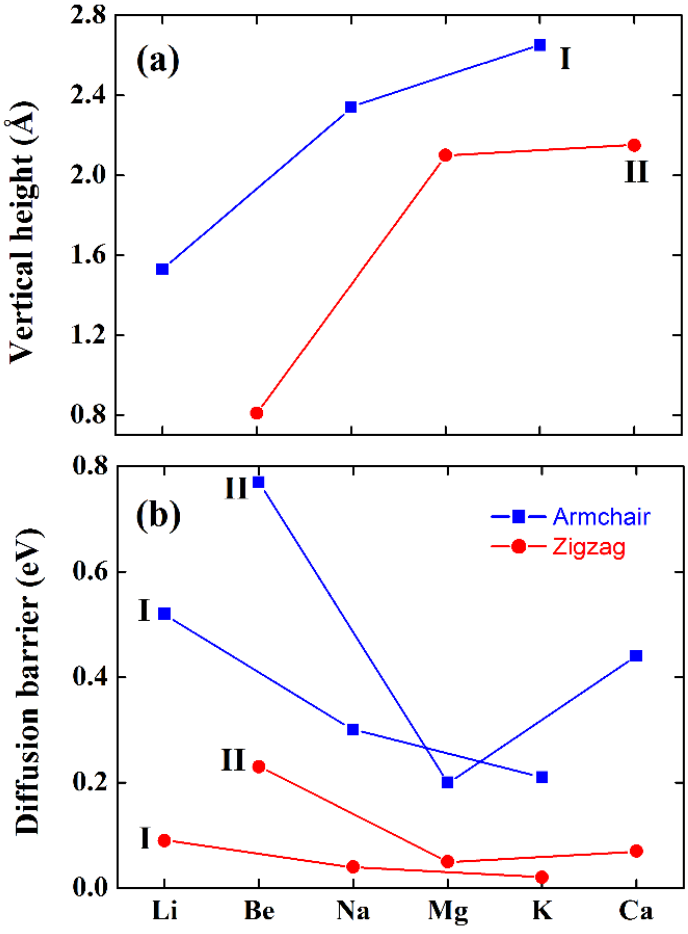

Figure IV.5: (a) Vertical height (h) of adatoms with respect to the surface of phosphorene at the H-site, and (b) diffusion barrier energies of metal adatoms. Group I and II denote alkali and alkaline-earth metals, respectively.

To gain additional insight on the surface capacity of phosphorene, we have checked the adsorption of adatoms on a phosphorene monolayer with different concentrations: 1, 2 and 4 adatoms. For all six elements, it was found that in the case of a 1x2 supercell of phosphorene (eight phosphorus atoms), the adsorption of more than four adatoms yields to a structural distortion of the phosphorene lattice as presented in Figure IV.6. Therefore, a 1x2 supercell of phosphorene is considered as full with four adsorbed atoms giving rise to pseudo- compound with a formula of $A_{0.5}P$ (A = Li, Be, Na, Mg, K or Ca).

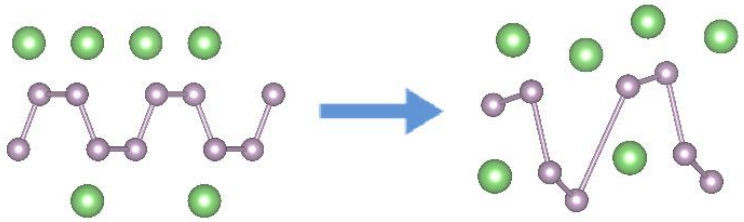

Figure IV.6: The structural distortion of phosphorene lattice with an adsorption of six Li atoms.

For practical usage, anode materials should have a high specific capacity which is calculated based on the highest number of ions that can be hosted in a material. Accordingly, the computed specific capacities are evaluated based on the $A_{0.5}P$ composition for each element and are presented in Table IV.3. As compared to other 2D anode materials, such as Ti_3C_2 monolayer (320 mAh/g [161] for LIBs) or MoS_2 monolayer (146 mAh/g [162] for SIBs), phosphorene provides a larger capacity of storage with values of 389 mAh/g for Li and 315 mAh/g for Na. However, it is noted from values in Table IV.3 that graphene shows higher specific capacities as compared with phosphorene, which could be attributed to the large mechanical strength of graphene [124] preventing it from distortion at the adsorption of adatoms, unlike phosphorene. Finally, we clearly notice that phosphorene has a better potential than graphene in terms of binding energies and diffusion, but shows a low performance in terms of capacity of storage. With this in mind, we believe that a phosphorene-graphene hybrid system may act as a remarkable ion-anode. Indeed, such an attempt has been successfully tested by Jie Sun et al. [143] where a phosphorene–graphene hybrid material was experimentally fabricated arising in a high-capacity anode for sodium-ion batteries.

Table IV.3: Calculated specific capacities (mAh/g) of phosphorene, as compared with those of graphene and Ti_3C_2 as extracted from the literature.

atoms	Li	Be	Na	Mg	K	Ca
Phosphorene	389.02	377.67	315.52	310.71	265.22	262.68
Graphene	744 [139]	-	300 [139]	-	-	297 [165]
Ti_3C_2	320 [161]	-	351 [166]	-	191 [166]	319 [166]

In addition, the examination of the density of states (DOS) of full phosphorene in the case of all six elements indicates that the semiconducting behavior observed in the pristine form of phosphorene is switched into a metallic one at the adsorption of four adatoms. This observation was reported in other studies on phosphorene [154] and also for other 2D materials such as germanene and stanene [163]. Figure IV.7a shows that phosphorene monolayer exhibits a semiconducting behavior with a direct bandgap of about 2.03 eV (HSE06 calculations) at Γ point symmetry, identical to the experimental bandgap [164], where the valence and conduction bands are mainly composed of the 3p states. By gradually increasing the concentration, and before reaching the fully adsorbed configuration of phosphorene, the bandgap of the P-adatom system gradually decreases in an inversely proportional manner to the atomic size of the adatoms where the P-K structure have the lowest bandgap followed by structures such as P-Na, P-Mg or P-Ca. This observation could give a clear insight on the diffusion behaviors of the adatoms where K, having the largest atomic size, diffuses more easily on the phosphorene surface. In Figure IV.7b, which corresponds to the fully lithiated phosphorene, a metallic transition is observed as the Fermi level is occupied by electronic states. This finding is also observed in the case of all other elements. This observation indicates that the adatoms mainly contribute into the donation of electrons to the band conduction of phosphorene until changing its electronic structure after full adsorption, as presented in Figure IV.7 in the case of Li.

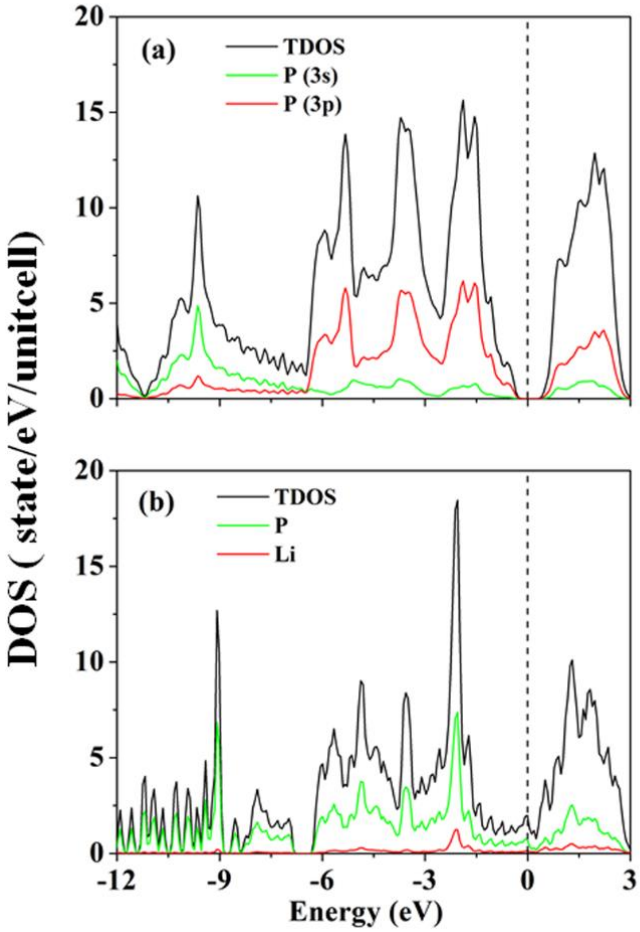

Figure IV.7: Density of states of (a) pristine phosphorene monolayer and (b) fully lithiated phosphorene corresponding to the adsorption of four Li atoms.

IV.4 Conclusion

In summary, we have investigated in the present study, using first-principles calculations, the adsorption and surface-diffusion behaviors of alkali atoms (Li, Na and K) and alkaline earth-metal atoms (Be, Mg and Ca) on a phosphorene surface in order to evaluate its performance as an anode material for rechargeable batteries. Our results show that all the elements can be stably adsorbed on phosphorene and tend to prefer to be adsorbed on the H-site.

The binding energy of alkali atoms show that the atomic size highly influences the interaction between the adatom and the substrate while the interaction of alkaline-earth metals and phosphorene is difficult to be predicted. In comparison with graphene, our results show that phosphorene enhances the binding energies of the adsorbed atoms. Moreover, a semiconductor-to-metal transition is observed upon the complete adsorption of more than four atoms, which is vital for electrode uses. The diffusion analysis shows that the migration of the adatoms on phosphorene is highly influenced by its structural anisotropy giving a privilege to the diffusion along the zigzag direction over the armchair direction. Owing to its large atomic size, we found that the diffusion barrier of K along the zigzag direction is extremely low (0.02 eV) while an atomic size of the order of Be atom finds it almost prohibited to diffuse along the armchair direction (0.77 eV).

Our findings show that phosphorene is clearly exhibiting a higher performance than other 2D materials such as graphene in terms of adsorption and diffusion, but a less capacity of storage than the latter. Nevertheless, we believe that a phosphorene-graphene hybrid system may constitute promising high-capacity ion-anode.

CHAPTER V: COVERAGE DEPENDENT ADSORPTION OF SMALL GAS MOLECULES ON PHOSPHORENE FOR SENSING APPLICATIONS

In this Chapter, we performed a detailed computational study to explore the adsorption characteristics of NH_3, NO, NO_2, CO and CO_2 molecules on a black phosphorene monolayer, at several coverages. The van der Waals (vdW) interactions were taken into account within the optB88-vdW functional. In addition, a comparison with the newly introduced Strongly-Constrained and Appropriately-Normed (SCAN) meta-Generalized Gradient Approximation (meta-GGA) is used.

Our calculations show that all molecules adsorb on the phosphorene surface with different favorite adsorption sites, depending on the molecule geometry and orientation. Alongside with the adsorption energies, other properties of the molecules' adsorption are presented including the adsorption heights and charge transfers. At high coverages, the calculated adsorption energies per molecule show that the molecule-molecule interactions for the SCAN is stronger than that for the optB88-vdW functional pointing to new insights for the role of meta-GGA in the inter-molecule interactions.

V.1 Motivation

The air pollution caused by exhaust gases from automobiles has become a critical issue. In some regions, fossil fuel combustion is a problem as well. The principal gases that cause air pollution from automobiles are nitrogen oxides, NO_x (NO and NO_2), and carbon monoxide (CO). Because NO_x gases with sulfur oxides (SO_x) emitted from coal fired plants cause acid rain and global warming and produce ozone (O_3) that leads to serious metropolitan smog from photochemical reaction, they must be detected and reduced [167,168].

A substance in the air that can cause harm to humans and to the environment is known as an air pollutant. Pollutants can be in the form of solid particles, liquid droplets, or gases. They may be natural or man-made [169]. Pollutants can be classified as primary or secondary. Usually, primary pollutants are directly emitted from a process, such as ashes from a volcanic eruption, the NO_x and CO gases from a motor vehicle exhaust or SO_x released from factories. Secondary pollutants are not emitted directly. Rather, they form in the air when primary pollutants react or interact. An important example of a secondary pollutant is ground level ozone - one of the many secondary pollutants that make up photochemical smog. Some pollutants may be both primary and secondary: that is, they are both emitted directly and formed from other primary pollutants. Causes and effects of air pollution are shown in Figure V.1.

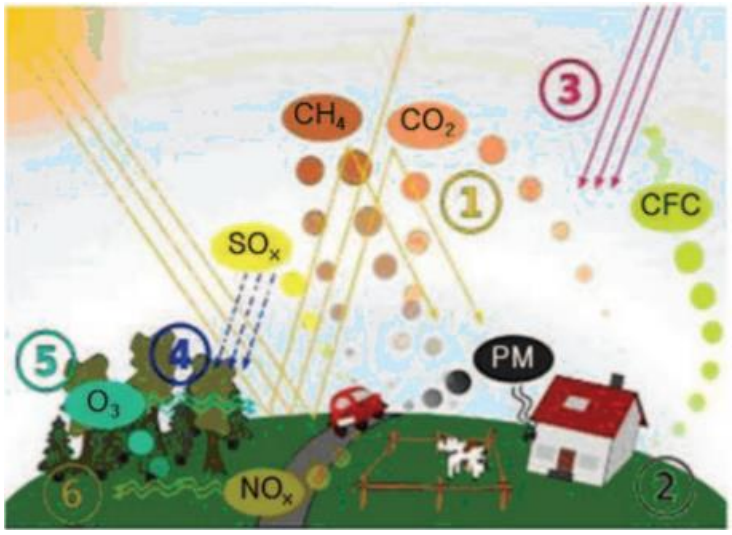

Figure V.1: Schematic drawing, causes and effects of air pollution: (1) greenhouse effect, (2) particulate contamination, (3) increased UV radiation, (4) acid rain, (5) increased ground level ozone concentration, (6) increased levels of nitrogen oxides.

In addition, as greater amounts of oil organic compounds are currently being produced by applied construction materials and households, the number of people who develop various symptoms after moving into a new apartment (e.g., tickle, headache, skin trouble) is increasing [170]. The principal gases that cause this phenomenon (called "sick-building syndrome") are formaldehyde (HCHO) and volatile organic compounds (VOCs) [171]. Especially, formaldehyde is the most dangerous among indoor pollutants as it could harm all kinds of organisms. Considering these, the allowed concentration of formaldehyde in the Netherlands and Germany is only 0.1 ppm [172]. Therefore, gas sensors with excellent reactivity and stability are needed.

The first decade of the 21st century has been labeled by some as the "Sensor Decade." A sensor is a device that converts a physical phenomenon into an electrical signal. As such, sensors represent part of the interface between the physical world and the world of electrical devices, such as computers. In recent years, sensors have received people's attention as one of the important devices in electronic systems and enormous capability for information processing has been developed within the electronics industry. Of all sensors, gas sensors and light sensors have been most actively studied [173]. The final goal of gas sensor development is to establish the array technology of multifunctional gas sensors that can monitor air pollution with low cost, and is to fabricate the electronic nose using this technology.

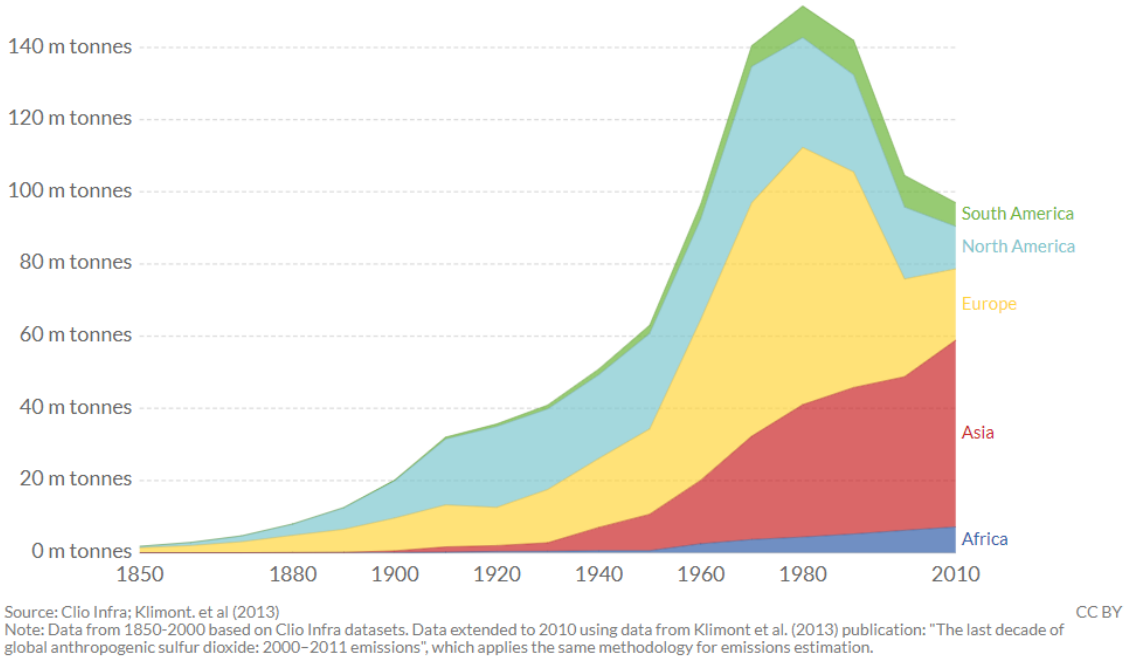

Figure V.2: Annual sulphur dioxide (SO_2) emissions by world region in million tones.

Gas sensors can be classified into semiconductor-type, solid electrolyte-type, electrochemical type and catalytic combustion-type. Among these, the semiconductor-type gas sensor, the best-known one, is operated by changing its conductivity when it is exposed to gas. The semiconductor-type gas sensor has the advantages of rapid reactivity, efficiency, and gas selectivity when suitable additives are applied to it [174,175]. The gas-sensing materials for semiconductor type are SnO_2, WO_3, In_2O_3, perovskite-structure oxides, etc. Sensors made of inorganic materials are the most commonly used, especially ceramics. One reason is that many sensors are used in very severe conditions such as high temperature, reactive or corrosive atmosphere and high humidity, and ceramics are most reliable materials in these conditions.

V.1.1 2D Materials as Gas Sensors

Since the millennium untill now, a vast number of materials have demonstrated gas sensing properties including low dimensional carbon-based materials as carbon nanotubes, graphene and its oxide. Recently, other 2D materials featuring a bandgap caught the attention as a promising candidate material for sensing devices. One example of such materials family is the transition metal di/tri-chalcogenides family (TMDs). For example, molybdenum disulfide has shown sensitivity to different gas molecules interacting on its monolayer showing sensitivity towards carbon monoxide/dioxide, ammonia, nitrogen monoxide/dioxide, methane, water molecules, nitrogen, oxygen and sulfur dioxide. Similarly, Dirac materials such as silicene have also demonstrated promising activity in the material's sensing behavior, showing sensitivity against a wide range of gases such as nitrogen monoxide/dioxide, sulfur dioxide, oxygen and ammonia, as well as formaldehyde. In addition, the newly discovered 2D black phosphorene is expected to hold promising sensing capabilities due to its very large surface-to-volume ratio [176].

In fact, several studies have already been devoted to the study and understanding of this newly discovered 2D material and its integration into different applications such as transistors [177], batteries [178] and thin-film solar cells [179]. However, only a few have explored the potential of phosphorene as a gas sensing material [180-185]. A reason why we believe that the effect of the adsorption of small gas molecules on phosphorene is still not fully explored and must be investigated in depth using highly accurate Density Functional Theory (DFT) methods. Actually, a recent breakthrough in DFT has been recently introduced in the form of the strongly-constrained and appropriately-normed (SCAN) [186,187] meta-generalized gradient

approximation (meta-GGA) which can predict accurate geometries and energies of diversely-bonded molecules and materials (including covalent, metallic, ionic, hydrogen, and van der Waals bonds) significantly improving over its predecessors at comparable efficiency such as the GGA which dominates materials computation. We believe that this newly introduced approximation can help to accurately predict the detection process of toxic gas molecules on phosphorene.

In this Chapter, we will use both GGA and meta-GGA based functionals in order to perform a comprehensive computational study of the adsorption of small gas molecules (NH_3, NO, NO_2, CO and CO_2) on a phosphorene monolayer, at both low and high coverage rates. Our calculations show that, at high coverage, the recently introduced SCAN+rVV10 functional predicts, for some cases, geometries and binding energies of the adsorbed molecules different than the widely used optB88-vdW functional.

V.2 Computational Details

Our calculations were performed within the framework of Density Functional Theory (DFT) as implemented in the Vienna *ab initio* simulation (VASP) package [188-190]. The generalized gradient approximation (GGA) in the form of the Perdew−Burke−Ernzerhof (PBE) functional and the projector augmented wave (PAW) potentials [191,192] were considered alongside with the effect of van der Waals (vdW) interactions in the form of the optB88-vdW correction [193]. In addition, the recently developed SCAN meta-GGA functional [186,187] as combined with the long-range rVV10 [194], a revised van der Waals correction from the VV10 [195], is used for comparison with the optB88-vdW functional. The plane wave cut-off for all calculations was set to 400 eV and the atomic relaxation was performed with a force criterion of 0.01 eV/Å. A 3×3 supercell (36 Phosphorus atoms) structure of phosphorene with a lateral periodic boundary condition is used alongside with a vacuum of 15 Å in the perpendicular direction to the surface in order to avoid interactions between periodic images. In the relaxation calculations of the adsorbed molecules on phosphorene, all structures were allowed to relax along all three *x, y* and *z* directions in order to get the lowest energy relaxed configurations. k-point samplings of 4×3×1 was used for the structure relaxation, while denser meshes of 12×9×1 was used to calculate the electronic properties.

V.3 Results and Discussion

As mentioned before, one of the objectives of our study is to test the efficiency of the newly introduced SCAN+rVV10 functional in predicting the adsorption characteristics of NH_3, NO, NO_2, CO and CO_2 gas molecules on phosphorene as compared to the optB88-vdW functional. But before that, we first start by evaluating the performance of the SCAN+rVV10 functional in the calculation of the structural parameters of black phosphorus and its two-dimensional derivatives.

V.3.1 Structural Properties of Black Phosphorus with SCAN+rVV10

Black Phosphorus (BP) is a layered material in which atomic layers are bound by van der Waals (vdW) interactions and which exhibits an AB stacking. In each single layer of BP, phosphorus atoms are arranged in a puckered and hexagonal structure as shown in Figure V.3.

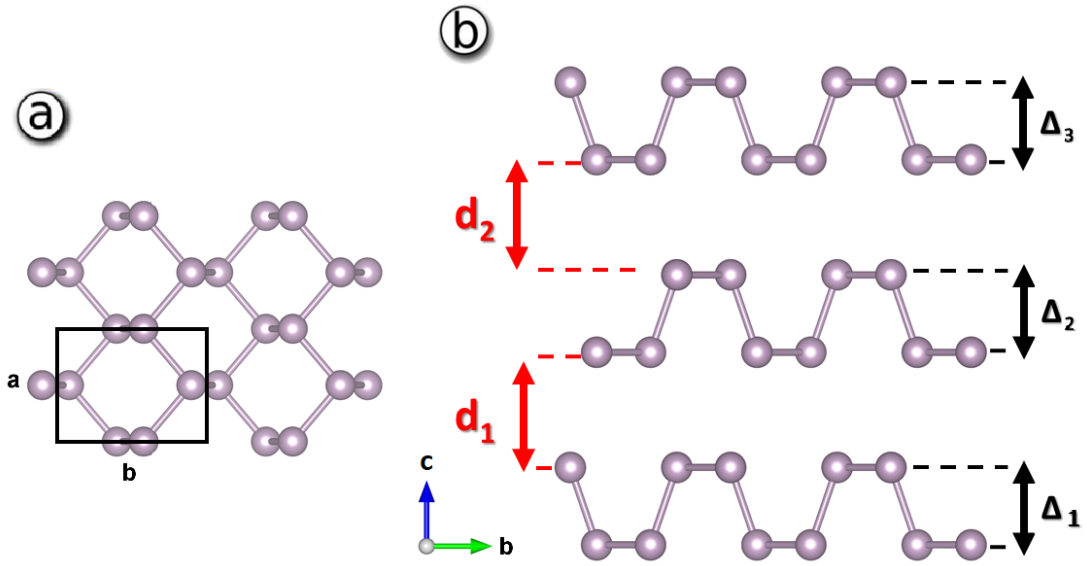

Figure V.3: (a) Top view of monolayer phosphorene and (b) side view of trilayer phosphorene. Δ and *d* denote the puckering and interlayer distances, respectively.

We first start by calculating the lattice constants for bulk BP with PBE, optB88-vdW and SCAN+rVV10 functionals. The resulting lattice constants are shown in Figure V.4. The calculated *c* lattice constant for bulk BP is: 11.28, 10.74 and 10.66 Å for PBE, optB88-vdW and SCAN+rVV10 respectively (see Table V.1). Overall, all calculated lattice parameters for bulk BP are in good agreement with the experiment (a = 3.31 Å, b = 4.37 Å and c = 10.48 Å) [196,197].

However, it can be seen that SCAN+rVV10 is the functional that presents the best agreement with the experimental values, with *b* and *c* lattice parameters overestimated by only 1.71% and 1.83%, respectively, while both SCAN+rVV10 and PBE functionals predict the *a* lattice constant with a better accuracy, resulting in an underestimation of only 0.6% and 0.3% from the experiment, respectively.

Table V.1: Lattice constants for monolayer (ML), bilayer (BL), trilayer (TL) and bulk BP. All reported values are in angstrom (Å).

	ML	BL	TL	Bulk
PBE	*a* = 3.29 *b* = 4.62	*a* = 3.30 *b* = 4.59	*a* = 3.30 *b* = 4.58	*a* = 3.30 *b* = 4.55 *c* = 11.28
vdw-optB88	*a* = 3.32 *b* = 4.57	*a* = 3.33 *b* = 4.52	*a* = 3.33 *b* = 4.50	*a* = 3.34 *b* = 4.46 *c* = 10.74
SCAN+rVV10	*a* = 3.26 *b* = 4.58	*a* = 3.28 *b* = 4.50	*a* = 3.27 *b* = 4.50	*a* = 3.29 *b* = 4.45 *c* = 10.66
Experimental [196]	—	—	—	*a* = 3.31 *b* = 4.37 *c* = 10.48

Based on this, the initial structure of phosphorene monolayer (ML), bilayer (BL) and trilayer (TL) were obtained from the relaxed structure of bulk BP with each different functional. The calculated lattice constants for these structures are summarized in Figure V.4 showing that by adding more layers, from ML to TL, the *a* lattice constant increases for all three functionals except for SCAN+rVV10, where the *a* lattice constant value in TL drops by 0.005 Å from that in BL, while the *b* lattice constant continuously decreases from ML to TL for the cases of all three functionals. This tendency can be explained by the fact that, using all three functionals, both lattice parameters tend to converge towards those of the bulk BP parameters.

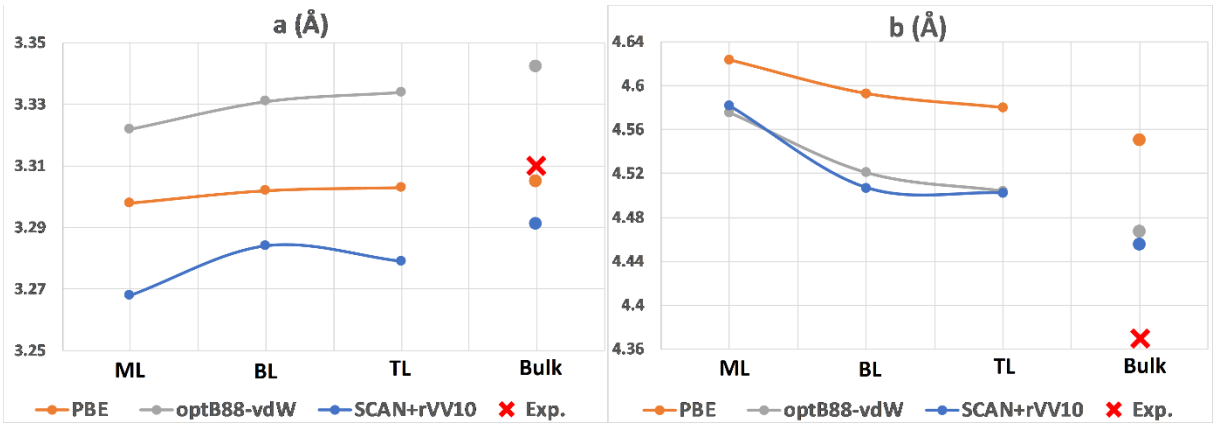

Figure V.4: Lattice constant parameters of monolayer (ML), bilayer (BL), trilayer (TL) and bulk black Phosphorus (BP) obtained with PBE, optB88-vdW and SCAN+rVV10 functionals. Red crosses represent experimental values for bulk BP from Ref. [196].

V.3.2 Adsorption of NH_3, NO, NO_2, CO and CO_2 on a phosphorene monolayer at low coverage

In order to study the adsorption behaviors of NH_3, NO, NO_2, CO and CO_2 gas molecules on phosphorene, we first start by identifying the adsorption sites with the highest binding energies on the phosphorene surface. These latter were found to be corresponding to four different adsorption sites as illustrated in the scheme of Figure V.5. The calculated binding energy for each adsorption site is calculated as: $E_b = E_P + E_M - E_{PM}$, where E_P is the total energy of phosphorene, E_M is the total energy of a freestanding molecule and E_{PM} is the total energy of the system composed of the adsorbed molecule bound to phosphorene. Based on this definition, a positive value of E_b refers to a stable structure and a higher value of E_b indicates a strong interaction between the molecule and the phosphorene surface. The calculated binding energies (E_b) in addition to the shortest height (h) from the surface to the molecule and the charge transfer (C) from the surface to the molecule at the energy-preferable sites are summarized in Table V.2. Moreover, in what follows we will only consider the optB88-vdW and SCAN+rVV10 functionals as the PBE functional does not take into consideration the van der Waals interactions which are crucial to treat the interactions between the adsorbed molecules and the phosphorene surface.

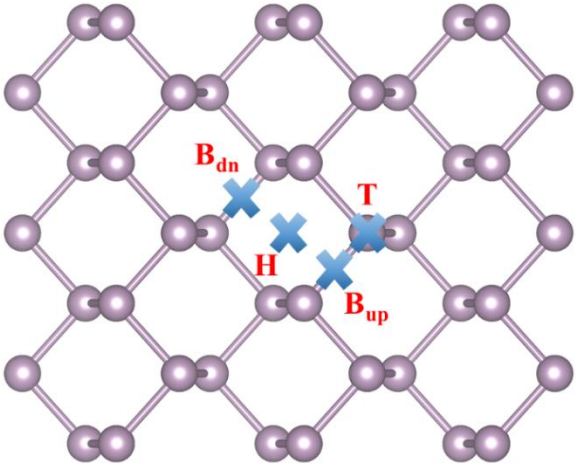

Figure V.5: Top view of phosphorene with four different adsorption sites: hollow (H), top (T), bridge up (Bup) and bridge down (Bdn). The purple spheres and the cross marks represent P atoms and the adsorption sites, respectively.

From the results presented in Table V.2, we first notice that both optB88-vdW and SCAN+rVV10 functionals predict the same energy-preferable adsorption sites for each molecule. In fact, it can also be observed from Figures V.6a-6e and Figures V.7a-7e that the functional of choice, optB88-vdW or SCAN+rVV10, does not make a difference in terms of the final relaxed configurations of the adsorption process at low coverage as both functionals predict the exact same geometries and orientations for each adsorbed molecule. However, not all molecules agree to share the same preferable adsorption site which is different from one molecule to another depending on its adsorbed geometry and orientation on phosphorene. Those relaxed structures are illustrated in Figures V.6a-6e and Figures V.7a-7e as calculated with optB88-vdW and SCAN+rVV10, respectively. On a different note, it has been reported that most of the adsorbed metals on a phosphorene surface prefer to adsorb on the H site [198]. Such finding makes sense since adatoms usually favor adsorption sites with the highest coordination number. In fact, the same observation can be noticed for the adsorption of NH_3, NO, NO_2, CO and CO_2 molecules on phosphorene, where atoms with the highest electronegativity from each molecule tend to adsorb on the H sites and thus forcing their neighboring atom(s) from the same molecule to adsorb on a different site. This can be clearly seen in the case of NH_3, NO, NO_2 and CO_2 molecules where the N atom in NH_3 and the O atoms in NO, NO_2 and CO_2 prefer to adsorb on the H sites and therefore resulting in the molecule center of mass to be adsorbed on a different adsorption site. The only exception for this tendency is the CO molecule where both C and O atoms prefer to share the H site.

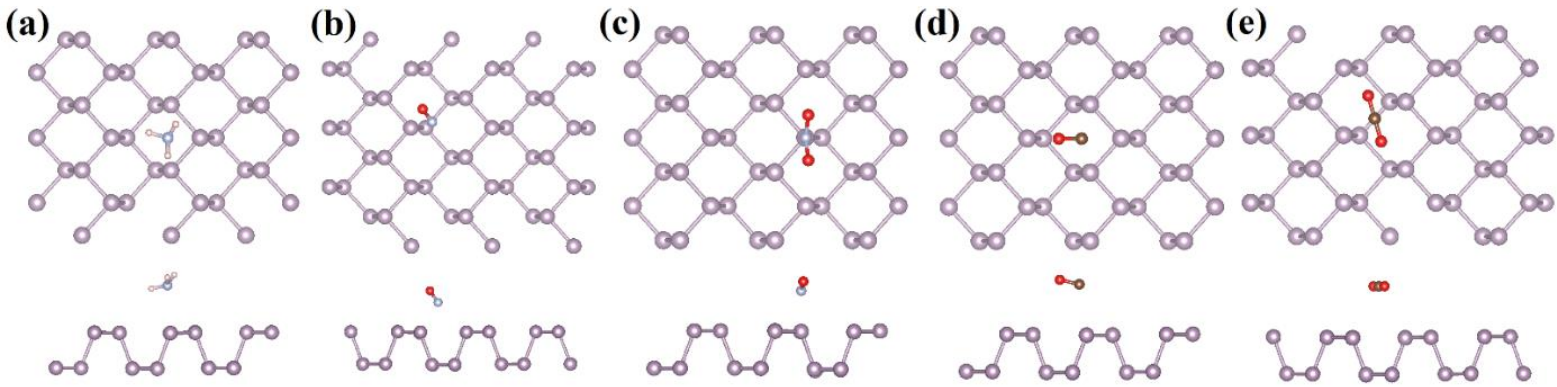

Figure V.6: Top and side views of the relaxed structures of phosphorene with the adsorbed gases (a) NH_3, (b) NO, (c) NO_2, (d) CO and (e) CO_2 as obtained with optB88-vdW functional. Purple, while gray, cyan, red, and brown spheres represent P, N, H, O, and C atoms, respectively.

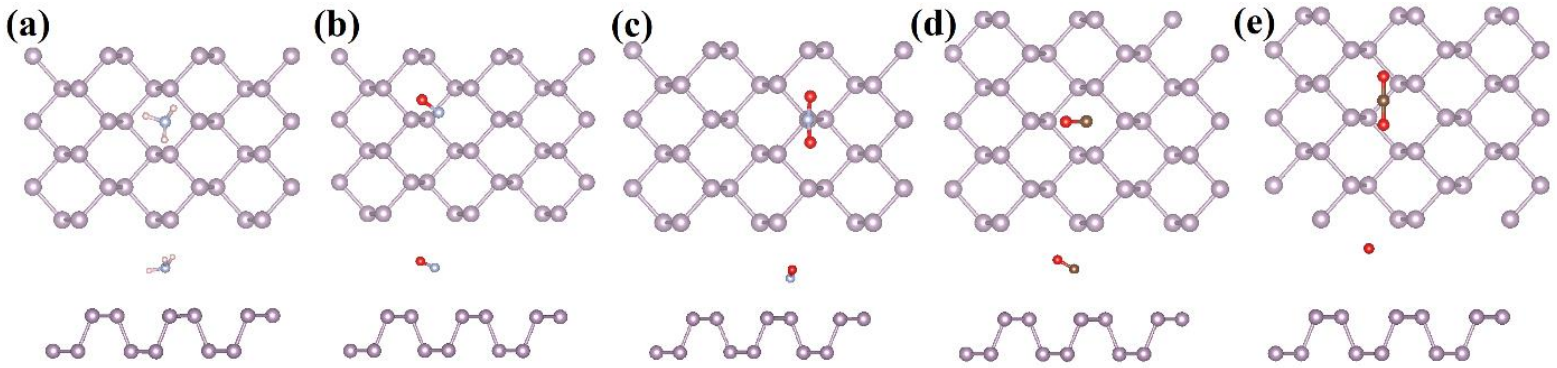

Figure V.7: Top and side views of the relaxed structures of phosphorene with the adsorbed gases (a) NH_3, (b) NO, (c) NO_2, (d) CO and (e) CO_2 as obtained with SCAN+rVV10 functional. Purple, while gray, cyan, red, and brown spheres represent P, N, H, O, and C atoms, respectively.

To further investigate the adsorption strength of these molecules on the phosphorene surface, we have calculated their binding energies (E_b) and adsorption heights (h) to the surface. In the case of NH_3 and CO molecules, both optB88-vdW and SCAN+rVV10 functionals give similar binding energies (in bold from Table V.2). For NO and CO_2 molecules, optB88-vdW seems to predict a higher E_b than SCAN+rVV10 while the opposite is true for NO_2 molecule. In addition, it can also be noted that SCAN+rVV10 functional always gives a higher h value than optB88-vdW

for all molecules except for NH_3 molecule where both functionals predict the same *h* value. Alongside the adsorption energies and height distances, we have carried out a Bader charge analysis [199] in order to calculate the charge transfer (*C*) from the surface to the molecule upon the adsorption. A positive charge transfer value denotes electron transfer from the molecule to the surface while a negative value represents the opposite. The obtained results presented in Table V.2 show that most gas molecules exhibit a small charge transfer to or from the phosphorene surface except for NO and NO_2 molecules. For these two molecules, both optB88-vdW and SCAN+rVV10 show that there is a strong correlation between the binding energy and the charge transfer value. For example, the adsorption of NO_2 molecule induces the highest binding and charge transfer, with E_b (0.52 eV) and *C* (-0.37 e) using optB88-vdW, and E_b (0.57 eV) and *C* (-0.34 e) using SCAN+rVV10. On the other hand, the calculated *C* value for NO molecule drops from -0.16 e with optB88-vdW to -0.06 e with SCAN+rVV10. This difference is due to the predicted adsorption height which plays an important role in determining the *C* value. The lowest the height, the highest the charge transfer value.

Table V.2: Energy-preferable adsorption sites, binding energies (E_b), height distances (*h*) and charge transfer from the surface to the molecule (*C*) at the most preferable site.

	optB88-vdW				SCAN+rVV10			
	site	E_b (eV)	*h* (Å)	*C* (e^-)	site	E_b (eV)	*h* (Å)	*C* (e^-)
NH_3	H	0.26	2.61	+0.02	H	0.26	2.61	-0.02
NO	B_{dn}	0.28	2.38	-0.16	B_{dn}	0.23	2.99	-0.06
NO_2	T	0.52	2.28	-0.37	T	0.57	2.46	-0.34
CO	H	0.18	2.89	-0.03	H	0.18	2.99	-0.03
CO_2	B_{dn}	0.24	2.96	-0.03	B_{dn}	0.18	3.72	-0.03

V.3.3 Adsorption of NH_3, NO, NO_2, CO and CO_2 on a phosphorene monolayer at high coverage

To gain additional insight on the ability of phosphorene to host the NH_3, NO, NO_2, CO and CO_2 molecules, we have determined the adsorption behaviors of these molecules at higher coverage rates by gradually filling the available energy-preferable adsorption sites for each molecule on the phosphorene surface. For example, the adsorption of three NH_3 molecules on the H-sites of the phosphorene surface refers to a 16.7% coverage while the adsorption of nine and

eighteen NH_3 molecules refer to a 50% and 100% coverage, respectively. Therefore, in this case, a phosphorene monolayer is considered as full when the NH_3 molecules fill in all of the 18 available H-sites in the 3x3 phosphorene supercell. A different configuration is considered for each molecule depending on the number of the available adsorption sites.

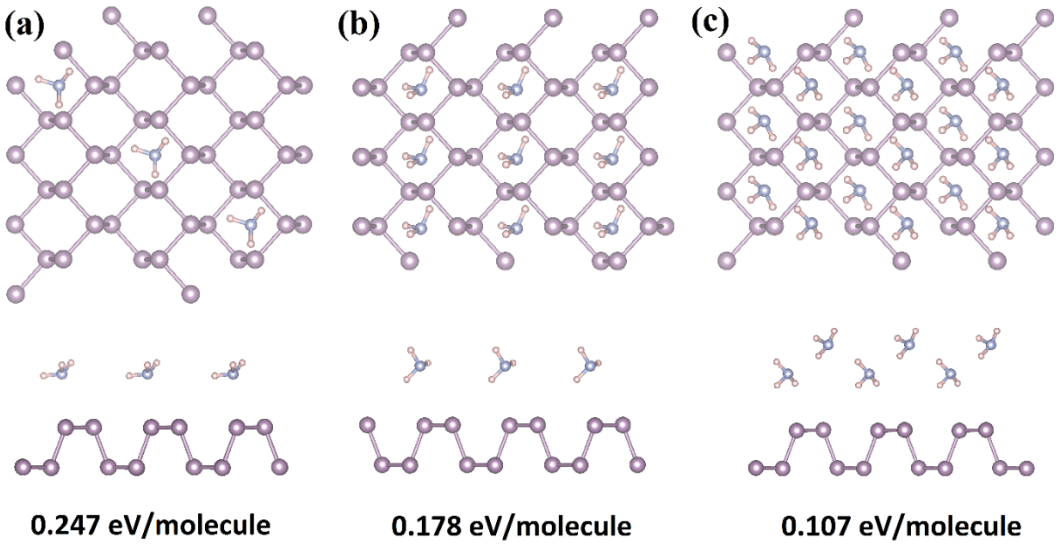

Figure V.8: Optimized configurations of the adsorption of NH_3 on phosphorene at high coverage with optB88-vdW. (a) $3NH_3$ (16.7%), (b) $9NH_3$ (50%) and $18NH_3$ (100%).

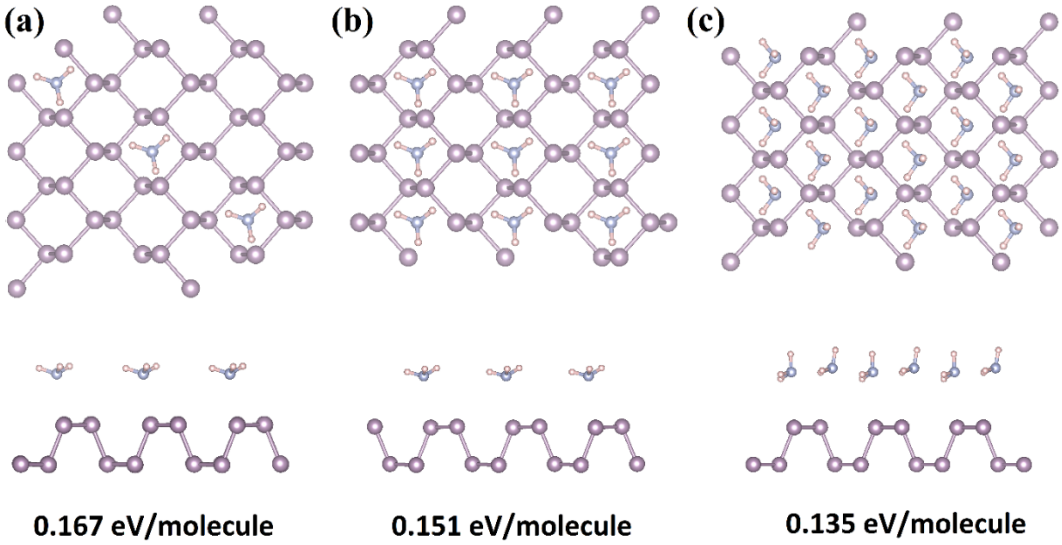

Figure V.9: Optimized configurations of the adsorption of NH_3 on phosphorene at high coverage with SCAN+rVV10. (a) $3NH_3$ (16.7%), (b) $9NH_3$ (50%) and $18NH_3$ (100%).

Figure V.8 and Figure V.9 illustrate the optimized configurations of the adsorption of NH_3 on a phosphorene monolayer as a function of the coverage rate, using both optB88vdW and SCAN-rVV10 functionals, respectively. We note that at the lower coverage rate of 16.7%, both optB88-vdW (Figure V.8a) and SCAN+rVV10 (Figure V.9a) functionals predict practically the same optimized configuration for the NH_3 molecule. As the coverage increases, the optimized configurations tend to differ for different functionals. For optB88-vdW, Figure V.8c shows that at a full coverage rate of 100%, the adsorbed NH_3 molecules tend to induce repulsive interactions between the molecules, thus forming a buckled configuration on top of the phosphorene surface. On the other hand, Figure V.9c shows that the SCAN+rVV10 functional predicts an almost flat configuration of the full coverage of NH_3 molecules on top of the phosphorene surface, thus suggesting that the adsorption behavior of the NH_3 molecules differs qualitatively when using SCAN+rVV10 and optB88-vdW, at full coverage. These findings were confirmed by calculating the binding energies (E_b) as a function of the adsorption coverage of the NH_3 molecules with both optB88-vdW and SCAN+rVV10 functionals as represented in Figure V.11, where SCAN+rVV10 seems to predict a higher binding energy (E_b) than optB88-vdW, at full coverage (100%), which can be explained by the fact that the SCAN+rVV10 functional can probably better predict the long-range molecule-molecule interactions than the optB88-vdW functional. Additionally, we have checked the behavior of the NH_3 molecules in the gas phase. Figures V.10a-10b show that, using both functionals, the NH_3 molecules prefer to form a buckled structure in the absence of a substrate proving the vital role of this latter in the adsorption configurations of NH_3 on phosphorene. Interestingly, we found that both optB88-vdW and SCAN+rVV10 functionals predict almost the same optimized configurations for NO_2, CO and CO_2 molecules at both low and high coverage rates except for NO molecules where these tend to change their favorable adsorption site at a higher coverage rate of 100%, from the H-sites to the T-sites. This behavior is only observed in the case of the optB88-vdW functional.

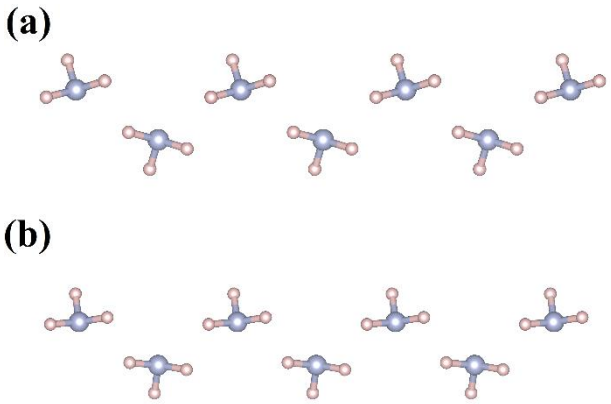

Figure V.10: Relaxed NH_3 molecules in the gas phase with (a) optB88-vdW and (b) SCAN+rVV10.

To determine which functional better predicts the adsorption behavior of our considered molecules, we have plotted in Figure V.11 the calculated E_b per molecule for each molecule as a function of their coverage rates. As a first remark, one can notice that, for both functionals, E_b per molecule decreases as the coverage increases due to the repulsive interactions between the neighboring molecules. This tendency can be observed for all molecules. We can also notice that, except for NO_2 and the full coverage for NH_3 molecules, optB88-vdW functional predicts a higher binding energy (E_b) per molecule than SCAN+rVV10. In addition, we can see that for NH_3, NO and CO_2 molecules, SCAN+rVV10 predicts the smallest difference in value of E_b as a function of the coverage rate than optB88-vdW while both functionals predict practically the same difference in the case of the CO molecules. These findings show that the molecule-molecule interaction within SCAN+rVV10 is stronger in comparison with the optB88-vdW functional and thus proving new insights for the role of the meta-GGA approximations in predicting the inter-molecular interactions that are of vital importance in describing the sensing of small toxic gas molecules such as NH_3, NO, NO_2, CO and CO_2 molecules.

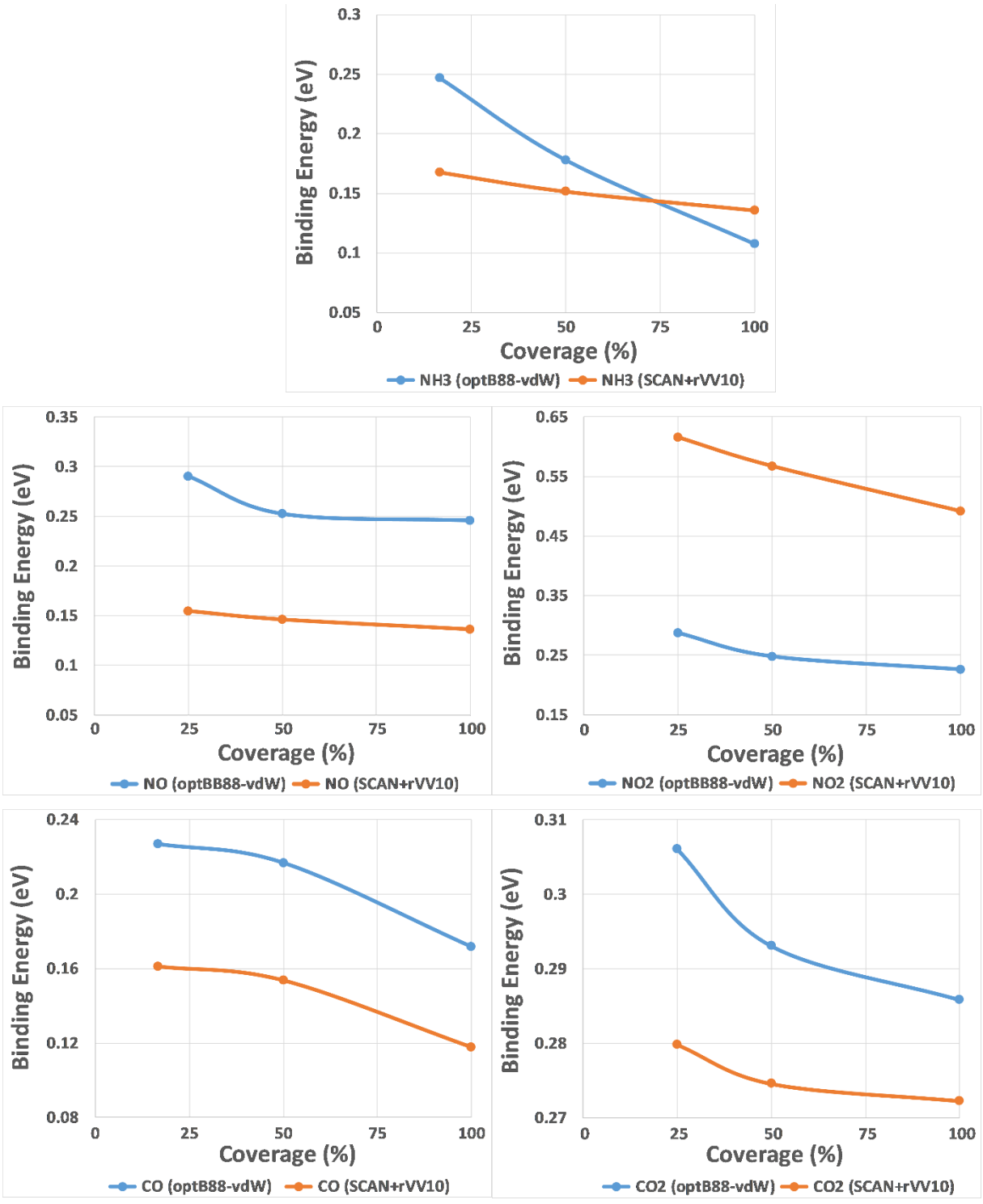

Figure V.11: Calculated binding energy per molecule as a function of the adsorption coverage for NH_3, NO, NO_2, CO and CO_2 molecules, respectively. All connecting lines are to guide the eye.

V.4 Conclusion

In summary, we have studied in the present Chapter the adsorption behaviors of NH_3, NO, NO_2, CO and CO_2 molecules on a phosphorene surface by using first-principles calculations. From our results, SCAN+rVV10 is found to give a better agreement with the experimental lattice parameters of the bulk black phosphorus, as compared to optB88-vdW and PBE.

Our finding show that all considered molecules can bind strongly to the phosphorene surface with different energy-preferable adsorption sites, when van der Waals interactions are taken into account. Except for NO and NO_2, no noticeable charge transfer was found. For NO_2, both optB88-vdW and SCAN+rVV10 predict substantial charge transfer from the substrate to the molecule (~ 0.34e), while for NO, SCAN+rVV10 predicts a negligible charge transfer and optB88-vdW predicting a small charge transfer (.16e).

The calculated effects of molecular coverage showed substantial differences between the two functionals. Our calculated comparison between the optB88-vdW functional and the newly introduced SCAN+rVV10 functional shows that, as the coverage increases, substantial differences in adsorption energies and configurations between the two functionals start to appear.

GENERAL CONCLUSION

In this thesis, we have employed first-principles calculations in order to explore the physical properties of phosphorene and to exploit them in various technological applications. we attempted to demonstrate that phosphorene's unique properties such as its anisotropic and puckered structure in addition to its tunable direct bandgap, that are not found in graphene and therefore limit its integration, could make of phosphorene a promising candidate for the next-generation nanoelectronic devices where such properties are needed.

Indeed, our first-principles calculations on the strain and size effects interplay, where both structural and electronic properties of a phosphorene monolayer, bilayer and trilayer under a uniaxial strain, are explored, show that the applied strain either on the armchair or zigzag direction tends to change the nature of the bandgap from a direct to an indirect electronic gap as a function of the strain value. However, we find that within a strain ranging from -14% to +6%, the ML, BL and TL structures behave like most semiconductors under strain where compressive strain blueshifts the bandgap and tensile strain redshifts it. Finally, a very interesting strain-size combined effect is observed on the VBM and CBM bands where the Fermi level shifts from one side to another of the energy gap. While the ML, BL and TL structures are of *p-type* at 0% strain, they switch to n-type semiconductors under strain ranging from +2% up to +14%. We believe that this p-type to n-type transition ability may have a major technological impact in fields where mono- and hetero-junctions are needed.

In terms of adsorption and surface-diffusion behaviors of alkali atoms (Li, Na and K) and alkaline earth-metal atoms (Be, Mg and Ca) on a phosphorene surface in order to evaluate its performance as an anode material for rechargeable batteries, our results show that all the elements can be stably adsorbed on phosphorene and tend to prefer to be adsorbed on the H-site. The binding energy of alkali atoms show that the atomic size highly influences the interaction between the adatom and the substrate while the interaction of alkaline-earth metals and phosphorene is difficult

to be predicted. In comparison with graphene, our results show that phosphorene enhances the biding energies of the adsorbed atoms. Moreover, a semiconductor-to-metal transition is observed upon the complete adsorption of more than four atoms, which is vital for electrode uses. Besides, the diffusion analysis shows that the migration of the adatoms on phosphorene is highly influenced by its structural anisotropy giving a privilege to the diffusion along the zigzag direction over the armchair direction. Owing to its large atomic size, we found that the diffusion barrier of K along the zigzag direction is extremely low (0.02 eV) while an atomic size of the order of Be atom finds it almost prohibited to diffuse along the armchair direction (0.77 eV). Our findings show that phosphorene clearly exhibits a higher performance than other 2D materials such as graphene in terms of adsorption and diffusion, but a less capacity of storage than the latter. Nevertheless, we believe that a phosphorene-graphene hybrid system may constitute promising high-capacity ion-anode.

On the other hand, our results show a better agreement with previous experimental studies when using the SCAN+rVV10 method, as compared with those obtained from optB88-vdW and PBE in terms of the calculated lattice parameters of the bulk black phosphorus. In addition, adsorption behavior of NH_3, NO, NO_2, CO and CO_2 molecules on a phosphorene surface are explored and show that all considered molecules can bind strongly to the phosphorene surface with different energy-preferred adsorption sites, when van der Waals interactions are taken into account. Except for NO and NO_2, no noticeable charge transfer was found. For NO_2, both optB88-vdW and SCAN+rVV10 predict substantial charge transfer from the substrate to the molecule (~ 0.34e), while for NO, SCAN+rVV10 predicts a negligible charge transfer and optB88-vdW predicting a small charge transfer (.16e). The calculated effects of molecular coverage showed substantial differences between the two functionals. Our calculated comparison between the optB88-vdW functional and the newly introduced SCAN+rVV10 functional shows that, as the coverage increases, substantial differences in adsorption energies and configurations between the two functionals start to appear.

Finally, we believe that the integration of phosphorene in future technologies faces a major hurdle toward the establishment of Phosphorene-based devices due to many factors which limit how we can benefit from this promising material such as the fast oxidation and subsequent

degradation of phosphorene under ambient conditions. Nevertheless, and although the accomplishment of this work was not an easy task to make due to the lack of high-performance computational resources in our country, we hope that our findings presented in this Thesis could provide an instructive insight to the experimental researchers working on the making of high performing phosphorene-based devices in the future.

References

[1] K. S. Novoselov, A. K. Geim, S. V. Morozov, D. Jiang, Y. Zhang, S. V. Dubonos, I. V. Grigorieva, A. A. Firsov. Electric Field Effect in Atomically Thin Carbon Films. Science 2004, 306, 666-669.

[2] A. K. Geim and K. S. Novoselov. Nat. Mater. vol. 6 183 p. 183, 2007.

[3] K.I. Bolotina, K.J. Sikesb, Z. Jianga, M. Klimac, G. Fudenberga, J. Honec, P. Kima, H.L. Stormera. Ultrahigh electron mobility in suspended graphene. Solid State Communications, Volume 146, Issues 9-10, June 2008, Pages 351-355.

[4] M. S. Fuhrer, J. Hone. Measurement of Mobility in Dual-gated MoS 2 Transistors. Nat. Nanotechnol. 2013, 8, 146-147.

[5] Tayari, V. et al. Two-dimensional magnetotransport in a black phosphorus naked quantum well. Nat. Commun. 6:7702 doi: 10.1038/ncomms8702 (2015).

[6] Liu, H.; Neal, A. T.; Zhu, Z.; Luo, Z.; Xu, X.; Tomanek, D.; Ye, P. D. Phosphorene: An Unexplored 2D Semiconductor with a High Hole Mobility. ACS Nano 2014, 8, 4033-4041.

[7] S. Appalakondaiah, G. Vaitheeswaran, S. Lebegue, N. E. Christensen, A. Svane. Effect of Van der Waals Interactions on the Structural and Elastic Properties of Black Phosphorus. Phys. Rev. B: Condens. Matter Mater. Phys. 2012, 86, 035105.

[8] Appalakondaiah, S.; Vaitheeswaran, G.; Lebegue, S.; Christensen, N. E.; Svane, A. Effect of Van der Waals Interactions on the Structural and Elastic Properties of Black Phosphorus. Phys. Rev. B: Condens. Matter Mater. Phys. 2012, 86, 035105.

[9] Castellanos-Gomez, A.; Vicarelli, L.; Prada, E.; Island, J. O.; Narasimha-Acharya, K.; Blanter, S. I.; Groenendijk, D. J.; Buscema, M.; Steele, G. A.; Alvarez, J. Isolation and Characterization of Few-layer Black Phosphorus. 2014, arXiv :1403.0499.

[10] Qiao, J.; Kong, X.; Hu, Z.-X.; Yang, F.; Ji, W. Few-layer Black Phosphorus: Emerging Direct Band Gap Semiconductor with High Carrier Mobility. 2014, arXiv :1401.5045.

[11] Dienwiebel M, Verhoeven GS, Pradeep N, Frenken JW, Heimberg JA, Zandbergen HW. Superlubricity of graphite. Physical review letters. 2004 Mar 24;92(12):126101.

[12] Nicolosi V, Chhowalla M, Kanatzidis MG, Strano MS, Coleman JN. Liquid exfoliation of layered materials. Science. 2013 Jun 21;340(6139):1226419.

[13] Karttunen AJ, Linnolahti M, Pakkanen TA. Structural principles of polyhedral allotropes of phosphorus. ChemPhysChem. 2008 Dec 1;9(17):2550-8.
[14] Bridgman PW. TWO NEW MODIFICATIONS OF PHOSPHORUS. Journal of the American Chemical Society. 1914 Jul;36(7):1344-63.
[15] Endo S, Akahama Y, Terada SI, Narita SI. Growth of large single crystals of black phosphorus under high pressure. Japanese Journal of Applied Physics. 1982 Aug;21(8A):L482.
[16] Warschauer D. Electrical and optical properties of crystalline black phosphorus. Journal of Applied Physics. 1963 Jul;34(7):1853-60.
[17] Brown A, Rundqvist S. Refinement of the crystal structure of black phosphorus. Acta Crystallographica. 1965 Oct 10;19(4):684-5.
[18] Liu H, Du Y, Deng Y, Peide DY. Semiconducting black phosphorus: synthesis, transport properties and electronic applications. Chemical Society Reviews. 2015 Apr 28;44(9):2732-43.
[19] Sansone G, Maschio L, Usvyat D, Schütz M, Karttunen A. Toward an accurate estimate of the exfoliation energy of black phosphorus: a periodic quantum chemical approach. The journal of physical chemistry letters. 2015 Dec 22;7(1):131-6.
[20] Bridgman 2. Effects of high shearing stress combined with high hydrostatic pressure. Physical Review. 1935 Nov 15;48(10):825.
[21] Park, C.M. and Sohn, H.J., 2007. Black phosphorus and its composite for lithium rechargeable batteries. Advanced materials, 19(18), pp.2465-2468.
[22] Nilges, T., Kersting, M. and Pfeifer, T., 2008. A fast low-pressure transport route to large black phosphorus single crystals. Journal of solid state chemistry, 181(8), pp.1707-1711.
[23] Köpf, M., Eckstein, N., Pfister, D., Grotz, C., Krüger, I., Greiwe, M., Hansen, T., Kohlmann, H. and Nilges, T., 2014. Access and in situ growth of phosphorene-precursor black phosphorus. Journal of crystal growth, 405, pp.6-10.
[24] Moran, S.T., Nayak, A., Barron, M., Khakoo, U. and Akinwande, D., 2015. Investigating Ultrasonicated Allotropes of Phosphorus. 2015 NCUR.
[25] Novoselov, K.S., Geim, A.K., Morozov, S.V., Jiang, D., Zhang, Y., Dubonos, S.V., Grigorieva, I.V. and Firsov, A.A., 2004. Electric field effect in atomically thin carbon films. science, 306(5696), pp.666-669.

[26] Novoselov, K.S., Geim, A.K., Morozov, S., Jiang, D., Katsnelson, M.I., Grigorieva, I., Dubonos, S. and Firsov, A.A., 2005. Two-dimensional gas of massless Dirac fermions in graphene. nature, 438(7065), p.197.

[27] Liu, H., Neal, A.T., Zhu, Z., Luo, Z., Xu, X., Tománek, D. and Ye, P.D., 2014. Phosphorene: an unexplored 2D semiconductor with a high hole mobility. ACS nano, 8(4), pp.4033-4041.

[28] Li, L., Yu, Y., Ye, G.J., Ge, Q., Ou, X., Wu, H., Feng, D., Chen, X.H. and Zhang, Y., 2014. Black phosphorus field-effect transistors. Nature nanotechnology, 9(5), p.372.

[29] Cain, D.F. and Davies, R.E., 1962. Breakdown of adenosine triphosphate during a single contraction of working muscle. Biochemical and biophysical research communications, 8(5), pp.361-366.

[30] Srivastava, A., Khan, M.S., Gupta, S.K. and Pandey, R., 2015. Unique electron transport in ultrathin black phosphorene: Ab-initio study. Applied Surface Science, 356, pp.881-887.

[31] Island, J.O., Steele, G.A., van der Zant, H.S. and Castellanos-Gomez, A., 2015. Environmental instability of few-layer black phosphorus. 2D Materials, 2(1), p.011002.

[32] Wood, J.D., Wells, S.A., Jariwala, D., Chen, K.S., Cho, E., Sangwan, V.K., Liu, X., Lauhon, L.J., Marks, T.J. and Hersam, M.C., 2014. Effective passivation of exfoliated black phosphorus transistors against ambient degradation. Nano letters, 14(12), pp.6964-6970.

[33] Favron, A., Gaufrès, E., Fossard, F., Phaneuf-L'Heureux, A.L., Tang, N.Y., Lévesque, P.L., Loiseau, A., Leonelli, R., Francoeur, S. and Martel, R., 2015. Photooxidation and quantum confinement effects in exfoliated black phosphorus. Nature materials, 14(8), p.826.

[34] Guo, Z., Zhang, H., Lu, S., Wang, Z., Tang, S., Shao, J., Sun, Z., Xie, H., Wang, H., Yu, X.F. and Chu, P.K., 2015. From black phosphorus to phosphorene: basic solvent exfoliation, evolution of Raman scattering, and applications to ultrafast photonics. Advanced Functional Materials, 25(45), pp.6996-7002.

[35] Liu, H., Neal, A.T., Si, M., Du, Y. and Peide, D.Y., 2014. The effect of dielectric capping on few-layer phosphorene transistors: Tuning the Schottky barrier heights. IEEE Electron Device Letters, 35(7), pp.795-797.

[36] L. D. Landau and E. M. Lifshitz. Statistical Physics, volume 5. Butterworth-Heinemann, 3 edition, 1996.

[37] Novoselov, K.S., Jiang, D., Schedin, F., Booth, T.J., Khotkevich, V.V., Morozov, S.V. and Geim, A.K., 2005. Two-dimensional atomic crystals. Proceedings of the National Academy of Sciences, 102(30), pp.10451-10453.

[38] Novoselov, K.S. and Neto, A.C., 2012. Two-dimensional crystals-based heterostructures: materials with tailored properties. Physica Scripta, 2012(T146), p.014006.

[39] Woomer, A.H., Farnsworth, T.W., Hu, J., Wells, R.A., Donley, C.L. and Warren, S.C., 2015. Phosphorene: synthesis, scale-up, and quantitative optical spectroscopy. ACS nano, 9(9), pp.8869-8884.

[40] Park, S. and Ruoff, R.S., 2009. Chemical methods for the production of graphenes. Nature nanotechnology, 4(4), p.217.

[41] Ayari, A., Cobas, E., Ogundadegbe, O. and Fuhrer, M.S., 2007. Realization and electrical characterization of ultrathin crystals of layered transition-metal dichalcogenides. Journal of applied physics, 101(1), p.014507.

[42] De Padova, P., Quaresima, C., Ottaviani, C., Sheverdyaeva, P.M., Moras, P., Carbone, C., Topwal, D., Olivieri, B., Kara, A., Oughaddou, H. and Aufray, B., 2010. Evidence of graphene-like electronic signature in silicene nanoribbons. Applied Physics Letters, 96(26), p.261905.

[43] Luo, Z., Maassen, J., Deng, Y., Du, Y., Garrelts, R.P., Lundstrom, M.S., Peide, D.Y. and Xu, X., 2015. Anisotropic in-plane thermal conductivity observed in few-layer black phosphorus. Nature communications, 6, p.8572.

[44] Popović, Z.S., Kurdestany, J.M. and Satpathy, S., 2015. Electronic structure and anisotropic Rashba spin-orbit coupling in monolayer black phosphorus. Physical Review B, 92(3), p.035135.

[45] Hashmi, A., Farooq, U. and Hong, J., 2016. Graphene/phosphorene bilayer: High electron speed, optical property and semiconductor-metal transition with electric field. Current Applied Physics, 16(3), pp.318-323.

[46] Qiao, J., Kong, X., Hu, Z.X., Yang, F. and Ji, W., 2014. High-mobility transport anisotropy and linear dichroism in few-layer black phosphorus. Nature communications, 5, p.4475.

[47] Sun, J., Zheng, G., Lee, H.W., Liu, N., Wang, H., Yao, H., Yang, W. and Cui, Y., 2014. Formation of stable phosphorus–carbon bond for enhanced performance in black phosphorus nanoparticle–graphite composite battery anodes. Nano letters, 14(8), pp.4573-4580.

[48] Li, W., Yang, Y., Zhang, G. and Zhang, Y.W., 2015. Ultrafast and directional diffusion of lithium in phosphorene for high-performance lithium-ion battery. Nano letters, 15(3), pp.1691-1697.

[49] Yao, Q., Huang, C., Yuan, Y., Liu, Y., Liu, S., Deng, K. and Kan, E., 2015. Theoretical prediction of phosphorene and nanoribbons as fast-charging Li ion battery anode materials. The Journal of Physical Chemistry C, 119(12), pp.6923-6928.

[50] Tran, V., Soklaski, R., Liang, Y. and Yang, L., 2014. Layer-controlled band gap and anisotropic excitons in few-layer black phosphorus. Physical Review B, 89(23), p.235319.

[51] Carvalho, A., Wang, M., Zhu, X., Rodin, A.S., Su, H. and Neto, A.H.C., 2016. Phosphorene: from theory to applications. Nature Reviews Materials, 1(11), p.16061.

[52] Du, X., Skachko, I., Barker, A. and Andrei, E.Y., 2008. Approaching ballistic transport in suspended graphene. Nature nanotechnology, 3(8), p.491.

[53] Ellis, J.K., Lucero, M.J. and Scuseria, G.E., 2011. The indirect to direct band gap transition in multilayered MoS2 as predicted by screened hybrid density functional theory. Applied Physics Letters, 99(26), p.261908.

[54] Jin, Z., Li, X., Mullen, J.T. and Kim, K.W., 2014. Intrinsic transport properties of electrons and holes in monolayer transition-metal dichalcogenides. Physical Review B, 90(4), p.045422.

[55] Rodin, A.S., Carvalho, A. and Neto, A.C., 2014. Strain-induced gap modification in black phosphorus. Physical review letters, 112(17), p.176801.

[56] Low, T., Rodin, A.S., Carvalho, A., Jiang, Y., Wang, H., Xia, F. and Neto, A.C., 2014. Tunable optical properties of multilayer black phosphorus thin films. Physical Review B, 90(7), p.075434.

[57] Deng, Y., Luo, Z., Conrad, N.J., Liu, H., Gong, Y., Najmaei, S., Ajayan, P.M., Lou, J., Xu, X. and Ye, P.D., 2014. Black phosphorus–monolayer MoS2 van der Waals heterojunction p–n diode. ACS nano, 8(8), pp.8292-8299.

[58] Kou, L., Chen, C. and Smith, S.C., 2015. Phosphorene: fabrication, properties, and applications. The journal of physical chemistry letters, 6(14), pp.2794-2805.

[59] Zhao, S., Kang, W. and Xue, J., 2014. The potential application of phosphorene as an anode material in Li-ion batteries. Journal of Materials Chemistry A, 2(44), pp.19046-19052.

[60] Kou, L., Frauenheim, T. and Chen, C., 2014. Phosphorene as a superior gas sensor: selective adsorption and distinct I–V response. The journal of physical chemistry letters, 5(15), pp.2675-2681.

[61] Ray, S.J., 2016. First-principles study of MoS2, phosphorene and graphene based single electron transistor for gas sensing applications. Sensors and Actuators B: Chemical, 222, pp.492-498.

[62] Liu, X., Ang, K.W., Yu, W., He, J., Feng, X., Liu, Q., Jiang, H., Tang, D., Wen, J., Lu, Y. and Liu, W., 2016. Black phosphorus based field effect transistors with simultaneously achieved near ideal subthreshold swing and high hole mobility at room temperature. Scientific reports, 6, p.24920.

[63] Palacios, T., Hsu, A. and Wang, H., 2010. Applications of graphene devices in RF communications. IEEE Communications Magazine, 48(6), pp.122-128

[64] Wang, H., Wang, X., Xia, F., Wang, L., Jiang, H., Xia, Q., Chin, M.L., Dubey, M. and Han, S.J., 2014. Black phosphorus radio-frequency transistors. Nano letters, 14(11), pp.6424-6429.

[65] Hohenberg, P. and Kohn, W., 1964. Inhomogeneous electron gas. Physical review, 136(3B), p.B864.

[66] Kohn, W. and Sham, L.J., 1965. Self-consistent equations including exchange and correlation effects. Physical review, 140(4A), p.A1133.

[67] Ceperley, D.M. and Alder, B.J., 1980. Ground state of the electron gas by a stochastic method. Physical Review Letters, 45(7), p.566.

[68] Tao, J., Perdew, J.P., Staroverov, V.N. and Scuseria, G.E., 2003. Climbing the density functional ladder: Nonempirical meta–generalized gradient approximation designed for molecules and solids. Physical Review Letters, 91(14), p.146401.

[69] Perdew, J.P., Ruzsinszky, A., Csonka, G.I., Constantin, L.A. and Sun, J., 2009. Workhorse semilocal density functional for condensed matter physics and quantum chemistry. Physical Review Letters, 103(2), p.026403.

[70] Sun, J., Xiao, B. and Ruzsinszky, A., 2012. Communication: Effect of the orbital-overlap dependence in the meta generalized gradient approximation.

[71] del Campo, J.M., Gázquez, J.L., Trickey, S.B. and Vela, A., 2012. A new meta-GGA exchange functional based on an improved constraint-based GGA. Chemical Physics Letters, 543, pp.179-183.

[72] Sun, J., Ruzsinszky, A. and Perdew, J.P., 2015. Strongly constrained and appropriately normed semilocal density functional. Physical review letters, 115(3), p.036402.
[73] Blöchl, P.E., 1994. Projector augmented-wave method. Physical review B, 50(24), p.17953.
[74] Giannozzi, P., Baroni, S., Bonini, N., Calandra, M., Car, R., Cavazzoni, C., Ceresoli, D., Chiarotti, G.L., Cococcioni, M., Dabo, I. and Dal Corso, A., 2009. QUANTUM ESPRESSO: a modular and open-source software project for quantum simulations of materials. Journal of physics: Condensed matter, 21(39), p.395502.
[75] Wu X, Xu Z, Zeng XC. Single-walled MoTe2 nanotubes. Nano letters. 2007 Oct 10;7(10):2987-92.
[76] Geim, A.; Grigorieva, I. Van der Waals Heterostructures. Nature (London, U.K.) 2013, 499, 419-425.
[77] Liu, Q., Li, L., Li, Y., Gao, Z., Chen, Z. and Lu, J., 2012. Tuning electronic structure of bilayer MoS2 by vertical electric field: a first-principles investigation. The Journal of Physical Chemistry C, 116(40), pp.21556-21562.
[78] Guo, H., Lu, N., Dai, J., Wu, X. and Zeng, X.C., 2014. Phosphorene nanoribbons, phosphorus nanotubes, and van der Waals multilayers. The Journal of Physical Chemistry C, 118(25), pp.14051-14059.
[79] Yu, W.J., Li, Z., Zhou, H., Chen, Y., Wang, Y., Huang, Y. and Duan, X., 2013. Vertically stacked multi-heterostructures of layered materials for logic transistors and complementary inverters. Nature materials, 12(3), p.246.
[80] Lee, D.H. and Gupta, J.A., 2010. Tunable field control over the binding energy of single dopants by a charged vacancy in GaAs. Science, 330(6012), pp.1807-1810.
[81] Cai, J., Ruffieux, P., Jaafar, R., Bieri, M., Braun, T., Blankenburg, S., Muoth, M., Seitsonen, A.P., Saleh, M., Feng, X. and Müllen, K., 2010. Atomically precise bottom-up fabrication of graphene nanoribbons. Nature, 466(7305), p.470.
[82] Wang, X., Ouyang, Y., Li, X., Wang, H., Guo, J. and Dai, H., 2008. Room-temperature all-semiconducting sub-10-nm graphene nanoribbon field-effect transistors. Physical review letters, 100(20), p.206803.
[83] Lee, J.K., Yamazaki, S., Yun, H., Park, J., Kennedy, G.P., Kim, G.T., Pietzsch, O., Wiesendanger, R., Lee, S., Hong, S. and Dettlaff-Weglikowska, U., 2013. Modification of

electrical properties of graphene by substrate-induced nanomodulation. Nano letters, 13(8), pp.3494-3500.

[84] Liu, Q., Zhang, X., Abdalla, L.B., Fazzio, A. and Zunger, A., 2015. Switching a normal insulator into a topological insulator via electric field with application to phosphorene. Nano letters, 15(2), pp.1222-1228.

[85] Jacobsen, R.S., Andersen, K.N., Borel, P.I., Fage-Pedersen, J., Frandsen, L.H., Hansen, O., Kristensen, M., Lavrinenko, A.V., Moulin, G., Ou, H. and Peucheret, C., 2006. Strained silicon as a new electro-optic material. Nature, 441(7090), p.199.

[86] Haeni, J.H., Irvin, P., Chang, W., Uecker, R., Reiche, P., Li, Y.L., Choudhury, S., Tian, W., Hawley, M.E., Craigo, B. and Tagantsev, A.K., 2004. Room-temperature ferroelectricity in strained SrTiO 3. Nature, 430(7001), p.758.

[87] Hochbaum, A.I. and Yang, P., 2009. Semiconductor nanowires for energy conversion. Chemical reviews, 110(1), pp.527-546.

[88] Peng, X. and Logan, P., 2010. Electronic properties of strained Si/Ge core-shell nanowires. Applied Physics Letters, 96(14), p.143119.

[89] Thean, A. and Leburton, J.P., 2001. Strain effect in large silicon nanocrystal quantum dots. Applied Physics Letters, 79(7), pp.1030-1032.

[90] Lee, C., Wei, X., Kysar, J.W. and Hone, J., 2008. Measurement of the elastic properties and intrinsic strength of monolayer graphene. science, 321(5887), pp.385-388.

[91] Bertolazzi, S., Brivio, J. and Kis, A., 2011. Stretching and breaking of ultrathin MoS2. ACS nano, 5(12), pp.9703-9709.

[92] Peng, X., Wei, Q. and Copple, A., 2014. Strain-engineered direct-indirect band gap transition and its mechanism in two-dimensional phosphorene. Physical Review B, 90(8), p.085402.

[93] Wei, Q. and Peng, X., 2014. Superior mechanical flexibility of phosphorene and few-layer black phosphorus. Applied Physics Letters, 104(25), p.251915.

[94] Tran, V., Soklaski, R., Liang, Y. and Yang, L., 2014. Layer-controlled band gap and anisotropic excitons in few-layer black phosphorus. Physical Review B, 89(23), p.235319.

[95] Gilman, J.J., 2003. Electronic basis of the strength of materials. Cambridge University Press.

[96] Zhu, T. and Li, J., 2010. J. Ultra-strength materials Prog. Mater. Sci, 55, pp.710-757.

[97] Feynman, R.P., 1960. There's plenty of room at the bottom. California Institute of Technology, Engineering and Science magazine.

[98] Li, J., Shan, Z. and Ma, E., 2014. Elastic strain engineering for unprecedented materials properties. MRS Bulletin, 39(2), pp.108-114.

[99] Bedell, S.W., Khakifirooz, A. and Sadana, D.K., 2014. Strain scaling for CMOS. Mrs Bulletin, 39(2), pp.131-137.

[100] Zhang, H., Tersoff, J., Xu, S., Chen, H., Zhang, Q., Zhang, K., Yang, Y., Lee, C.S., Tu, K.N., Li, J. and Lu, Y., 2016. Approaching the ideal elastic strain limit in silicon nanowires. Science advances, 2(8), p.e1501382.

[101] Banerjee, A., Bernoulli, D., Zhang, H., Yuen, M.F., Liu, J., Dong, J., Ding, F., Lu, J., Dao, M., Zhang, W. and Lu, Y., 2018. Ultralarge elastic deformation of nanoscale diamond. Science, 360(6386), pp.300-302.

[102] Shi, Z., Tsymbalov, E., Dao, M., Suresh, S., Shapeev, A. and Li, J., 2019. Deep elastic strain engineering of bandgap through machine learning. Proceedings of the National Academy of Sciences, 116(10), pp.4117-4122.

[103] Tsao JY, et al. (2018) Ultrawide-bandgap semiconductors: Research opportunities and challenges. Adv Electron Mater 4:1600501

[104] Li, L., Yu, Y., Ye, G.J., Ge, Q., Ou, X., Wu, H., Feng, D., Chen, X.H. and Zhang, Y., 2014. Black phosphorus field-effect transistors. Nature nanotechnology, 9(5), p.372.

[105] Xia, F., Wang, H. and Jia, Y., 2014. Rediscovering black phosphorus as an anisotropic layered material for optoelectronics and electronics. Nature communications, 5, p.4458.

[106] Yang, J., Xu, R., Pei, J., Myint, Y.W., Wang, F., Wang, Z., Zhang, S., Yu, Z. and Lu, Y., 2014. Unambiguous identification of monolayer phosphorene by phase-shifting interferometry. arXiv preprint arXiv:1412.6701.

[107] Giannozzi, P., Baroni, S., Bonini, N., Calandra, M., Car, R., Cavazzoni, C., Ceresoli, D., Chiarotti, G.L., Cococcioni, M., Dabo, I. and Dal Corso, A., 2009. QUANTUM ESPRESSO: a modular and open-source software project for quantum simulations of materials. Journal of physics: Condensed matter, 21(39), p.395502.

[108] Perdew, J.P., Burke, K. and Ernzerhof, M., 1996. Generalized gradient approximation made simple. Physical review letters, 77(18), p.3865.

[109] Grimme, S., 2006. Semiempirical GGA-type density functional constructed with a long-range dispersion correction. Journal of computational chemistry, 27(15), pp.1787-1799.

[110] Heyd, J., Scuseria, G.E. and Ernzerhof, M., 2003. Hybrid functionals based on a screened Coulomb potential. The Journal of chemical physics, 118(18), pp.8207-8215.
[111] Brown, A. and Rundqvist, S., 1965. Refinement of the crystal structure of black phosphorus. Acta Crystallographica, 19(4), pp.684-685.
[112] Carvalho, A., Wang, M., Zhu, X., Rodin, A.S., Su, H. and Neto, A.H.C., 2016. Phosphorene: from theory to applications. Nature Reviews Materials, 1(11), p.16061.
[113] Çakır, D., Sevik, C. and Peeters, F.M., 2015. Significant effect of stacking on the electronic and optical properties of few-layer black phosphorus. Physical Review B, 92(16), p.165406.
[114] Wang, C., Xia, Q., Nie, Y. and Guo, G., 2015. Strain-induced gap transition and anisotropic Dirac-like cones in monolayer and bilayer phosphorene. Journal of Applied Physics, 117(12), p.124302.
[115] Perdew, J.P., 1985. Density functional theory and the band gap problem. International Journal of Quantum Chemistry, 28(S19), pp.497-523.
[116] Kou, L., Ma, Y., Smith, S.C. and Chen, C., 2015. Anisotropic ripple deformation in phosphorene. The journal of physical chemistry letters, 6(9), pp.1509-1513.
[117] Fei, R. and Yang, L., 2014. Strain-engineering the anisotropic electrical conductance of few-layer black phosphorus. Nano letters, 14(5), pp.2884-2889.
[118] Kittel C. Chapter 7. Introduction to solid state physics. Wiley; 2005
[119] Keyes, R.W., 1953. The electrical properties of black phosphorus. Physical Review, 92(3), p.580.
[120] Peng, X., Copple, A. and Wei, Q., 2014. Edge effects on the electronic properties of phosphorene nanoribbons. Journal of Applied Physics, 116(14), p.144301.
[121] Novoselov KS, Geim AK, Morozov SV, Jiang D, Zhang Y, Dubonos SV, Grigorieva IV, Firsov AA (2004) Electric field effect in atomically thin carbon films. Science 306(5696):666-9
[122] Geim AK, Novoselov KS (2007) The rise of graphene. Nat. Mater. 6(3):183-91
[123] Neto AC, Guinea F, Peres NM, Novoselov KS, Geim AK (2009) The electronic properties of graphene. Rev. Mod. Phys. 81(1):109
[124] Lee C, Wei X, Kysar JW, Hone J (2008) Measurement of the elastic properties and intrinsic strength of monolayer graphene. Science 321(5887):385-8
[125] Balandin AA, Ghosh S, Bao W, Calizo I, Teweldebrhan D, Miao F, Lau CN (2008) Superior thermal conductivity of single-layer graphene. Nano Lett. 8(3):902-7

[126] Liao L, Lin YC, Bao M, Cheng R, Bai J, Liu Y, Qu Y, Wang KL, Huang Y, Duan X (2010) High-speed graphene transistors with a self-aligned nanowire gate. Nature 467(7313):305-8
[127] Xia F, Farmer DB, Lin YM, Avouris P (2010) Graphene field-effect transistors with high on/off current ratio and large transport band gap at room temperature. Nano Lett. 10(2):715-8
[128] Miao X, Tongay S, Petterson MK, Berke K, Rinzler AG, Appleton BR, Hebard AF (2012) High efficiency graphene solar cells by chemical doping. Nano Lett. 12(6):2745-50
[129] Liu H, Gao P, Fang J, Yang G (2011) Li 3 V 2 (PO 4) 3/graphene nanocomposites as cathode material for lithium ion batteries. Chem. Commun. 47(32):9110-2
[130] Yan JF, Zhang SY, Wang G, Wang H, Zhang ZY, Ruan XF, Zheng HY (2015) Preparation Assisted via Thermal Stress and Electrochemical Performance of Graphene Nano-Sheets as Anode Materials for Lithium-Ion Batteries. Integr. Ferroelectr. 160(1):27-37
[131] Yoo E, Kim J, Hosono E, Zhou HS, Kudo T, Honma I (2008) Large reversible Li storage of graphene nanosheet families for use in rechargeable lithium ion batteries. Nano Lett. 8(8):2277-82
[132] Chang K, Chen W (2011) L-cysteine-assisted synthesis of layered MoS2/graphene composites with excellent electrochemical performances for lithium ion batteries. ACS Nano 5(6):4720-8
[133] Yang S, Gong Y, Liu Z, Zhan L, Hashim DP, Ma L, Vajtai R, Ajayan PM (2013) Bottom-up approach toward single-crystalline VO2-graphene ribbons as cathodes for ultrafast lithium storage. Nano Lett. 13(4):1596-601
[134] Feng C, Ma J, Li H, Zeng R, Guo Z, Liu H (2009) Synthesis of molybdenum disulfide (MoS 2) for lithium ion battery applications. Mater. Res. Bull. 44(9):1811-5
[135] Du G, Guo Z, Wang S, Zeng R, Chen Z, Liu H (2010) Superior stability and high capacity of restacked molybdenum disulfide as anode material for lithium ion batteries. Chem. Commun. 46(7):1106-8
[136] Hwang H, Kim H, Cho J (2011) MoS2 nanoplates consisting of disordered graphene-like layers for high rate lithium battery anode materials. Nano Lett. 11(11):4826-30
[137] Chang K, Chen W (2011) Single-layer MoS 2/graphene dispersed in amorphous carbon: towards high electrochemical performances in rechargeable lithium ion batteries. J. Mater. Chem. 21(43):17175-84

[138] Li Y, Wu D, Zhou Z, Cabrera CR, Chen Z (2012) Enhanced Li adsorption and diffusion on MoS2 zigzag nanoribbons by edge effects: a computational study. J. Phys. Chem. Lett. 3(16):2221-7

[139] Raccichini R, Varzi A, Passerini S, Scrosati B (2015) The role of graphene for electrochemical energy storage. Nat. Mater. 14(3):271-9

[140] Park CM, Sohn HJ (2007) Black phosphorus and its composite for lithium rechargeable batteries. Adv. Mater. 19(18):2465-8

[141] Li L, Yu Y, Ye GJ, Ge Q, Ou X, Wu H, Feng D, Chen XH, Zhang Y (2014) Black phosphorus field-effect transistors. Nat. Nanotechnol. 9(5):372-7

[142] Komaba S, Murata W, Ishikawa T, Yabuuchi N, Ozeki T, Nakayama T, Ogata A, Gotoh K, Fujiwara K (2011) Electrochemical Na insertion and solid electrolyte interphase for hard-carbon electrodes and application to Na-Ion batteries. Adv. Funct. Mater. 21(20):3859-67

[143] Sun J, Lee HW, Pasta M, Yuan H, Zheng G, Sun Y, Li Y, Cui Y (2015) A phosphorene–graphene hybrid material as a high-capacity anode for sodium-ion batteries. Nat. Nanotechnol. 10(11):980-5

[144] Giannozzi P, Baroni S, Bonini N, Calandra M, Car R, Cavazzoni C, Ceresoli D, Chiarotti GL, Cococcioni M, Dabo I, Dal Corso A (2009) QUANTUM ESPRESSO: a modular and open-source software project for quantum simulations of materials. J. Phys.: Condens. Matter 21(39):395502

[145] Perdew JP, Burke K, Ernzerhof M (1996) Generalized gradient approximation made simple. Phys. Rev. Lett. 77(18):3865

[146] Grimme S (2004) Accurate description of van der Waals complexes by density functional theory including empirical corrections. J. Comput. Chem. 25(12):1463-73

[147] Li QF, Duan CG, Wan XG, Kuo JL (2015) Theoretical prediction of anode materials in Li-ion batteries on layered black and blue phosphorus. J. Phys. Chem. C 119(16):8662-70

[148] Zhu Z, Tománek D (2014) Semiconducting layered blue phosphorus: A computational study. Phys. Rev. Lett. 112(17):176802

[149] Kou L, Frauenheim T, Chen C (2014) Phosphorene as a superior gas sensor: Selective adsorption and distinct I–V response. J. Phys. Chem. Lett. 5(15):2675-81

[150] Tritsaris GA, Kaxiras E, Meng S, Wang E (2013) Adsorption and diffusion of lithium on layered silicon for Li-ion storage. Nano Lett. 13(5):2258-63

[151] Banerjee S, Pati SK (2016) Anodic performance of black phosphorus in magnesium-ion batteries: the significance of Mg–P bond-synergy. Chem. Commun. 52(54):8381-4
[152] Kulish VV, Malyi OI, Persson C, Wu P (2015) Adsorption of metal adatoms on single-layer phosphorene. Phys. Chem. Chem. Phys. 17(2):992-1000
[153] Li W, Yang Y, Zhang G, Zhang YW (2015) Ultrafast and directional diffusion of lithium in phosphorene for high-performance lithium-ion battery. Nano Lett. 15(3):1691-7
[154] Kulish VV, Malyi OI, Persson C, Wu P (2015) Phosphorene as an anode material for Na-ion batteries: a first-principles study. Phys. Chem. Chem. Phys. 17(21):13921-8
[155] Liu X, Wang CZ, Hupalo M, Lu WC, Tringides MC, Yao YX, Ho KM (2012) Metals on graphene: correlation between adatom adsorption behavior and growth morphology. Phys. Chem. Chem. Phys. 14(25):9157-66
[156] Denis PA, Iribarne F (2014) Theoretical investigation on the interaction between beryllium, magnesium and calcium with benzene, coronene, cirumcoronene and graphene. Chem. Phys. 430:1-6
[157] Henkelman G, Arnaldsson A, Jónsson H (2006) A fast and robust algorithm for Bader decomposition of charge density. Comput. Mater. Sci.. 30;36(3):354-60.
[158] Uthaisar C, Barone V (2010) Edge effects on the characteristics of Li diffusion in graphene. Nano Lett. 10(8):2838-42
[159] Xu B, Lu HS, Liu B, Liu G, Wu MS, Ouyang C (2016) Comparisons between adsorption and diffusion of alkali, alkaline earth metal atoms on silicene and those on silicane: Insight from first-principles calculations. Chin. Phys. B. 25(6):067103
[160] Radisavljevic B, Radenovic A, Brivio J, Giacometti IV, Kis A (2011) Single-layer MoS2 transistors. Nat. Nanotechnol. 6(3):147-50
[161] Tang Q, Zhou Z, Shen P (2012) Are MXenes promising anode materials for Li ion batteries? Computational studies on electronic properties and Li storage capability of Ti3C2 and Ti3C2X2 (X= F, OH) monolayer. J. Am. Chem. Soc. 134(40):16909-16
[162] Mortazavi M, Wang C, Deng J, Shenoy VB, Medhekar NV (2014) Ab initio characterization of layered MoS 2 as anode for sodium-ion batteries. J. Power Sources 268:279-86
[163] Mortazavi B, Dianat A, Cuniberti G, Rabczuk T (2016) Application of silicene, germanene and stanene for Na or Li ion storage: A theoretical investigation. Electrochim. Acta 20;213:865-70.

[164] Tran V, Soklaski R, Liang Y, Yang L (2014) Layer-controlled band gap and anisotropic excitons in few-layer black phosphorus. Phys. Rev. B 26;89(23):235319

[165] Datta D, Li J, Shenoy VB (2014) Defective graphene as a high-capacity anode material for Na-and Ca-ion batteries. ACS Appl. Mater. Interfaces 6(3):1788-95

[166] Er D, Li J, Naguib M, Gogotsi Y, Shenoy VB (2014) Ti3C2 MXene as a high capacity electrode material for metal (Li, Na, K, Ca) ion batteries. ACS Appl. Mater. Interfaces 6(14):11173-9

[167] Kawasaki, H., Ueda, T., Suda, Y. and Ohshima, T., 2004. Properties of metal doped tungsten oxide thin films for NOx gas sensors grown by PLD method combined with sputtering process. Sensors and Actuators B: Chemical, 100(1-2), pp.266-269.

[168] Guth, U. and Zosel, J., 2004. Electrochemical solid electrolyte gas sensors—Hydrocarbon and NO x analysis in exhaust gases. Ionics, 10(5-6), pp.366-377.

[169] Yoo, K.S., 2011. Gas sensors for monitoring air pollution. Monitoring, Control and Effects of Air Pollution, pp.51-52.

[170] Kim, H.K., Yun, Y.K. and Ahn, Y.J., 2007. Toxicity of atractylon and atractylenolide III identified in Atractylodes ovata rhizome to Dermatophagoides farinae and Dermatophagoides pteronyssinus. Journal of agricultural and food chemistry, 55(15), pp.6027-6031.

[171] H. J. An, C. H. Cheong, H. J. Kim, and Y. G. Lee, J. Archi. Ins. Kor., vol. 25, p. 51, 2005.

[172] J. W. Seo, J. Kor. Air-Condi. Refri., vol.31, p. 13, 2002.

[173] Japanese, R.D., 1989. Trend Analysis Report No. 6: Ceramic Sensors, KRI International. Inc., Tokyo.

[174] Lee, D.D., Rey, C. and Aiolova, M., Etex Corp, 2001. Cartilage growth from cell seeded ceramic compositions. U.S. Patent 6,277,151.

[175] Kim, T.S., Kim, Y.B., Yoo, K.S., Sung, G.S. and Jung, H.J., 2000. Sensing characteristics of dc reactive sputtered WO3 thin films as an NOx gas sensor. Sensors and Actuators B: Chemical, 62(2), pp.102-108.

[176] Zhang Y, Liu C, Hao F, Xiao H, Zhang S, Chen X. CO2 adsorption and separation from natural gason phosphorene surface: Combining DFT and GCMC calculations. Applied Surface Science. 2017 Mar 1;397:206-12.

[177] Li L, Yu Y, Ye GJ, Ge Q, Ou X, Wu H, Feng D, Chen XH, Zhang Y. Black phosphorus field-effect transistors. Nature nanotechnology. 2014 May;9(5):372.

[178] Sun J, Lee HW, Pasta M, Yuan H, Zheng G, Sun Y, Li Y, Cui Y. A phosphorene–graphene hybrid material as a high-capacity anode for sodium-ion batteries. Nature nanotechnology. 2015 Nov;10(11):980.
[179] Dai J, Zeng XC. Bilayer phosphorene: effect of stacking order on bandgap and its potential applications in thin-film solar cells. The journal of physical chemistry letters. 2014 Mar 26;5(7):1289-93.
[180] Kou L, Frauenheim T, Chen C. Phosphorene as a superior gas sensor: selective adsorption and distinct I–V response. The journal of physical chemistry letters. 2014 Jul 24;5(15):2675-81.
[181] Cai Y, Ke Q, Zhang G, Zhang YW. Energetics, charge transfer, and magnetism of small molecules physisorbed on phosphorene. The Journal of Physical Chemistry C. 2015 Jan 30;119(6):3102-10.
[182] Kuang A, Ran Y, Peng B, Kuang M, Wang G, Yuan H, Tian C, Chen H. Adsorption and decomposition of metal decorated phosphorene toward H2S, HCN and NH3 molecules. Applied Surface Science. 2019 Apr 15;473:242-50.
[183] Pang J, Yang Q, Ma X, Wang L, Tan C, Xiong D, Ye H, Chen X. DFT coupled with NEGF study of ultra-sensitive HCN and HNC gases detection and distinct I–V response based on phosphorene. Physical Chemistry Chemical Physics. 2017;19(45):30852-60.
[184] Mansouri E, Karamdel J, Berahman M, Ahmadi MT. Phosphorene as H2S and CH4 Gas Sensor. physica status solidi (a). 2019 Jan;216(2):1800086.
[185] Bhuvaneswari R, Chandiramouli R. First-principles investigation on detection of phosgene gas molecules using phosphorene nanosheet device. Chemical Physics Letters. 2019 Feb 16;717:99-106.
[186] Sun J, Remsing RC, Zhang Y, Sun Z, Ruzsinszky A, Peng H, Yang Z, Paul A, Waghmare U, Wu X, Klein ML. Accurate first-principles structures and energies of diversely bonded systems from an efficient density functional. Nature chemistry. 2016 Sep;8(9):831.
[187] Sun J, Ruzsinszky A, Perdew JP. Strongly constrained and appropriately normed semilocal density functional. Physical review letters. 2015 Jul 14;115(3):036402.
[188] Kresse G, Furthmüller J. Efficient iterative schemes for ab initio total-energy calculations using a plane-wave basis set. Physical review B. 1996 Oct 15;54(16):11169.

[189] Kresse G, Furthmüller J. Efficiency of ab-initio total energy calculations for metals and semiconductors using a plane-wave basis set. Computational materials science. 1996 Jul 1;6(1):15-50.

[190] Kresse G, Hafner J. Ab initio molecular dynamics for liquid metals. Physical Review B. 1993 Jan 1;47(1):558.

[191] Blöchl PE. Projector augmented-wave method. Physical review B. 1994 Dec 15;50(24):17953.

[192] Kresse G, Joubert D. From ultrasoft pseudopotentials to the projector augmented-wave method. Physical Review B. 1999 Jan 15;59(3):1758.

[193] Klimeš J, Bowler DR, Michaelides A. Chemical accuracy for the van der Waals density functional. Journal of Physics: Condensed Matter. 2009 Dec 10;22(2):022201.

[194] Sabatini R, Gorni T, De Gironcoli S. Nonlocal van der Waals density functional made simple and efficient. Physical Review B. 2013 Jan 31;87(4):041108.

[195] Vydrov OA, Van Voorhis T. Nonlocal van der Waals density functional: The simpler the better. The Journal of chemical physics. 2010 Dec 28;133(24):244103.

[196] Brown A, Rundqvist S. Refinement of the crystal structure of black phosphorus. Acta Crystallographica. 1965 Oct 10;19(4):684-5.

[197] Carvalho A, Wang M, Zhu X, Rodin AS, Su H, Neto AH. Phosphorene: from theory to applications. Nature Reviews Materials. 2016 Nov;1(11):16061.

[198] Sibari A, Kerrami Z, Kara A, Hamedoun M, Benyoussef A, Mounkachi O, Benaissa M. Adsorption and diffusion on a phosphorene monolayer: a DFT study. Journal of Solid State Electrochemistry. 2018 Jan 1;22(1):11-6.

[199] Henkelman G, Arnaldsson A, Jónsson H (2006) A fast and robust algorithm for Bader decomposition of charge density. Comput. Mater. Sci.. 30;36(3):354-60.

List of Publications

1. **A. Sibari**, Z. Kerrami, M. Benaissa, A. Kara. *Coverage dependent adsorption of small gas molecules on black phosphorene*, submitted.
2. **A. Sibari**, Z. Kerrami, A. Kara, O. Mounkachi, M. Hamedoun, A. Benyoussef, M. Benaissa. *Strain-engineered p-type to n-type transition in mono-, bi- and tri-layer phosphorene*, submitted.
3. Kerrami, Z., **Sibari, A.**, Mounkachi, O., Benyoussef, A. and Benaissa, M., **2019**. *SnO_2 improved thermoelectric properties under compressive strain.* Computational Condensed Matter, 18, p.e00356.
4. **Sibari, A.**, El Marjaoui, A., Lakhal, M., Kerrami, Z., Kara, A., Benaissa, M., Ennaoui, A., Hamedoun, M., Benyoussef, A. and Mounkachi, O., **2017**. *Phosphorene as a promising anode material for (Li/Na/Mg)-ion batteries: a first-principle study.* Solar Energy Materials and Solar Cells. 180, pp. 253-257.
5. Kerrami Z, **Sibari A**, Mounkachi O, Benyoussef A, Benaissa M. *Improved photo-electrochemical properties of strained SnO_2.* International Journal of Hydrogen Energy. **2018** Apr 21.
6. **Sibari, A.**, Kerrami, Z., Kara, A., Hamedoun, M., Benyoussef, A., Mounkachi, O. and Benaissa, M., **2018**. *Adsorption and diffusion on a phosphorene monolayer: a DFT study*. Journal of Solid-State Electrochemistry, 22(1), pp.11-16.
7. Kerrami Z, **Sibari A**, Benaissa M, Benyoussef A, Mounkachi O. *Strain Effect on The Photo-Catalytic Properties of SnO_2.* In 2017 International Renewable and Sustainable Energy Conference (IRSEC) **2017** Dec 4 (pp. 1-3). IEEE.
8. **Sibari A**, Kerrami Z, Kara A, Benyoussef A, Mounkachi O, Benaissa M. *Bandgap Engineering of Black Phosphorus-Based Nano structures.* In **2017** International Renewable and Sustainable Energy Conference (IRSEC) 2017 Dec 4 (pp. 1-4). IEEE.
9. Kerrami, Z., **Sibari, A.**, Lakhal, M., Benyoussef, A., Benaissa, M., Mounkachi, O. and Hamedoun, M., 2016, November. *Effect of biaxial strain on SnO_2 bandgap: First-principles calculations.* In Renewable and Sustainable Energy Conference (IRSEC), **2016** International (pp. 853-856). IEEE.

10. **Sibari, A.**, Kerrami, Z., Marjaoui, A., Lakhal, M., Benyoussef, A., Benaissa, M., Mounkachi, O. and Kara, A., **2016**, November. *Phosphorene as a promising anode material for lithium-ion batteries: A first-principle study.* In Renewable and Sustainable Energy Conference (IRSEC), 2016 International (pp. 931-934). IEEE.